



TECHNISCHE  
UNIVERSITÄT  
DARMSTADT

Physik

# Poly-N-isopropylacrylamide Based Microgels A Study on Magnetic Microgels and Their Structure

vom Fachbereich Physik  
der Technischen Universität Darmstadt

zur Erlangung des akademischen Grades

**Doktor der Naturwissenschaften**  
(Dr. rer. nat.)

genehmigte Dissertation von  
**M. Sc. Marcus Ulf Witt**  
geboren in Berlin

Promotionsausschuss:

- |                 |                               |
|-----------------|-------------------------------|
| 1. Gutachterin: | Prof. Dr. Regine von Klitzing |
| 2. Gutachter:   | Prof. Dr. Markus Biesalski    |
| 3. Prüfer:      | Prof. Dr. Emanuel Schneck     |
| 4. Prüfer:      | Prof. Dr. Jens Braun          |

Tag der Disputation: 21.04.2021

Darmstadt 2021  
D17

Witt, Marcus Ulf: Poly-N-isopropylacrylamide Based Microgels, A Study on Magnetic  
Microgels and Their Structure

Darmstadt, Technische Universität Darmstadt

Jahr der Veröffentlichung der Dissertation auf TUprints: 2021

URN: urn:nbn:de:tuda-tuprints-185638

URL: <https://tuprints.ulb.tu-darmstadt.de/id/eprint/18563>

Tag der mündlichen Prüfung: 21.04.2021

Veröffentlicht unter CC-BY-NC-SA 4.0 International

<https://creativecommons.org/licenses/>



TECHNISCHE  
UNIVERSITÄT  
DARMSTADT

## **Erklärung gemäss §9 Promotionsordnung**

Hiermit versichere ich, dass die vorliegende Dissertation von mir selbstständig angefertigt wurde und keine anderen Quellen und Hilfsmittel verwendet wurden als angegeben. Alle Zitate wurden angemessen kenntlich gemacht. Die Dissertation wurde bisher zu keiner Prüfung verwendet.

-----  
Datum, Unterschrift

# Wissenschaftlicher Werdegang

- 04/2017 - heute**      Wissenschaftlicher Mitarbeiter am Institut für Physik kondensierter Materie an der Technischen Universität Darmstadt  
AG Prof. Dr. Regine von Klitzing
- 01/2014 - 03/2017**      Wissenschaftlicher Mitarbeiter am Institut für Chemie an der Technischen Universität Berlin  
AG Prof. Dr. Regine von Klitzing
- 11/2011 - 10/2013**      Studium der Physik (M. Sc.) an der Freien Universität Berlin  
Schwerpunkt: Festkörperphysik/Nanophysik  
Titel der Masterarbeit: Selective Enrichment of Carbon Nanotube Chiralities due to Different Amphiphiles  
AG Prof. Dr. Stephanie Reich
- 10/2008 - 10/2011**      Studium der Physik (B. Sc.) an der Freien Universität Berlin  
Titel der Bachelorarbeit: Carbon Nanotube Dependent Selective Affinity of Different Polyglycerol Amphiphiles versus SDBS Replacment  
AG Prof. Dr. Stephanie Reich
- 2005 - 2008**              Ausbildung zum chemisch-technischen Assistenten am OSZ für Naturwissenschaften der Lise-Meitner-Oberschule Berlin  
Titel der Abschlussarbeit: Synthese von Capsaicin mit Qualitätskontrolle

# Wissenschaftliche Veröffentlichungen

## Publikationen als Erstautor

Distribution of  $CoFe_2O_4$  Nanoparticles Inside PNIPAM-Based Microgels of Different Cross-linker Distributions, Marcus U. Witt, Stephan Hinrichs, Nadir Möller, Sebastian Friedrich, Birgit Fischer, and Regine von Klitzing, *The Journal of Physical Chemistry B* (2019), 123 (10), 2405-2413, DOI: 10.1021/acs.jpccb.8b09236

## Ausstehende Publikation als Erstautor

Magnetic Response of  $CoFe_2O_4$  Nanoparticles Confined in Microgel Meshes, Marcus U. Witt, Joachim Landers, Stephan Hinrichs, Soma Salamon, Juri Kopp, Birgit Hankiewicz, Heiko Wende, and Regine von Klitzing, *Soft Matter* (2021)

## Publikationen als Koautor

Loading of PNIPAM Based Microgels with  $CoFe_2O_4$  Nanoparticles and their Magnetic Response in Bulk and at Surfaces, Sebastian Friedrich, Marcus U. Witt, Eric Roeben, Lucas Kuhrts, Sarah Aleed, Annette M. Schmidt and Regine von Klitzing, *The Journal of Physical Chemistry. B* (2015), 119 (36), 12129-12137, DOI: 10.1021/acs.jpccb.5b03778

Poly(*N*-isopropylacrylamide) Microgels under Alcoholic Intoxication: When a LCST Polymer Shows Swelling with Increasing Temperature, Sebastian Friedrich, Patrick Krause, Weronika Tabaka, Marcus U. Witt, Debashish Mukherji, Kurt Kremer and Regine von Klitzing, *ACS Macro Lett.* (2017), 6 (10), 1042-1046, DOI: 10.1021/acsmacrolett.7b00557

Combined Cononsolvency and Temperature Effects on Adsorbed PNIPAM Microgels, Sebastian Friedrich, Patrick Krause, Weronika Tabaka, Marcus U Witt, Regine von Klitzing, *Langmuir* (2017), 33 (50), 14269-14277, DOI:10.1021/acs.langmuir.7b02903

Externally Triggered Oscillatory Structural Forces, Sebastian Schön, Marcel Richter, Marcus U. Witt and Regine von Klitzing, *Langmuir* (2018), 34 (38), 11526-11533, DOI: 10.1021/acs.langmuir.8b02284

Bridging the gap between two different scaling laws for structuring of liquids under geometrical confinement, Michael Ludwig, Marcus U. Witt and Regine von Klitzing, *Advances in Colloid and Interface Science* (2019), 269, 270-276, DOI: 10.1016/j.cis.2019.04.012

A comparison of the network structure and inner dynamics of homogeneously and heterogeneously crosslinked PNIPAM microgels with high crosslinker content, Judith Witte, Tetyana Kyrey, Jana Lutzki, Anna Margarethe Dahl, Judith Houston, Aurel Radulescu, Vitaliy Pipich, Laura Stingaciu, Matthias Kühnhammer, Marcus U. Witt, Regine von Klitzing, Olaf Holderer and Stefan Wellert, *Soft Matter* (2019), 15, 1053-1064, DOI:10.1039/C8SM02141D

Inner structure and dynamics of microgels with low and medium crosslinker content prepared via surfactant-free precipitation polymerization and continuous monomer feeding approach, Tetyana Kyrey, Judith Witte, Artem Feoktystov, Vitaliy Pipich, Baohu Wu, Stefano Pasini, Aurel Radulescu, Marcus U. Witt, Margarita Kruteva, Regine von Klitzing, Stefan Wellert and Olaf Holderer, *Soft Matter* (2019), 32, DOI:10.1039/C9SM01161G

# Contents

<b>1</b>	<b>Introduction</b>	<b>1</b>
<b>2</b>	<b>Theoretical Background</b>	<b>3</b>
2.1	Microgels . . . . .	3
2.2	Magnetism of Magnetic Nanoparticles . . . . .	5
2.3	Measurement Techniques . . . . .	13
<b>3</b>	<b>Experimental Section</b>	<b>22</b>
3.1	Chemicals . . . . .	22
3.2	Samples . . . . .	22
3.3	Experimental Methods . . . . .	26
<b>4</b>	<b>Loading of PNIPAM Based Microgels with <math>CoFe_2O_4</math> Nanoparticles and their Magnetic Response in Bulk and at Surfaces</b>	<b>31</b>
4.1	Abstract . . . . .	31
4.2	Introduction . . . . .	32
4.3	Results . . . . .	33
4.4	Discussion . . . . .	40
4.5	Conclusion . . . . .	42
<b>5</b>	<b>Kinetics of Microgel Formation</b>	<b>43</b>
5.1	Abstract . . . . .	43
5.2	Introduction . . . . .	43
5.3	Results . . . . .	44
5.4	Discussion . . . . .	48
5.5	Conclusion . . . . .	50
<b>6</b>	<b>Distribution of <math>CoFe_2O_4</math> Nanoparticles Inside PNIPAM Based Microgels of Different Cross-Linker Distributions</b>	<b>51</b>
6.1	Abstract . . . . .	51
6.2	Introduction . . . . .	52
6.3	Results . . . . .	53
6.4	Discussion . . . . .	58
6.5	Conclusion . . . . .	64
<b>7</b>	<b>Magnetic Response of <math>CoFe_2O_4</math> Nanoparticles Confined in Microgel Meshes</b>	<b>65</b>
7.1	Abstract . . . . .	65
7.2	Introduction . . . . .	66

7.3	Results and Discussion . . . . .	66
7.4	Summary and Conclusion . . . . .	82
<b>8</b>	<b>Conclusion and Future Work</b>	<b>83</b>
8.1	Conclusion . . . . .	83
8.2	Future Work . . . . .	84
<b>9</b>	<b>Danksagung</b>	<b>85</b>
<b>10</b>	<b>Abbreviations</b>	<b>87</b>
<b>11</b>	<b>Appendix</b>	<b>100</b>
11.1	Magnetic Microgels: Different Approaches via Synthesis . . . . .	100
11.2	Allyl Mercaptane as "Glue" . . . . .	102
11.3	Dynamic Light Scattering with Magnetic Field . . . . .	104

# 1 Introduction

*N*-isopropylacrylamid (NIPAM) microgels are widely used as responsive polymers. Responsive polymers are of high interest for many applications such as medicine, smart fabrics, sensors, actuators and surface coatings. Polymerizing NIPAM with a cross-linker ,e.g. with *N,N'*-Methylenbisacrylamide (BIS), results in a gel. This study focuses on NIPAM based microgels (MG) and their combination with magnetic nanoparticles (MNP). Poly-NIPAM (PNIPAM) based microgels are of high interest due to their swelling and shrinking behavior. PNIPAM is easily dispersed in water below 32 °C, hence the description in literature as a hydrogel. Above 32 °C water becomes a bad solvent and the microgels shrink. Reducing the temperature below 32 °C the microgels swell [41, 44, 60, 79, 93, 121]. Furthermore, microgels respond faster to temperature changes compared to macrogels. They react faster because their equilibration time is shorter due to the smaller temperature gradient inside [121].

PNIPAM microgels are used as model systems for surface coatings [5], actuators, sensors [91, 103, 106], medical applications [66, 113] or drug delivery systems [11, 28]. Some more examples are humidity [77], glucose sensors [116], micro reactors [46] or model systems for concentrated colloidal systems [79, 127]. Modified microgels with different moieties show that the volume phase transition (VPT) can be triggered with other stimuli than temperature, e.g. pH [1, 8, 12, 59, 72, 114] or ionic strength [74, 78]. Also the mechanical properties can be influenced by changing the amount or distribution of cross-linker [2, 81].

Incorporating metallic nanoparticles (NPs) leads to applications in catalysis [111]. They can also introduce responsiveness to other stimuli, e.g. with gold NPs the MGs become sensitive to light [39, 45, 57, 71, 75, 76] or with TiO<sub>2</sub> they can detox drinking water [109]. In this thesis magnetic NPs were used to introduce a response to external magnetic fields. Such magnetic microgels can be heated [7, 69, 129] or deformed [17, 51, 99, 101]. Often the magnetic microgels have a core/shell structure with either a single magnetic core or an agglomerate of several smaller MNPs [25, 26, 48, 83, 86, 90, 97]. Infrequent a reversed core/shell structure is described (polymer core and magnetic shell) [50, 55]. The above mentioned distributions of magnetic material show polymer volume that is not affected by the magnetic material. This thesis aims to reduce this non-reactive volume.

The thesis addresses the MNP distribution for the combination of NIPAM based microgels and *CoFe<sub>2</sub>O<sub>4</sub>* MNPs. The advantage of homogeneously distributed MNPs inside the polymer matrix is the higher volume affected by the MNPs. Increasing the number of MNPs is desired because more MNPs results in a larger effected volume. Their increasing number is limited by the fact that the resulting MMGs are still responsive to temperature changes.

*Chapter 4* addresses test combinations of MNPs and MGs. For the combinations four

microgels were tested, one negatively charged (close to neutral) and three positively charged with increasing amount of AA (positively charge co-monomer). The MGs and the MMGs were studied due to their swelling and shrinking behavior with dynamic light scattering (DLS), measurements of the electrophoretic mobility (EM), atomic force microscopy (AFM) and transmission electron microscopy (TEM). Furthermore, the MMGs were exposed to external magnetic fields.

To increase the response of the MMG from *Chapter 4*, the microgel structure is varied by different synthesis methods in *Chapter 5*. The following three methods were tested: the batch method (all reactants in one reaction vessel), the feeding method (the reactants are fed into the reaction vessel) and the semi-batch method (a combination of the two previous mentioned). In this chapter the microgels were analyzed with DLS and the EM was measured. Additionally two kinds of microgels were monitored with mass spectrometry during the reaction time to calculate reaction rate constants.

*Chapter 6* uses the information from the previous two chapters to create MMG with a much higher loading with MNPs. Two microgels were polymerized, one with the batch method and the other with the feeding method. Beside the standard analysis with DLS and the measurement of the EM the MGs were imaged with the AFM. Additionally the elastic modulus of the MGs was measured locally over the whole particle size. The data can be used to determine the cross-linker distribution inside the microgels. The two microgels were then loaded with MNP. The MG and the MMG were imaged with a TEM. From the images the distribution of cross-linker and MNPs was derived.

In *Chapter 7* the hydrophobic moiety allyl mercaptan (AM) was polymerized into one type of microgel. This type of microgel was compared with the one without AM to see the influence on the microgel properties and the loading with MNPs. Additionally, magnetic measurements were performed by Joachim Landers (AG Wende, University Duisburg) to measure the magnetic properties of the MMGs. Therefore, ZFC-FC magnetization and AC-susceptibility measurements were done. The Brownian magnetic relaxation is correlated to the viscosity of the environment of the MNPs and MMGs. The viscosity is used as a measure for the interaction strength between the MNPs and the microgel matrix. This is of high interest for a tunable sensitivity.

## 2 Theoretical Background

This thesis addresses the combination of microgels with magnetic nanoparticles. The first section of the theoretical background introduces microgels and their properties. This is followed by an introduction to magnetism and magnetic nanoparticles. Afterwards, the underlying physics of the applied measurement techniques is described.

### 2.1 Microgels

As the term microgel indicates their typical size is below a few micrometers. A gel consists of two phases. In the studied system the gel consists of a cross-linked polymer network and water.

The synthesis of microgels from *N*-Isopropylacrylamide (NIPAM) was first reported by Tanaka *et al.* and Pelton *et al.* [93,95,126]. They reported the radical precipitation polymerization from NIPAM to Poly-NIPAM (PNIPAM) gels.

In general, the cross-linking can be realized in different ways. For example via covalent bounds or physical entanglement. The concentration and distribution of cross-linker plays an important role in the microgel properties such as their elastic modulus [118]. Some microgels form hydrogen bonds if dispersed in water. Such microgels are often called hydrogels in literature to highlight this property. Hydrogels are of high interest as they show properties that are related to water and properties that are related to the polymers. In the gel the volume occupied by the solvent can go up to 99.7 % of the total volume [29]. Adding the solvent to the dry microgel leads to a swelling of the microgel. The swelling is driven by the interaction strength between the polymer matrix and the solvent. The swelling capacity is influenced by various parameters such as the network cross-linker density and distribution as well as the polarity of the solvent. Some gels are reactive to external stimuli such as the surrounding temperature [42,44,60,79,93], pH [9,59,73,115], ionic strength [74,78], light [39,45,57,71,75,76] and electric or magnetic fields [27]. Tanaka reported in 1978, a large change in particle volume with increasing temperature [120]. The observed volume change is illustrated in *Figure 2.1*.

Microgel systems have the advantage that they react faster to external stimuli changes compared to macrogels. This faster response originates in the smaller length scale of the temperature deviation inside the system [6]. In addition the surface to volume ratio is increased for microgels (MGs). This is discussed in more detail in the following chapters.

The microgels synthesized in this study consist of the monomer NIPAM and the cross-linker *N,N'*-Methylenbisacrylamide (BIS). The hydrophobicity of the monomer NIPAM increases with increasing temperature. This behavior of NIPAM is similar to ethylene oxide [40]. This influences the solubility of NIPAM based polymers and they show a lower critical solution temperature (LCST). Above this LCST the polymer separates

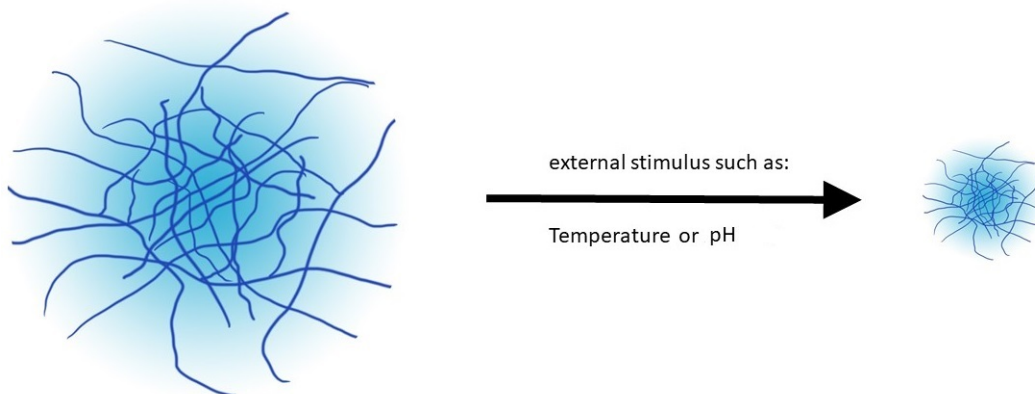


Figure 2.1: Illustration of the VPT for microgels, triggered by external stimuli.

from the water phase. Other polymers show a similar but reversed behavior called upper critical solution temperature (UCST), where the phase separation occurs below a certain temperature. *Figure 2.2* shows the LCST and UCST in separate phase diagrams.

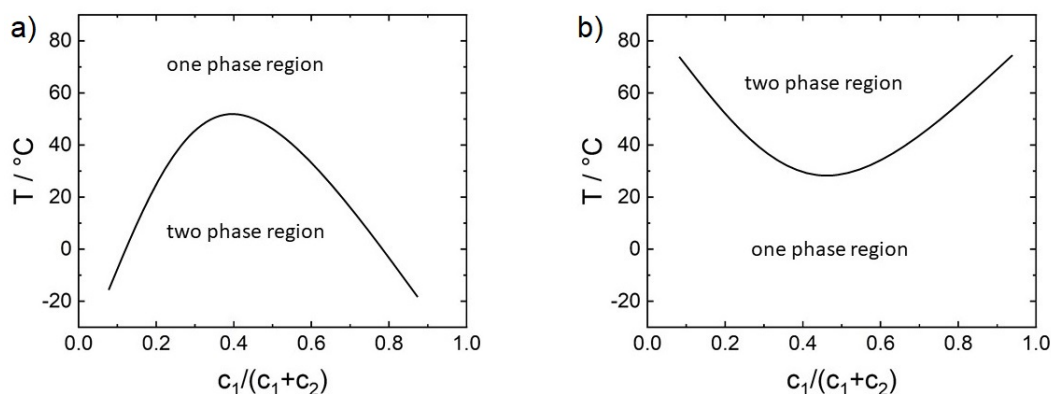


Figure 2.2: Schematic phase diagrams of two component mixtures that show a UCST (a) and a LCST (b)). With the mole fraction of substance 1 on the x-axis.

For PNIPAM microgels the LCST becomes visible by a volume phase transition (VPT). For PNIPAM microgels water is a good solvent at temperatures below  $32\text{ }^{\circ}\text{C}$  due to the formation of hydrogen bonds between water and MG. This leads to a swelling of the polymer network. With increasing temperature the ratio between broken hydrogen bonds and new formed ones increases. By crossing the volume phase transition temperature (VPPT) water becomes a bad solvent and is pressed out of the microgel, the microgel shrinks. How extensive this swelling/shrinking is, depends on several factors such as the network stiffness (cross-linker concentration) and the network structure (cross-linker distribution and co-monomer content and distribution). From the swollen

and shrunken size the swelling ratio  $\alpha$  can be calculated:

$$\alpha = \frac{V_H(20\text{ }^\circ\text{C})}{V_H(50\text{ }^\circ\text{C})} = \frac{r_H^3(20\text{ }^\circ\text{C})}{r_H^3(50\text{ }^\circ\text{C})}. \quad (2.1)$$

$V_H$  is the hydrodynamic volume and  $r_H$  the hydrodynamic radius at a given temperature.

The microgel swelling and shrinking can be described by the Flory-Rehner theory [85]. In this theory, the free energy of the gel is defined as the sum of the mixing energy, the elasticity energy and the electrostatic energy from the network  $E_{gel} = E_{mix} + E_{elast} + E_{elec}$ . The shrinking of the gel changes the internal osmotic pressure  $\Pi_{gel}$ . The osmotic pressure can be derived from the energy:

$$-\left(\frac{\partial E}{\partial V}\right)_T = \Pi_{gel} = \Pi_{mix} + \Pi_{elast} + \Pi_{elec}. \quad (2.2)$$

The individual contributions of the osmotic pressure can be expressed as:

$$\Pi_{mix} = -\frac{N_A k_B T}{v} (\phi + \ln(1 - \phi) + \chi \phi^2) \quad (2.3)$$

$$\Pi_{elast} = -\frac{N_c k_B T}{V_0} \left( \frac{\phi}{2\phi_0} - \frac{\phi^{1/3}}{\phi_0} \right) \quad (2.4)$$

$$\Pi_{elec} = \frac{f N_c k_B T}{V_0} \frac{\phi}{\phi_0} \quad (2.5)$$

with  $V$  the volume,  $V_0$  the volume of the relaxed Gaussian gel network,  $N_A$  the Avogadro constant,  $v$  the molar volume of the solvent,  $\phi$  the volume fraction of the polymer,  $\phi_0$  the volume fraction of the polymer at reference conditions,  $N_c$  the number of chains in the gel network,  $f$  the number of counter ions per chain,  $\chi$  the Flory-Huggins parameter [10] and  $k_B$  the Boltzmann constant. During a collision between the solvent molecules and the gel particle, energy is transferred:

$$\chi = \frac{\Delta E}{k_B T} = \frac{\Delta H - T \Delta S}{k_B T}. \quad (2.6)$$

$\Delta H$  and  $\Delta S$  are the change in enthalpy and entropy of the monomer segments.

## 2.2 Magnetism of Magnetic Nanoparticles

Magnetic materials can be divided into several classes and sub classes. The three main classes are defined by the permeability ( $\mu_r$ ) of the materials. With  $0 \leq \mu_r < 1$ , the material is considered as diamagnetic. Diamagnetic materials are repelled from external magnetic fields. All materials are diamagnetic. For some materials the diamagnetic properties are over compensated by their paramagnetic properties. A material is considered paramagnetic if  $\mu_r > 1$ . Opposing to a diamagnetic material, a paramagnetic material is attracted by an external magnetic fields. If the permeability is much larger

( $\mu_r \gg 1$ ), the material is considered to be ferromagnetic. The most prominent ferromagnetic materials are Iron, Nickel and Cobalt.

Magnetic materials show an easy and hard direction if they have a spontaneous magnetization and more than one symmetry axis. The easy direction is the lowest energy level for the magnetization while the hard direction is the highest stable energy level. This can be described by magnetic anisotropy. One major magnetic anisotropy originates from the spin-orbit coupling and is called the magnetocrystalline anisotropy. *Figure 2.3* shows schematically two elongated magnetic particles with different crystal structures. In a) is the [001] direction parallel to the long axis of the particle and in b) it is tilted. For cobalt ferrite particles the easy direction points in the [001] direction [128]. The magnetic moment in such materials originates from the spin angular momentum  $\vec{S}$  of unpaired electrons. The orbital angular momentum  $\vec{L}$  is pointing in the direction of the crystal axes towards the highest probability densities of electrons. The spin-orbit coupling depends on the orientation of the magnetization relative to the crystal lattice symmetry axis. For systems with a single high symmetry axis, the magnetic anisotropy is uniaxial.

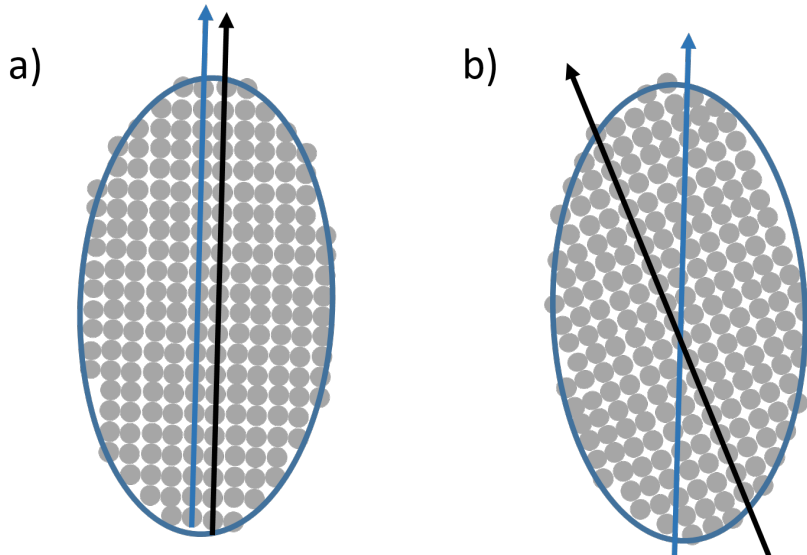


Figure 2.3: Schematic depiction of a magnetic particles with the long particle axis as a blue arrow and the [001] crystal direction as a black arrow. In a) is the crystal direction [001] parallel to the long particle axis and in b) it is tilted.

One part of the magnetic anisotropy energy originates from the particle shape, called shape anisotropy energy ( $E_{shape}$ ). The shape anisotropy energy is given by:

$$E_{shape} = V \frac{\mu_0}{2} \vec{M} \underline{N} \vec{M} = V \frac{\mu_0}{2} \sum_i N_i M_i^2 = V K_{shape} \quad (2.7)$$

with  $\underline{N}$  being the diagonalized demagnetization tensor [92] with  $\sum N_i = 1$ ,  $\vec{M}$  the magnetization and  $\mu_0$  the vacuum permeability. For an ideal spherical object the shape

anisotropy energy becomes zero. The elements of  $\underline{N}$  depend on the particle structure. For spherical particles with no preferred magnetization direction the value is  $N_i = 1/3$ . For small particles an additional anisotropy energy contributes, the surface anisotropy energy. The surface anisotropy ( $E_{surf}$ ) increases with decreasing particle size. The ratio of surface area versus volume increases with decreasing particle size. The surface anisotropy is given by:

$$E_{surf} = \frac{6K_s}{d} \quad (2.8)$$

with  $d$  as the particle diameter and  $K_s$  as the surface anisotropy constant. The orientation of the atomic magnetic moments are disturbed by surface effects. As the particle surface can be considered as a thin layer with negligible curvature, the atomic magnetic moments tend to arrange in plane. All the described anisotropy energies can be described by introducing the effective magnetic anisotropy constant  $K_{eff}$ . For nanoparticles smaller than 20 nm, the magnetocrystalline anisotropy plays an inferior role for the magnetic anisotropy energy. For spherical particles, every surface defect results in an increasing contribution via the uniaxial anisotropy parallel to the defect axes of the particle. In literature it has been reported that the anisotropy energy can be derived from [124]:

$$E_A = VK_{eff} \sin^2 \theta \quad (2.9)$$

for such cases.  $K_{eff}$  is calculated from the contributions of shape and surface anisotropy and  $\theta$  the angle between the easy axis and the magnetization:

$$K_{eff} = K_{shape} + \frac{6}{d}K_s. \quad (2.10)$$

Beside the particle properties, the magnetic orientation is also influenced by the environment and neighboring magnetic particles. Some interactions, such as the magnetic exchange interaction [18], can be neglected in a dispersion due to the large distance between the individual magnetic particles. The distance between such particles is too large for such short ranged interactions. The magnetic dipole interaction is more relevant in such cases. *Equation 2.11* gives the maximum of the dipole interaction energy between two magnetic particles in distance  $d$  and with a net magnetic moment for the particles  $\mu_{part}$ . The total energy of the magnetic dipole interaction depends on the local configuration. The dipole energy is given by:

$$E_{Dipole} \approx \frac{\mu_0 \mu_{part}^2}{4\pi d^3}. \quad (2.11)$$

Besides the anisotropy energy, other particle properties are as well influenced by the size. For example some systems have a decreasing saturation magnetization for increasing particle size [105]. Additionally, the probability of oxidation also increases with decreasing particle size. Some particles such as magnetite are less effected in the course of the oxidation to maghemite. The change of magnetic properties is small compared

to the difference between magnetite and pure iron particles. The magnetite can oxidize into different magnetic materials that are either ferri- or antiferromagnetic.

Coating magnetic particles for stabilization has additional benefits. The coating reduces the migration of oxygen towards the particle and therefore hinders the oxidative degradation. In contrast, the high surface to volume ratio makes the particles highly suitable candidates for catalysis. But most used catalysis particles are non magnetic. Never the less they may be used as Janus particles or in a core/shell configuration.

Surface effects of magnetic nanoparticles are important for their static properties. They are also interesting for the magnetization dynamics. One prominent phenomenon is the thermally excited fluctuation of the particles superspin which is called superparamagnetism. The superspin is the combination of all coherent fluctuating magnetic moments in ferromagnetic single domain particles, it is also referred to as the particle magnetic moment.

### 2.2.1 Superparamagnetism

For ferromagnetic particles that are single-domain particles, the magnetic anisotropy energy can be derived from  $E_A = K_{eff}V_C$  with  $V_C$  as the volume of the magnetic core. This energy is similar to the thermal energy given as  $E_{thermal} = k_B T$ , because the core volume is small ( $k_B$  as the Boltzmann constant and  $T$  the temperature in Kelvin). The Stoner-Wohlfarth model shows for non interacting magnetic nanoparticles (MNPs) that they have an uniaxial magnetic anisotropy [30]. While the model is simple, it is also very suitable for experimental applications. The smallest deviation from perfect spherical particles results in the above discussed shape anisotropy. *Equation 2.9* gives two minima for the particle energy, separated by an energy barrier of  $E_A$ . Néel [84] proposed a model in which the thermal excitation results in a randomized magnetic moment. The magnetic moment switches between the two minima on a short time scale. The time scale is given as:

$$\tau_{Neel} = \tau_0 \exp\left(\frac{K_{eff}V_c}{k_B T}\right). \quad (2.12)$$

$\tau_0$  is the intrinsic time constant in which the superspin can change its orientation.  $\tau_{Neel}$  is minimal when the magnetic anisotropy energy is zero. With no magnetic anisotropy barrier, the flipping frequency  $\tau_0^{-1}$  of the superspin between both states becomes high. For energy barriers that are non negligible, *Equation 2.12* shows an Arrhenius-like behavior. This is well known for processes that are thermally driven and include an energy barrier.  $\tau_{Neel}$  directly determines, if an experimental setup measures a magnetically blocked or superparamagnetic behavior. The system appears superparamagnetic for measuring times slower than  $\tau_{Neel}$ , as the time averaged magnetic moment becomes zero. For measurements that are faster than  $(\tau_{Neel})^{-1}$ , the magnetic moment appears to be blocked. Such a sample can still be interpreted for its temperature and field-dependent magnetization by paramagnetic behavior. One exception of the paramagnetic behavior can be an extraordinary high magnetic moment, that can be well above  $10^5 \mu_B$  ( $\mu_B$  is the Bohr magneton). This highly depends on the particle size.

A common misunderstanding is that there is some sort of thermodynamic phase transition between the magnetically blocked and the superparamagnetic state. The transition between these states is continuous, the relaxation rate increases with increasing temperature. The MNP is considered superparamagnetic if the relaxation rate is faster than the probing rate of the measurement. In literature, the temperature where the probing frequency exceeds the fluctuation rate is called blocking temperature ( $T_B$ ). The blocking temperature can be directly derived from *Equation 2.12*:

$$T_B = \frac{K_{eff}V}{k_B\Phi}, \Phi = \ln\left(\frac{\tau_M}{\tau_0}\right) \quad (2.13)$$

with  $\tau_M$  denoting the time resolution of the measuring device. The time resolution of the devices can vary by several orders of magnitude.

For example, the super quantum interference device (SQUID) magnetometer used in this study takes 10 s to measure the net magnetic moment in field direction, while the extension, the AC-susceptometer, is limited by the applied AC magnetic field with a time resolution of microseconds. Therefore, it is important to keep the used measurement device in mind when comparing blocking temperatures.

For a better understanding of the magnetic relaxation dynamics, the model developed by Néel has to be improved. Brown [23] found a good estimation of the relaxation prefactor  $\tau_0$  and its temperature dependence.  $\tau_0$  was found to be between  $10^{-12}$  and  $10^{-9}$  depending on the measured particle system [108]. Also the influence of other parameters beside the temperature has been studied. Such studied system includes the amplitude of the applied fields, the magnetic ordering and the magnetic dipole interaction [49, 123]. For more complex systems a more sophisticated model such as the Vogel-Fulcher model is needed:

$$\tau_{Neel} = \tau_0 \exp\left(\frac{K_{eff}V}{k_B(T - T_0)}\right), T_0 = \frac{E_{dip}}{k_B} \approx \frac{\mu_0\mu_{NP}^2}{4\pi D^3 k_B}. \quad (2.14)$$

$\mu_{NP}$  is the magnetic moment of the nanoparticles and  $D$  the distance between two interacting magnetic cores.  $T_0$  is therefore a measure for the interaction energy  $E_{dip}$ .

The superparamagnetic nanoparticles are of high interest because of their tunability between long-range magnetic ordering or quasi-paramagnetic behavior by changing the magnetic core volume. The superparamagnetic behavior, that can be expressed as the free coherent reorientation of the magnetic moments, is not only related to the Néel relaxation. The Néel relaxation describes the reorientation of the magnetic moment while the magnetic particle is fixed in space. The reorientation of the magnetic moment can also happen by reorienting the whole magnetic nanoparticle. This reorientation is driven by rotational and translational Brownian motion, called Brownian relaxation. *Figure 2.4* shows both processes in a scheme.

## 2.2.2 Brownian Relaxation

The Brownian relaxation time is influenced by several parameters such as the particle size and the viscosity of the environment. The Brownian relaxation is driven by translation

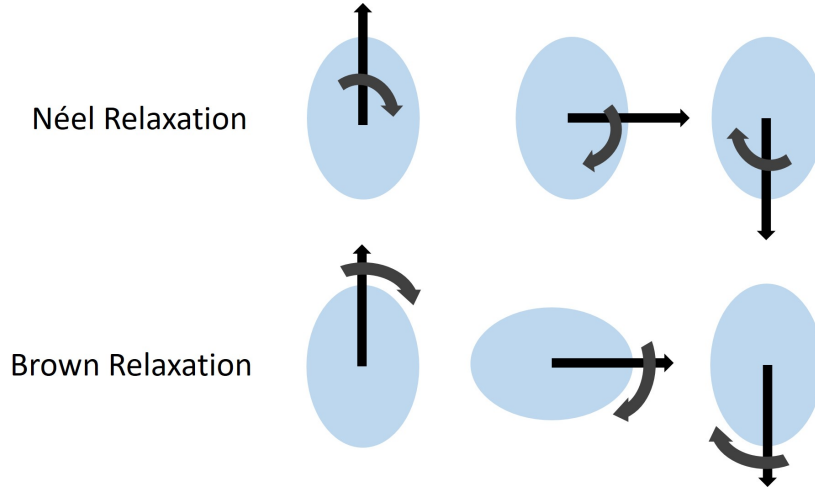


Figure 2.4: Schematic depiction of the two main magnetic relaxation processes. For the Néel relaxation the magnetic moment rotates, while for the Brownian relaxation the particle rotates.

and rotational diffusion due to the collision of the magnetic particles with the molecules of the environment. While the origin of the Néel and Brownian relaxation is different, both of them result in the reorientation of the magnetic moment. In literature, the Brownian relaxation of ferrofluidic systems without a net magnetization is called pseudo-superparamagnetism [63]. The Brownian motion was described by Einstein in 1905 by solving the Focker-Planck-equation to evaluate the progression of the probability function of separate particles [32]. Von Smoluchowski further developed the understanding of the Brownian motion by studying the distance traveled by particles at different time scales [122]. Two years later Langevin approached the phenomenon with a randomly directed complementary force. This gives a simple and more illustrative picture of the molecule collisions on the particles surface, resulting in the same mean square displacement as derived from Einstein [68]. In this study the model proposed by Langevin is used to describe the superparamagnetic behavior originating from Brownian relaxation.

For spherical particles in a Newtonian fluid and at thermal equilibrium the energy is proportional to  $k_B T/2$  for every degree of motional freedom derived from the equipartition theorem. The mean square velocity becomes

$$\overline{v^2} = \frac{3k_B T}{m_{NP}} \quad (2.15)$$

with  $m_{NP}$  as the mass of the nanoparticle. For iron oxide nanoparticles with a hydrodynamic radius of 10 nm (in water) the mean velocity is  $\sqrt{\overline{v^2}} \approx 1$  m/s, while the much smaller water molecules are moving with 600 m/s. Therefore, the observed particles can be considered as quasi static in water. For each collision of the water molecules with the particle surface, the particle momentum changes miniscular. Due to the high number of water molecules surrounding the particle and the resulting high collision rate (up to

$10^{15}$  collisions per second), this effect accumulates. The collision of the water molecules with the particle does not result in a preferred direction for the momentum transfer, thus resulting in a rather complex shivering of the particle. The motion is ballistic for smaller distances than the particle diameter. The model assumes that the rate of randomized momentum transfer can be considered as a continuous force acting upon the particles ( $F_x$ ). The time scale for such a force is long compared to the collision time, but considerably faster compared to the time scales relevant for diffusive motion of the particle. An additional force is acting on the particles resulting in a deceleration. The force is given by the Stokes friction that is proportional to the particle velocity and viscosity of the surrounding medium. The translational friction coefficient is  $\gamma_t = 6\pi\eta r_H$ , with  $\eta$  being the viscosity of the medium and  $r_H$  the hydrodynamic radius. The diffusive motion of the particle can then be calculated from the equation of motion

$$m \frac{d^2x}{dt^2} = -6\pi\eta r_H \frac{dx}{dt} + F_x = \gamma_t \frac{dx}{dt} + F_x. \quad (2.16)$$

As the direction of  $F_x$  is randomly averaged over a large amount of particles the averaged force  $F_x$  approaches zero. With this, the differential equation of motion can be solved with a simple exponential function. The mean square displacement at the time  $t'$  can be expressed as

$$\overline{\Delta x^2} = \frac{2k_B T}{\gamma_t} * t'. \quad (2.17)$$

This can further be simplified by using the Stokes-Einstein equation

$$D = \frac{k_B T}{6\pi\eta r_H} \quad (2.18)$$

to

$$\overline{\Delta r^2} = 6D_t t' \quad (2.19)$$

with  $D$  as the diffusion coefficient. For example, the traveled distance of the above described iron oxide particle in 1 *ns* in 3-dimensions with a water viscosity of  $\eta \approx 10^{-3}$  *Pa s* is just 0.4 *nm*. Important to note is, that the ballistic motion depends on the particle mass the diffusive motion does not. The diffusive motion rather depends on the temperature, medium viscosity and particle size. Besides the translation momentum transfer, the collision between particle and surrounding medium molecules also induces a transfer of torque. This results in translational and rotational motion. The mean squared angle ( $\overline{\Delta \Theta^2}$ ) can be calculated similar to the mean square displacement with the introduction of the rotational friction coefficient ( $\gamma_{rot}$ ) [33]. In relation to the translational motion, the rotational motion can be expressed by:

$$D_{rot} = \frac{k_B T}{8\pi\eta r_H^3} \quad (2.20)$$

$$\overline{\Delta \Theta^2} = 6D_{rot} t'. \quad (2.21)$$

The Brownian rotational motion of the particles is related to the phenomena of superparamagnetism of the magnetic particles. From this a time constant of the Brownian rotation can be calculated where the aligned magnetic moments relax to a net magnetic moment of zero, given by:

$$\tau_{rot} = \frac{1}{2D_{rot}} = \frac{4\pi\eta r^3}{k_B T}. \quad (2.22)$$

The velocity of the Brownian motion strongly depends on the friction coefficients. These coefficients are determined from the hydrodynamic radius and the dynamic viscosity.

### 2.2.3 Magnetic Microgels and Entrapped Magnetic Particles

So far the magnetic particle motion and the magnetic relaxation was described in Newtonian fluids with rather low particle concentrations. However, a broad range of application uses the combination of magnetic particles in non-Newtonian fluids or as in this study in elastic matrices. Such systems are of high interest for technological and medical applications as motivated in *Chapter 1*. The structure of such a matrix is mostly inhomogeneous on the nano- or macroscale. Such a structure influences the translational and rotational motion. The dynamic viscosity of the environment is not sufficient anymore to describe the system. The spacial restrictions of the magnetic particles may result in a directed motion or rotation. Furthermore, the mobility of the particles may be influenced by additional parameters, as the matrix is reacting upon these parameters and changing the constraints. Such a particle movement is shown in *Figure 2.5*. The particle position is depicted as a dot for equidistant time steps starting with the black dot. Part a) shows the Brownian motion of a free particle. Part b) shows the particle motion according to Brown with spacial constraints induced from the matrix.

*Figure 2.5* shows the particle position for 100 time steps. The first 10 in red and the rest in green. The area covered by the particle is also shown. While for small time scales the spacial constraints from the matrix may not influence the particle movement, this changes drastically with increasing observed time. For large time scales (green dots), the particle movement is restricted by the mesh size. The mean square displacement is shown in the figure with  $\Delta_{10}$  and  $\Delta_{100}$  for the 10 and 100 time steps. For time scales even larger as depicted here, the mean square displacement is expected to saturate. Again the observed behavior is sensitive to the applied measurements. For fast measurements, the particle motion will be the same as for free particles. For slow measurements, the observed particle motion will be hindered and an effective viscosity may be calculated [13, 31].

The magnetic microgels (MMGs) are also reactive to constant magnetic fields. In experiments with non homogeneous magnetic fields (from a permanent magnet) the MMGs were separated from the dispersion medium [98, 101]. The magnetic particles are oriented in field direction and are moving towards the lowest energy level, towards the magnet. MMGs that are adsorbed on a surface can be deformed by external magnetic fields. Similar to the separation experiments the magnetic particles are reorienting in field direction. For non homogeneous fields they even want to move. This movement is

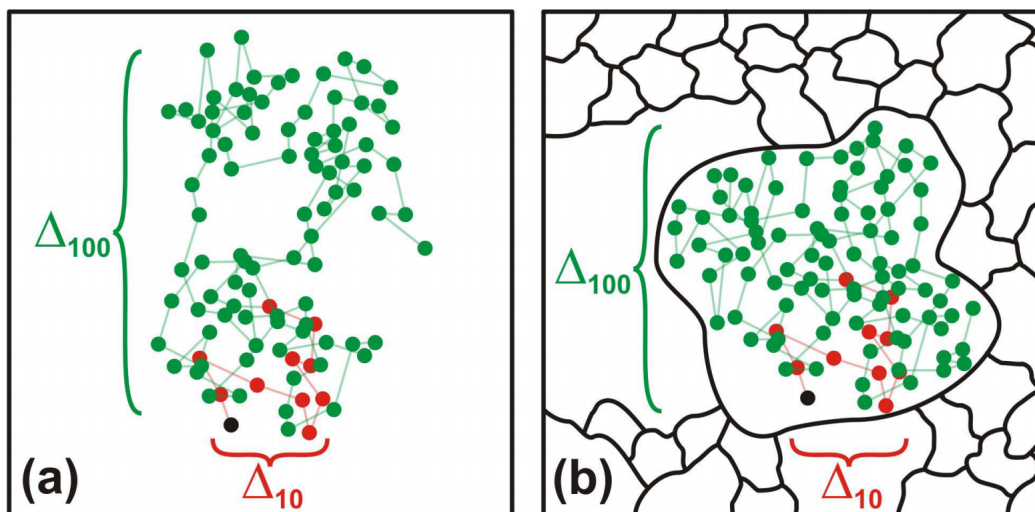


Figure 2.5: Sketch of particle position for equidistant time steps for free Brownian motion in a) and spacial constrains such as a polymer matrix in b). The particle position at time zero is black. The first ten time steps are colored in red. The next 90 time steps are colored in green. Reprinted from Joachim Landers [67].

hindered by the polymer matrix of the microgel. This introduces deformations to the gel matrix. This deformation can also originate from the rotation of the magnetic particles, e.g. non spherical particles (ellipsoids) or spherical particles that have a high interaction strength to the surrounding matrix (covalent bound) [47, 99, 101].

The response of the MMG to external magnetic fields is influenced by the interaction strength between the microgel matrix and the MNP. With increasing interaction strength the response increases. For example loosely bound MNPs will rotate inside the gel matrix with small restrictions of their movement. For covalently bound MNPs every rotation of the MNP introduces a deformation to the matrix. The microgel matrix is, to the most extent, elastic and the deformation results in a counter torque.

## 2.3 Measurement Techniques

To determine the successful combination of microgels and magnetic nanoparticles several properties were measured. For example, the resulting magnetic microgel should still exhibit the VPT when raising the temperature above 32 °C. The surface charge of magnetic microgels should differ compared to the pure microgels and most important the MNPs should be inside the microgel. To verify all this and gain insight into additional properties several devices were used: transmission photometer, dynamic light scattering (DLS), Zetasizer, atomic force microscope (AFM), transmission electron microscope (TEM) and superconducting quantum interference device (SQUID). The above mentioned techniques and devices will be presented in the following sections.

### 2.3.1 Dynamic Light Scattering (DLS)

Dynamic light scattering (DLS) is used to determine the hydrodynamic size of dispersed particles or macromolecules by using the elastic scattering of light. The first description of DLS dates back to Leon Brillouin in 1914. The development stopped due to lack of high intensity monochromatic light sources. With the development of lasers and suitable detectors, the DLS concept improved and measurements could be realized. The scattering phenomena that are of most interest on the investigated length scale are the Mie and Rayleigh scattering. Rayleigh scattering occurs for particles or molecules that are much smaller than the used light wavelength. The light is scattered isotropically in all directions. Mie scattering occurs for particles that are of similar size as the wavelength of the light. The scattering intensity is highly dependent on the scattering angle. The light that is scattered by a colloidal particle interferes with light scattered by the next neighbor particle and so on. The resulting interference patterns consists of dark areas and bright spots called speckles. The size, position and intensity of the speckles is thereby correlated to the probed state, meaning the position and size of the individual colloidal particles inside the sample volume. A typical speckles image is simulated in *Figure 2.6*.

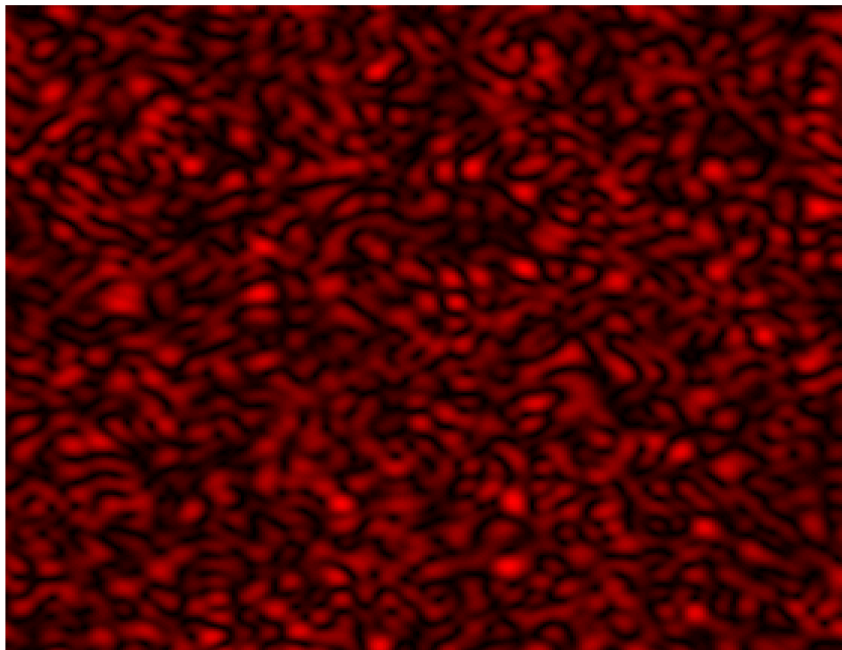


Figure 2.6: Simulated speckles created by the interference of scattered light from colloidal particles.

To measure the size of the colloidal particles, the light intensity of one speckle is measured against time. The speckle intensity changes with time due to Brownian motion of the colloidal particles. This particle motion is best described by a random walk model.

The intensity fluctuations of one speckle can be measured with an Avalanche photo diode. *Figure 2.7* shows such an intensity fluctuation. The graph sketches the intensity fluctuations for two cases, small particles and large particles. Small particles diffuse faster compared to larger particles, meaning smaller particles have a higher diffusion coefficient. The Stokes-Einstein equation (see *Equation 2.18*) relates the hydrodynamic radius ( $r_H$ ) and the diffusion coefficient ( $D$ ).

The diffusion coefficient is related to the auto correlation function of the scattered light. The field auto correlation  $g^1(\tau, \vec{q})$  is related to the particle distribution inside the dispersion, with  $\vec{q}$  being the scattering vector. The auto correlation function is given as:

$$g^1(\tau, \vec{q}) = \frac{\langle E(t, \vec{q})E(t + \tau, \vec{q}) \rangle}{\langle E(t, \vec{q}) \rangle^2}. \quad (2.23)$$

With  $E$  as the electric field of the scattered photon,  $t$  the measurement time and  $\tau$  the lag time (time between two measurements). Calculating the correlation values from the scattering events show a distinct behavior. At short lag times the correlation is high (for normalized correlation functions it is 1) due to the small distance the particles move during each measurements interval. For large lag times the correlation value decreases down to zero. If the movement of the particles can be fully described by Ficks second law, the auto correlation functions follows an exponential decay:

$$g^1(\tau, \vec{q}) = \int_0^\infty \exp(-\Gamma\tau). \quad (2.24)$$

$\Gamma$  is the decay rate. *Figure 2.7* shows a sketched exponential decay for small and large particles. The field auto correlation function is not accessible because it is based on the electric field of the photons. Instead the light intensity auto correlation function ( $g^2(\tau, \vec{q})$ ) is calculated. Both correlation functions are related by the Sigert equation:

$$g^2(\tau, \vec{q}) = 1 + \beta(g^1(\tau, \vec{q}))^2 \quad (2.25)$$

$\beta$  is a measure for the scattering geometry and is related to the number of observed speckles.

Colloidal particles in general are not monodisperse. Therefore, the simple exponential decay is not sufficient to describe the data points. To consider the particles polydispersity the exponential function is Taylor expanded. This is called Cumulant method proposed by Koppel [62]:

$$g^1(\tau, \vec{q}) = \exp\left(-\Gamma\left(\tau - \frac{\mu_2\tau^2}{2!} + \frac{\mu_3\tau^3}{3!}\right)\right) \quad (2.26)$$

$\mu_2$  and  $\mu_3$  are the moments of the second and third order. With the equations 2.26 and 2.25 the fitting function is constructed and is given as:

$$g^2(\tau, \vec{q}) = (Start - End) \exp\left(-2\Gamma\left(\tau - \frac{\mu_2\tau^2}{2!} + \frac{\mu_3\tau^3}{3!}\right)\right) + End \quad (2.27)$$

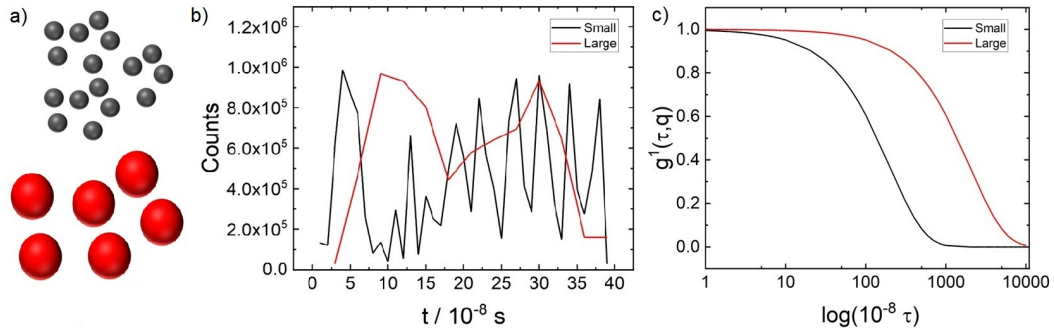


Figure 2.7: Sketch of the relation between particle size in a) for small particles (black) and large particles (red) and the light intensity fluctuation of speckles against time in b) and the calculated correlation function  $g^1(\tau, \vec{q})$  in c).

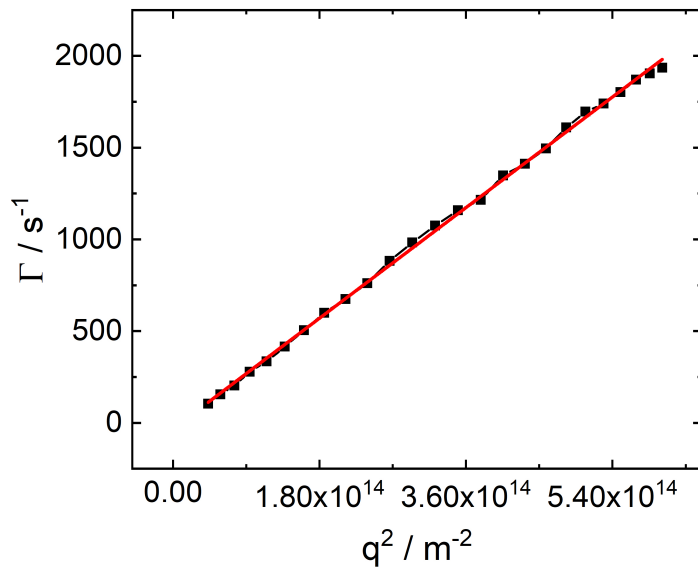


Figure 2.8:  $\Gamma$  is plotted against the scattering vector. The data were measured with standard particles of  $r_H = 100 \text{ nm}$  with the LS-Instruments DLS. The red line shows the linear regression. The error bars are not shown.

*Start* and *End* are the plateau values of the fits for small  $\tau$  and large  $\tau$ , respectively. The fitting equation *Equation 2.27* is more robust compared to *Equation 2.26*. After the data are fitted,  $\Gamma$  is plotted against  $q^2$ , where  $q$  is given by  $q = \frac{4\pi n_0}{\lambda} \sin\left(\frac{\theta}{2}\right)$ .  $n_0$  is the refractive index,  $\lambda$  is the laser wavelength and  $\theta$  is the scattering angle. The data  $\Gamma$  against  $q^2$  gives a linear relation that is connected via the diffusion coefficient  $\Gamma = Dq^2$ . *Figure 2.8* shows this linear behavior. From this, the hydrodynamic radius can be calculated. The hydrodynamic radius is defined as the radius a spherical particle would have with the same diffusion properties.

### 2.3.2 Electrophoretic Mobility/ Zeta Potential

The stability of colloidal particles is strongly related to their electrostatic interaction. This electrostatic interaction depends highly on the surface charge of such particles. The surface charge of the studied microgels originates in the network structure and the used monomers and their interaction with the environment (hydrophilic environment). The surface charges of the colloidal particles create a potential. This surface potential is not directly accessible through experimental setups. Instead, the zeta potential is measured. To understand the zeta potential, it is important to understand the particle surface, the adsorbed ions and water molecules. The ion distribution and the resulting potential are described with the Stern model. The Stern model is the combination of two opposing models used to describe the ions distribution and the resulting potential. The two outdated models were described by Helmholtz, which features a electrostatic double layer, and Gouy and Chapman, which features a diffusive ion layer.

To today's knowledge, the ion distribution and the potential can be described with the Stern model. The charged particles attract oppositely charged ions from the medium. The first layer is strongly bound to the particle surface and is called the Helmholtz layer. The Helmholtz layer and the surface charges of the particle is also called Stern layer. Inside the Stern layer the electrostatic potential decreases linearly. The strongly bound counter ions are not fixed in position and can be exchanged with other counter ions present in the solution.

The Stern layer is followed by a diffuse layer of mobile counter ions and ions. The counter ion concentration decreases from the concentration in the Stern layer down to the bulk concentration. The electrostatic potential decreases exponentially with a decay length  $\kappa^{-1}$  called the Debye length. The Debye length is given as:

$$\kappa^{-1} = \sqrt{\sum_i \frac{\epsilon_0 \epsilon k_B T}{\rho_{i,\infty} e^2 Z_i^2}} \quad (2.28)$$

$\epsilon_0$  is the vacuum permittivity,  $\epsilon$  the dispersant permittivity,  $\rho_{i,\infty}$  the number density of ion species  $i$ ,  $e$  the elementary charge and  $Z_i$  the valency of the ions. *Figure 2.9* shows the potential.

Inside the diffuse ion layer, the interaction strength between the ions and the charged particles decreases with increasing distance. At a certain distance, the ions are no

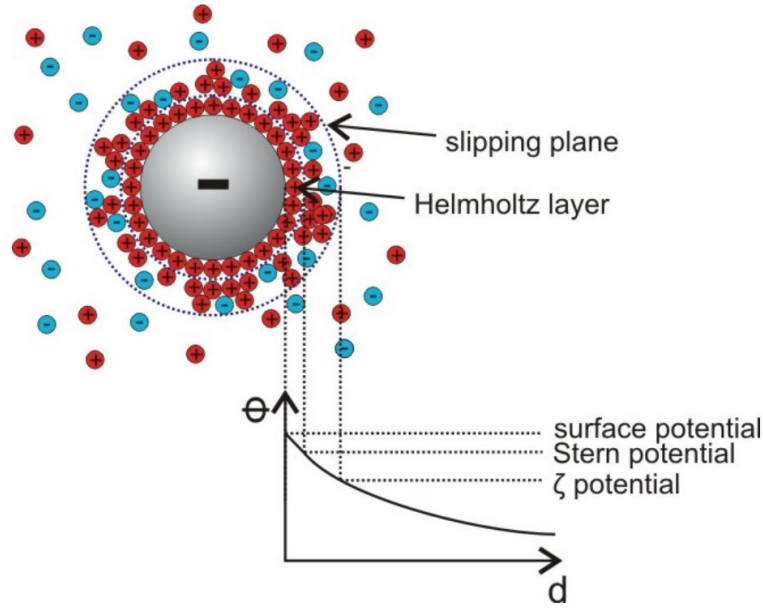


Figure 2.9: Schematic depiction of a negative charged particle with Stern layer and the diffusive layer of ions. Below is the electrostatic potential sketched. Reprinted from Sebastian Friedrich (née Backes) [22].

longer able to follow the movement of the particle. The layer at this distance is called the slipping plane. The potential at this plane is the so called zeta potential.

The zeta potential ( $\zeta$ ) is calculated from the electrophoretic mobility ( $\mu_E$ ) with the Henry equation:

$$\mu_E = \frac{v}{E} = \frac{2}{3} \frac{\epsilon \epsilon_0 \zeta f(ka)}{\eta}. \quad (2.29)$$

$f(ka)$  is the Henry parameter, which is 1 for unpolar solvents and small particles and  $\frac{3}{2}$  for polar solvents and large particles.  $v$  is the particle velocity and  $E$  the applied electrical field strength. The electrophoretic mobility is measured by laser Doppler electrophoresis. The sample is placed in an alternating electric field and is subjected to a laser. The scattered light is slightly shifted in frequency and it is detected in a heterodyne setup. The resulting intensity fluctuation frequency is related to the movement velocity of the particles.

The calculation of the zeta potential uses the Einstein-Smoluchowski equation for the relation between mobility and diffusion coefficient. This equation holds true for the assumption of spherical hard particles. For microgel particles the zeta potential can not be calculated due to the fluffy shell. Nevertheless, the measured electrophoretic mobility offers sufficient information about the electric charge of microgels. The electrophoretic mobility can also be used to compare different microgels and magnetic microgels.

The studied microgels have a typical diameter of less than  $1 \mu m$ . Optical microscopes

are not suitable for such small structures. Therefore, particle imaging was performed by either atomic force microscopy (AFM) or transmission electron microscopy (TEM).

### 2.3.3 Atomic Force Microscopy (AFM)

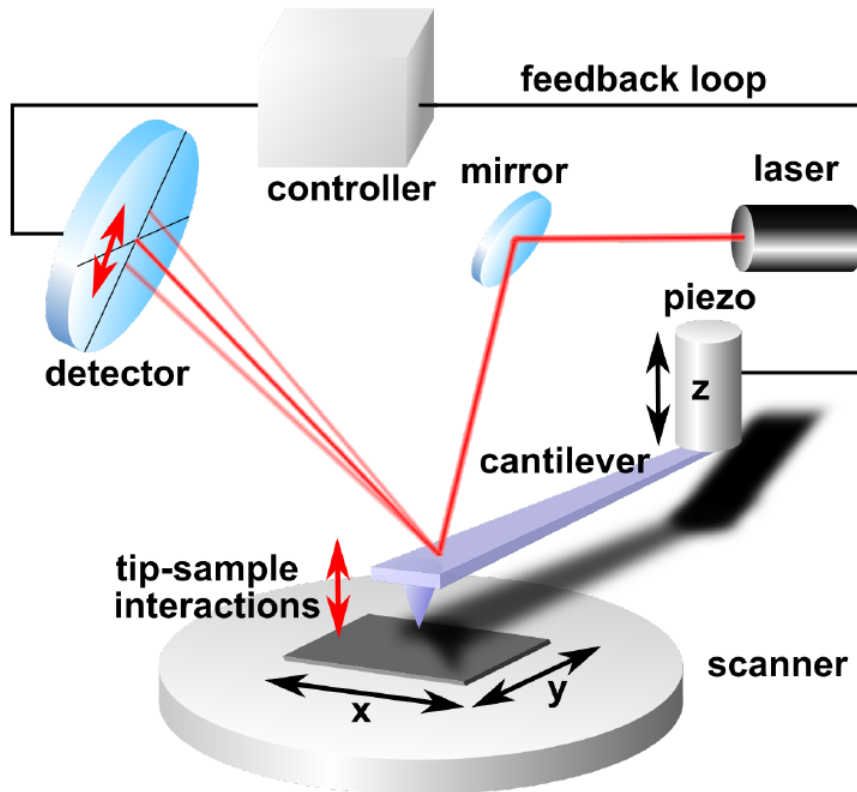


Figure 2.10: Sketch of an AFM setup, provided by Sebastian Schön.

Atomic force microscopy is a method of the scanning probe microscopy (SPM), invented from the scanning tunnelling microscope (STM). The STM had a resolution of several  $pm$  in normal and  $100 pm$  in lateral direction, thus an atomic resolution [37]. Common to all SPM methods is that the surface is scanned with a probe moving parallel to the surface. For the AFM, the deflection of a cantilever is monitored. *Figure 2.10* shows a simplified experimental setup of an AFM.

The measurement tip is located on the underside of the cantilever. The cantilever height is controlled by a piezo rack, which can extend and retract by applying a voltage. A laser beam is reflected off of the backside of the cantilever onto a 2D detector. Any deflection of the cantilever is encoded in the detector signal. The surface topography can be imaged in different ways, e.g. contact mode and tapping mode.

In the contact mode the tip of the cantilever is in contact with the surface. The surface is imaged by adjusting the height of the cantilever to achieve a constant deflection and

therefore, a constant force acting upon the cantilever. While this mode has a good lateral resolution it is also invasive. Materials such as soft microgels can be deformed easily.

The tapping mode is used to prevent such deformations of soft materials. In this mode the cantilever is excited to oscillate close to its resonance frequency. Upon approaching the surface the oscillation is damped. This damping originates from the interaction strength between surface and cantilever and their distance. The height of the cantilever is adjusted to achieve a constant damping. The target amplitude of the oscillation is kept at about 80 % of the free amplitude, which was set to 1 V. Due to oscillation above the sample surface the tip is never in contact with the sample and is thereby not invasive.

AFM in this study is used to image the surface coated with microgel particles. These microgels are measured at different temperatures around the VPTT. Additionally, the AFM can be used to measure the elastic moduli of the microgels at the surface. The cantilever is indented into the microgel and the deflection is proportional to the applied force and the elastic modulus of the microgel. With the spring constant of the cantilever and the Hertz model the elastic modulus can be calculated [43]. The Hertz model is given with

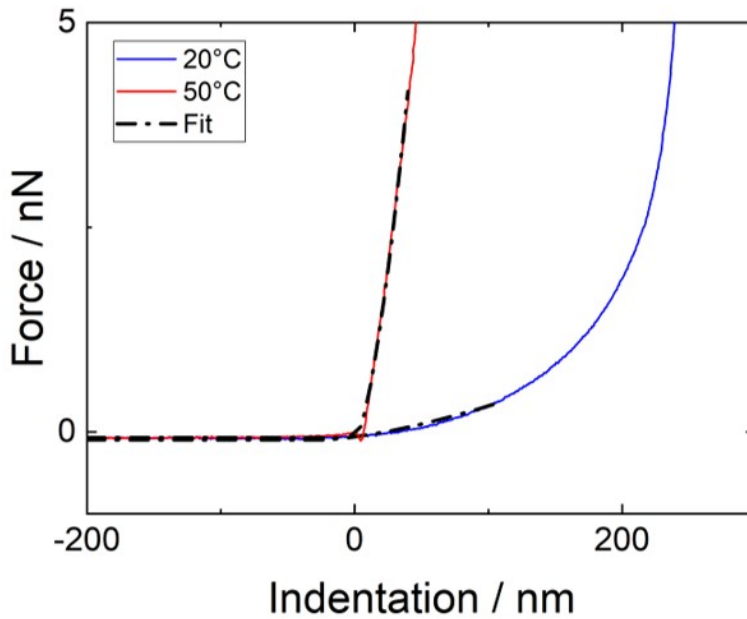


Figure 2.11: Two recorded force curves of a microgel at two temperatures. The blue curve shows a softer microgel (swollen state) while the red curves show a stiffer microgel (collapsed state). The black line is the applied Hertz model. The graph and the data are used with the permission of Matthias Kühnhammer.

$$F = \frac{4E\sqrt{R}}{3(1-\nu^2)}\delta^{3/2} \quad (2.30)$$

$\delta$  is the indentation depth,  $F$  is the applied force,  $E$  the elastic module,  $R$  is the radius

of the tip and  $\nu$  is the Poisson ratio. The Poisson ratio is the ratio of lateral and vertical strain. For microgel it is assumed to be 0.5 due to the high content of incompressible water.

*Figure 2.11* shows two force curves of one microgel at different temperature. For the softer gel (blue curve) the force increases slower with increasing indentation. Shown in black is the fitted Hertz model and only the first 10 % of the indentation were used to calculate the elastic modulus. *Figure 2.11* shows also that the collapsed microgel is stiffer compared to the swollen microgel. With this the elastic modulus of the microgels can be linked to the amount and distribution of cross-linker.

### 2.3.4 Transmission Electron Microscopy (TEM)

The diameter of the MNPs is about 15 nm, thus too small for measurements using a normal light microscope. One technique to image the samples is transmission electron microscopy. In a high vacuum a hot cathode produces thermal electrons. These electrons are accelerated to an energy of 200 keV. They are aligned and filtered before passing through the sample. After the sample, the electrons are focused on either a fluorescent screen or a camera. By changing the lenses, the magnification can be changed and also the electron beam can be aligned. The electron beam is highly sensitive to the electron density and the sensitivity is observed as different contrast for different materials. This leads to some problems for imaging organic structures such as the microgels as they give almost no contrast in vacuum. Metallic nanoparticles in the vicinity of or within the microgels can be used as reference points for the contrast. Thereby the microgels structure may become visible. As the electrons free path length highly depends on the density of the surrounding medium, the vacuum in the three chambers (gun chamber, sample chamber, camera chamber) is further increased with a cold trap.

### 2.3.5 UV/VIS Absorption

The UV/Vis spectrometer is used to measure the light absorption of a sample. The sample is exposed to light of different wavelengths and the transmitted light is detected. The transmittance is defined as  $\tau = \frac{I}{I_0}$ , where  $I$  is the light intensity after passing the sample and  $I_0$  the light intensity of the undisturbed beam. The loss of light intensity is related to the path length of the light ( $d$ ) in the sample and the sample concentration ( $c$ ), thus giving the Lambert-Beer law:

$$E_\lambda = \epsilon_\lambda cd = \log \frac{I_0}{I} \quad (2.31)$$

with  $\epsilon_\lambda$  as the molar extinction coefficient that depends on the light frequency.

## 3 Experimental Section

The following chapter describes the performed experiments and measurement parameters. The chapter consists of the used chemicals, the sample preparation and the used devices for the measurements, as well as the measurement routines.

### 3.1 Chemicals

The following chemicals were used to prepare the microgels (MGs) and magnetic microgels (MMGs). The chemicals were purchased from Sigma Aldrich and used as delivered with no further purification: *N*-Isopropylacrylamide (NIPAM, 97%), *N,N'*-Methylenbisacryl-

amide (BIS), allylamine (AA,  $\geq 99.5\%$ ) and allyl mercaptan (AM). The polymerization initiator 2,2'-Azobis(2-methylpropionamide) dihydrochloride (AAPH) was purchased from two companies once from Sigma Aldrich during research time in Berlin and from Caymen Chemicals in Darmstadt. Further, the following chemicals were used to clean measurement cells or disperse the samples: Ethanol ( $\geq 99.5\%$ , anhydrous, non-denatured), isopropanol ( $\geq 99.5\%$ ), acetone ( $\geq 99.5\%$ ), hydrogen chloride (37%), sodium bicarbonate.

The used water was purified with a Millipore milli-Q purification system (from Merck) with a final electrical resistance for the water of 18.5 M $\Omega$ .

### 3.2 Samples

#### 3.2.1 Microgel Synthesis

The microgels were polymerized from *N*-Isopropylacrylamide by surfactant free radical precipitation polymerization using the described synthesis procedure by Pelton et al. [93, 96]. *N,N'*-Methylenbisacrylamid was used as cross-linker. Additionally, two co-monomers were used for different purposes. Allylamine was built-in to increase the positive charges in the microgels. The positive charge of the microgels was desired to attract the negatively charged MNPs, and therefore improve the diffusion into the MGs. Allylmercaptan (AM) was built into the microgels to increase the attraction between the microgel and gold (gold wafer). Additionally the AM introduces a hydrophobic moiety to the microgel network. In the case of co-polymerization with AM, the co-monomer was added only in the last minute of the synthesis. 1 ml of a AM solution ( $c = 0.1$  mol/l) was added. *Figure 3.1* shows the structure of the used monomers, cross-linker, co-monomers and polymerization initiator.

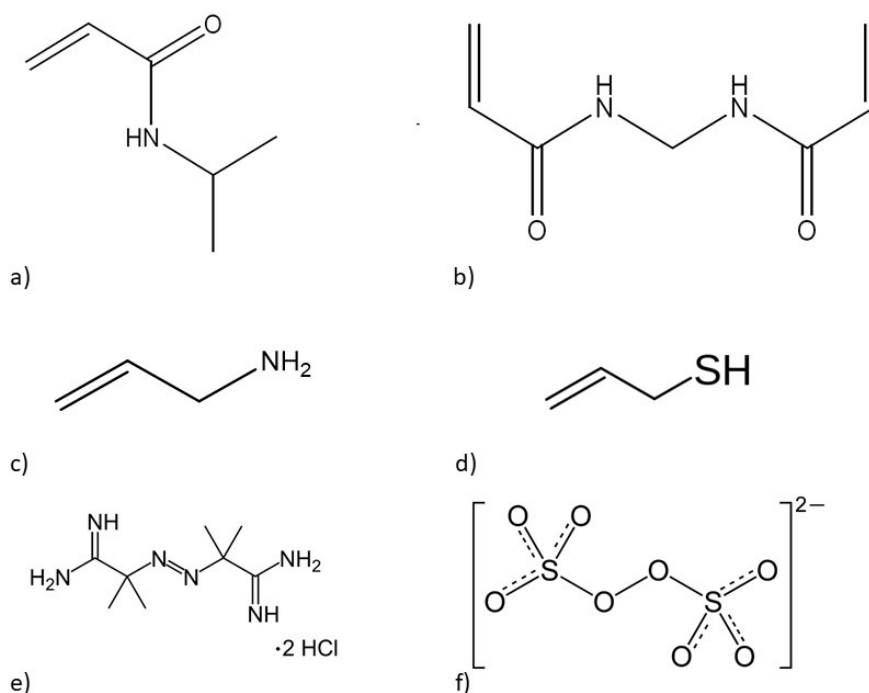


Figure 3.1: a) NIPAM monomer, b) BIS cross-linker, c) allylamin co-monomer, d) allylmercaptan co-monomer, e) AAPH positive polymerization initiator, f) KPS negative polymerization initiator

Three synthesis routes were used to polymerize the microgels presented in this work. The batch method is well known from literature and produces microgels with a higher cross-linker concentration in the center of the microgels (core/shell structure, heterogeneous structure) [89]. The feeding method was also described in literature [56, 81, 117] and leads to a constant cross-linker distribution (homogeneous structure). The last method is the semi-batch method, which is a combination of both methods [89]. The semi-batch method is in literature proposed to produce homogeneously cross-linked microgels. The three synthesis are designed to have an equal amount of monomer available for the reaction.

#### *Batch Method*

For the batch method, 20 mmol of the reactants were dissolved in 20 ml of milliQ water. The solution was transferred into the reactor. The beaker was washed several times with small amounts of milliQ water ( $\approx 10$  ml). The washing water was added to the reactor. The reactor was filled with milliQ water to a total reaction volume of 120 ml to 150 ml depending on the sample. Water as the reaction solvent does not take part in the reaction and is of minor influence to the reaction kinetics. The reaction volume was

stirred at 1000 rpm and degassed with nitrogen for one hour. The reactor was heated to 80 °C via a water jacket. The polymerization was started by adding 1 ml of initiator solution (the amount of starter is shown in *Tab. 3.1*). The reaction was stopped by rapid cooling after 90 min (bMG1-6) and after 10 min (bMG7-8). The formed microgel suspension was dialysed against milliQ water. The dialysis was carried out for a minimum of 7 days. After the dialysis, the microgel was freeze-dried at  $-84^{\circ}\text{C}$  for 72 hours. The dried microgels were stored in the freezer at  $-22^{\circ}\text{C}$ .

#### *Feeding Method*

For the feeding method 30 mmol of the reactants were dissolved in 30 ml of milliQ water. 100 ml to 130 ml milliQ water was placed in the reactor. The water in the reactor and the reactant solution were degassed separately for one hour with nitrogen under constant stirring. The reaction volume was stirred with 1000 rpm during the polymerization. The polymerization initiator was added to the reactor. 20 mmol of the reactants were fed into the reactor using a syringe pump. The feeding pump created a constant flow of reactants into the reactor. The flow rate was adjusted between 1 ml/min and 4 ml/min, for most of the used microgels 2 ml/min was used. The feeding and the polymerization were stopped simultaneously. The feeding/reaction time was chosen, so the amount of available monomer is equal to the amount of monomer used in the batch method. The microgels were cleaned by dialysis against milliQ water. The dialysis was performed for 7 days. After the dialysis, the microgels were freeze-dried at  $-84^{\circ}\text{C}$  for 72 hours. The dried microgels were kept in the freezer at  $-22^{\circ}\text{C}$ .

#### *Semi-Batch Method*

The combination of both presented methods is called the semi-batch method. In this combination, roughly 10% of the monomer solution is placed in the reactor. In total 20 mmol of reactants were used for the synthesis. Similar to the feeding method 100 ml to 130 ml milliQ water was added. The reactant were degassed for one hour with nitrogen. The remaining 90% of the monomer solution was also degassed and transferred into a syringe. The polymerization was started by adding the polymerization initiator. After a short time ( $\approx 30$  s to 60 s) the remaining monomer solution is fed into the reaction mixture. The reaction was terminated by rapid cooling. Similar to the other two microgel synthesis methods, the microgels were dialysed and freeze-dried.

The microgel samples were prepared by dispersing the dried microgels in water at  $\beta = 0.5$  wt% and slightly shaken for one day to re-swell the microgels.

*Table 3.1* shows an overview of the synthesized microgels. The microgel samples are labeled according to the following pattern: xMGy, where x refers to the synthesis method of feeding (fMG), batch (bMG), semi-batch (sbMG) and y is a numbering index starting from 1 for each method.

Sample	Initiator	$n_{total}/\text{mmol}$	$c(BIS)/\text{mol}\%$	$c(AA)/\text{mol}\%$	$c(AM)/\text{mol}\%$	$t/\text{min}$	Used in
bMG1	APS (0.10 mmol)	10	5	0	0	90	Chapter 6
bMG2	APS (0.10 mmol)	10	5	5	0	90	Chapter 6
bMG3	APS (0.40 mmol)	10	5	5	0	90	Chapter 6
bMG4	AAPH (0.15 mmol)	10	7.5	2.5	0	90	Chapter 6
bMG5	AAPH (0.12 mmol)	5	0.5	0	0	90	Chapter 7
bMG6	AAPH (0.12 mmol)	5	5	0	0	90	Chapter 7
bMG7	AAPH (0.10 mmol)	20	2	0	0	10	Chapter 7
fMG1	AAPH (0.10 mmol)	20	2	0	0	5	Chapter 7
fMG2	AAPH (0.10 mmol)	20	2	0	0	10	Chapter 7
fMG3	AAPH (0.10 mmol)	20	2	0	0	20	Chapter 7
sbMG1	AAPH (0.10 mmol)	20	2	0	0	10	Chapter 7
bMG8	AAPH (0.24 mmol)	20	2.5	2.5	0	10	Chapter 8
fMG4	AAPH (0.24 mmol)	20	2.5	2.5	0	10	Chapter 8
fMG5	AAPH (0.24 mmol)	20	3	3	0	10	Chapter 9
fMG6	AAPH (0.24 mmol)	20	3	3	0.4	10	Chapter 9

Table 3.1: Overview of the synthesized microgels used in this thesis. The sample name consists of the synthesis method (b = batch, f = feeding, sb = semi-batch) and an index. The parameter  $t$  is the reaction time and feeding time.

### 3.2.2 Magnetic Nanoparticles

The magnetic nanoparticles consisted of  $CoFe_2O_4$  and were synthesized by the group of Dr. Birgit Hankiewicz (née Fischer) in Hamburg or Prof. Dr. Annette M. Schmidt in Cologne. The description of the MNP synthesis can be found in literature [80, 81, 101]. While all the used MNP had the same core material, they differ in their stabilization coating and size. *Table 3.2* lists the used MNPs.

Sample	Origin	Core	Coating	$r$ / nm	$c$ / $\frac{mg}{ml}$	$\zeta$ / mV
MNP1	Cologne	$CoFe_2O_4$	PAA	15	1.	-70
MNP HHCA	Hamburg	$CoFe_2O_4$	CA	15	5.8	-56.9

Table 3.2: Characteristics of magnetic nanoparticles with core radius, hydrodynamic radius, concentration and zeta potential. PAA denotes Poly(acrylic acid) and CA is citric acid.

### 3.2.3 Magnetic Microgels

The microgels were loaded with the MNPs to form magnetic microgels. The microgels were dispersed in water and shaken for a minimum of 24 h before usage. The concentration of the microgel dispersion was chosen to be 0.5 wt% and a pH of 7 was measured (no further additives were used). The pH of 7 is a compromise between the stability of the MNPs and the charge density of the microgels.

Before usage, both dispersions (microgel and MNP) were placed in a ultrasonic bath for 10 min. For the MMGs, 50  $\mu$ l microgel dispersion was mixed with water ( $\approx$  950  $\mu$ l). The MNPs were added. A total sample volume of 1 ml was prepared. For larger volumes, several samples were produced at the same time in smaller sample sizes and combined after the last centrifugal step. The weight concentration of microgels and MNPs was set to be the same. After mixing, the samples were vortexed for 30 min with 1000 rpm up to 1500 rpm. To remove free and unbound MNPs, the samples were centrifuged at 1000 rpm (67 g) for 30 min. The supernatant contained the unbound MNPs and the precipitant the MMGs. The supernatant (800  $\mu$ l) was replaced with water. The cleaning process of vortexing and centrifuging the sample was repeated three times until the supernatant was clear. The measured pH was 7 for the MMG dispersion.

Also a different approach to create MMGs was tested. Here the MNP were already present in the reaction volume during the polymerization. This approach did not produce any usable MMGs so far and will be discussed in the appendix in more detail.

## 3.3 Experimental Methods

The microgels, MNPs and MMGs were characterized with various techniques such as dynamic light scattering (DLS), electrophoretic mobility (EM)/zeta potential, UV/VIS spectroscopy, transmission electron microscopy (TEM) and atomic force microscopy

(AFM). The following sections describe the used devices, measurement parameters and the sample preparation.

### 3.3.1 Dynamic Light Scattering (DLS)

Dynamic light scattering was used to determine the hydrodynamic radius of the microgels and magnetic microgels. The DLS setup was a multi angle setup from LS-Instruments. The measurements were performed with a solid state laser with  $\lambda = 660$  nm and a maximum energy output of 100 mW (Cobalt Flamenco 100).

The scattered light was coupled into a optical fiber to be detected with two avalanche photo diodes. The scattered light was analyzed with a pseudo cross correlation. The auto correlation is described in *Chapter 2.3.1*. In contrast to the described auto correlation function, the pseudo cross correlation calculates the correlation from two detectors. Both detectors measure the same speckle, hence the name pseudo cross correlation. This pseudo cross correlation was performed by the LS-Instruments hardware correlator. To calculate the hydrodynamic radius from the scattered light, the sample was measured at several angles. The samples were measured at angles between  $30^\circ$  and  $120^\circ$  in steps of  $5^\circ$  or  $10^\circ$ . The measurement time was set to 30 sec for each angle.

The measured samples were diluted until they appear clear and colorless and had no visual opalescence. The concentration was about 0.005 wt%. The dilution is a requirement to measure single scattering events and furthermore to measure the undisturbed Brownian motion of the particles. The dilution water for the sample was filtered with a 250 nm pore syringe filter. The cuvettes for the DLS measurements were cleaned with an acetone fountain before usage.

Dust particles or big agglomerates passing through the laser beam, disturbing the measurements, were excluded from the analysis. Some dust particles accumulate over time in the sample bath. Such a disturbance is exemplary shown in *Figure 3.2* in blue.

The correlation data were fitted with a Taylor expanded exponential decay given in *Equation 2.23*. The  $\Gamma$  was plotted against the scattering vector squared  $q^2$ . This plot is fitted with a linear regression and the slope corresponds to the diffusion coefficient related to the hydrodynamic radius via *Equation 2.18*. The error of the hydrodynamic radius was calculated from the fitting error for the diffusion coefficient and the Gaussian propagation of uncertainty.

The temperature inside the sample chamber was controlled via a thermostat with an accuracy between 0.5 K and 0.1 K. To measure the shrinking and swelling behavior, the samples were measured between  $15^\circ\text{C}$  to  $50^\circ\text{C}$ . The performed temperature dependent measurements were scripted and, for temperature steps smaller than 2 K, the sample was equilibrated for 5 min. For larger temperature steps, the samples were equilibrated for 10 min. The data were analyzed with a self written Mathematica script. The resulting hydrodynamic radii in dependence of the temperature can then be plotted. The temperature with the highest slope of the size change is the VPTT. In this study the VPTT was derived from a fit with a simple exponential decay.

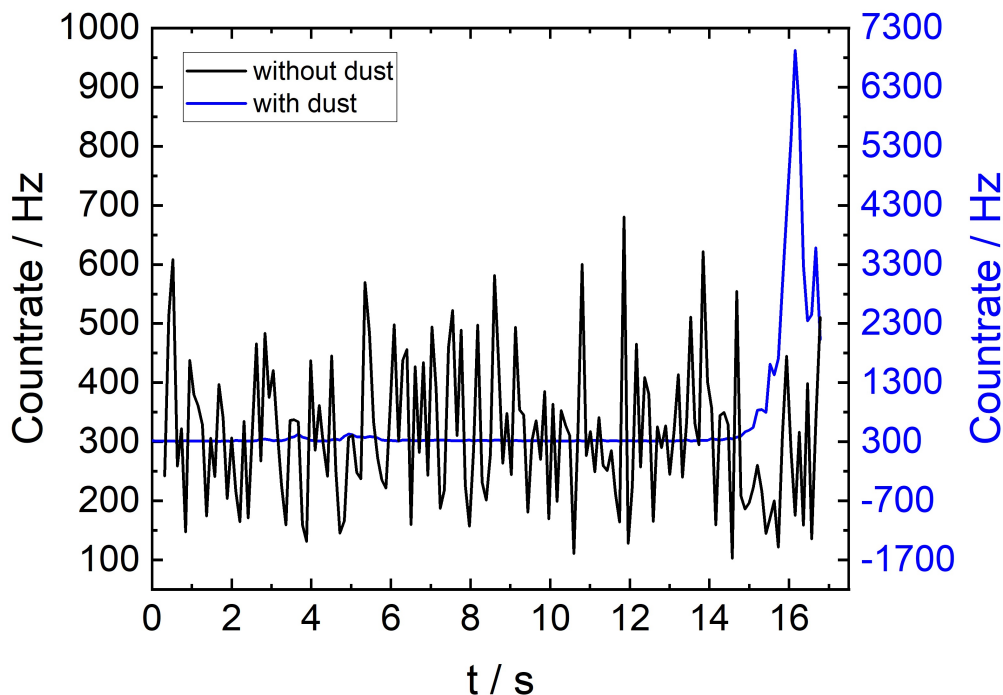


Figure 3.2: Exemplary graphical data of the scattering intensity measured by DLS for two samples. In black, the expected scattering signal is shown and appears to be random. In blue the expected scattering signal is overlaid by a scattering signal from dust (the large peak at around 16 s).

### 3.3.2 Electrophoretic Mobility/Zeta Potential

The electrophoretic mobility and the zeta potential measurements were carried out with a Malvern Zetasizer Nano ZS. The laser had a wavelength of  $\lambda = 633$  nm with a power of  $p = 4$  mW. The scattered light was measured under an angle of  $\theta = 173^\circ$ . The samples were diluted similar to the DLS samples. The samples were measured 7 times and the average and standard deviation were calculated. The measurements were carried out at various temperatures ranging from 15 °C to 50 °C.

### 3.3.3 Transmission Electron Microscopy (TEM)

The TEM images were done with one of the two devices: from 2014 to 2017 with a Cryogen TEM JEOL JEM2100 (TU Berlin) and the EM21010 sample holder. From 2017 till 2021 with FEI CM20 microscope and a Gatan double tilt sample holder (TU Darmstadt). In both cases, the measurements were performed with an acceleration voltage of 200 kV. The samples were prepared on a 300 or 200 mesh copper grid covered with a carbon film (Sience Service, Munich, Germany). The grids were charge neutralized in a plasma glow discharge chamber. 5  $\mu$ l of the sample (0.05 wt%) was placed on the grid. After 1 min, the excess dispersion was removed with filter paper to prevent any

further particle precipitation. The samples were dried under ambient conditions in a box with air circulation over night before being imaged.

### 3.3.4 Atomic Force Microscopy (AFM)

The samples were prepared on a gold wafer. Gold wafers have shown the highest number of microgels adsorbed on the surface, due to mirror charges. Furthermore, the microgels were not as easy to be washed off compared to other surfaces. The gold wafer was cleaned with ethanol in a ultrasonic bath for 5 minutes. The microgel dispersion were spin coated (1000 rpm for 30 s) onto a cleaned gold wafer. The samples were imaged with a JPK NanoWizard II or with an MFP-3D (Asylum Research, Oxford Instruments). For measurements in ambient conditions, AC 160 cantilevers from Olympus were used. For measurements in liquid, HQ:NSC18/CR-AU BS cantilevers from Micromash were used. Measurements of the elastic modulus were performed with the MFP-3D and HQ:CSC38/NO AL cantilevers from Micromash. The tip angle is  $40^\circ$  with an average spring constant of  $0.05 \text{ N/m}$ . The elasticity was measured in a water drop and the approach curves were fitted by the Hertz model. For the fitting the first 10 % of the approach curve was used. The elastic moduli were averaged for several particles.

### 3.3.5 UV/Vis Spectroscopy

The UV/Vis spectrometer was used to measure the absorption of light by the microgels, MMGs and the MNPs to determine a relative change in concentration. The change in concentration was observed for the samples in an external magnetic field and without. The measurements were carried out with a Cary 50 spectrometer and a Perkin Elmar Lambda 650 spectrometer. The external magnetic field was generated by a neodymium magnet ( $Nd_2Fe_{12}B$ ) placed next to the sample.

### 3.3.6 Mass Spectrometry

The mass spectrometry (MS) measurements were performed on a LTW Orbitrap XL with an ionization by atmospheric pressure chemical ionization. The samples were directly injected into the ionization chamber without a chromatographic column. The measurements were performed by Dr. Maria Schlangen (technical staff from the analytic service of the TU Berlin). Beforehand the samples were filtered with a centrifugal filter to remove microgel particles.

### 3.3.7 Superconducting Quantum Interference Device (SQUID)

The magnetization and the AC-susceptibility measurements were performed with a Quantum Design MPMS-5S SQUID magnetometer with an integrated AC option. About 50  $\mu\text{l}$  of the MMG dispersion were placed into a PCR tube, the lid was then melted to provide a gas-tight holding for the MMG sample material. This is required due to the helium underpressure atmosphere in the SQUID sample chamber. Individual samples of the same batch were used for magnetometry and AC-susceptibility to circumvent aging

effects or permanent changes inflicted during one measurement protocol. For temperature dependent magnetization measurements the standard zero-field-cooled/ field-cooled (ZFC-FC) protocol was employed, using a magnetic field of 10 mT and heating/cooling rates of 2 K/min. The sample is cooled down without an external field. The ZFC curve is recorded with a magnetic field and the sample is heated. After the heating the sample is cooled down again with the magnetic field still present (FC curve). AC-susceptibility measurements were performed upon rising temperature in settle mode with temperature steps  $\Delta T$  of 0.5 – 5 K at frequencies between 0.1 Hz and 1500 Hz, using 8 equidistant frequency steps per order of magnitude and an AC-field amplitude of 0.1 mT. The SQUID measurements were performed by Joachim Landers in the group of Prof. Dr. Wende at the University Duisburg-Essen.

## 4 Loading of PNIPAM Based Microgels with $CoFe_2O_4$ Nanoparticles and their Magnetic Response in Bulk and at Surfaces

This study was performed in collaboration with Sebastian Friedrich (né Backes). The AFM measurements and analysis were performed by Sebastian Friedrich. Two microgels (bMG1 and bMG2) were synthesized by Lucas Kuhrts as part of the work of Sarah Aleed. The magnetic nanoparticle were synthesized by Eric Roeben. This study has been published in "Loading of PNIPAM Based Microgels with  $CoFe_2O_4$  Nanoparticles and their Magnetic Response in Bulk and at Surfaces", Sebastian Backes, Marcus U. Witt, Eric Roeben, Lucas Kuhrts, Sarah Aleed, Annette M. Schmidt, Regine von Klitzing, *J. Phys. Chem. B*(2015), 119, 12129-12137, DOI: 10.1021/asc.jp cb.sb03778

### 4.1 Abstract

The present chapter addresses the loading of thermoresponsive poly-*N*-isopropylacrylamide (PNIPAM) based microgel particles with magnetic nanoparticles (MNP:  $CoFe_2O_4@PAA$  (PAA: polyacrylic acid)) and their response to an external magnetic field. The MNP uptake is analyzed by transmission electron microscopy (TEM). Obviously, the charge combination of MNPs and microgels plays an important role for the MNP uptake, but it does not explain the whole uptake process. The MNP uptake results in changes of size and electrophoretic mobility, which is investigated by dynamic light scattering (DLS) and Zetasizer. The microgels loaded with MNPs preserve their thermosensitivity and they show magnetic separability and are considered as magnetic microgels. After adsorption at a surface the magnetic microgels are studied with a scanning force microscope and indentation experiments. The magnetic microgels show an elongation along the magnetic field parallel to the surface while the height of the microgels (perpendicular to the surface and to the magnetic field) is compressed. This result is in good agreement with simulations of volume change of ferrogels in a magnetic field.

## 4.2 Introduction

Polymeric ferrogels consist of magnetic nanoparticles (MNPs), which are embedded in a cross-linked polymeric hydrogel [82].

The here presented polymeric ferrogels are ferromagnetic and the ferrofluids used for their preparation are superparamagnetic. If there is a coupling between MNP and gel, the magnetic torque which is exerted on the MNPs is balanced by an elastic counter-torque caused by the deformation of the gel [64]. This means that the magnetisation of the hybrids reflects the elastic properties of the gel. It has been shown that the Young's modulus of macroscopic ferrogels increases in the presence of an external magnetic field [65,70]. Other factors influencing the magnetic response are the concentration of MNPs, their distribution in the gel, and their magnetic properties.

Several theoretical studies have dealt with the deformation of ferrogels in a magnetic field. Most ferrogels elongate in field direction, but depending on their shape and on the concentration of MNPs also a contraction is possible for low concentrations and prolate or strongly oblate shapes [17]. The coupling of MNPs to the matrix also plays a role, with weak couplings leading to a stretching in field direction and an overall anisotropic volume loss, whereas strongly coupled hybrids show an isotropic volume loss [99].

The resulting magnetic microgels could be magnetically separated. Another approach is the incorporation of MNPs into the meshes of a polymer network [15,102]. Here, magnetite nanoparticles have been deposited into/onto microgels consisting of copolymers of acetoacetoxyethyl methacrylate and N-vinylcaprolactam P(AAEM-co-VCL). A considerable temperature and pH dependence was preserved for these hybrids.

So far, the magnetic microgels were mainly investigated according to their magnetic separability and their magnetisation. In case of thermoresponsive microgels (e.g. PNIPAM, P(AAEM-co-VCL)) it was tested if their thermosensitivity is still preserved after loading with MNPs. So far, the microgel composition have not been tuned in order to increase the amount of MNPs. Furthermore, nothing is known about the change in microgel shape in an external field, especially under geometrical confinement, e.g. after adsorption at a surface. The present study on PNIPAM based microgels addresses these problems.

Embedding a large number of  $CoFe_2O_4@PAA$  MNPs into a PNIPAM microgel network is aimed. In order to increase the amount of MNPs the microgel matrix is tailored with a comonomer and different polymerization starters. The loading of the obtained magnetic microgels is characterized by TEM. Additionally, the hydrodynamic radii (by DLS), the electrophoretic mobility (by Zetasizer), as well as the magnetic separability (by UV-Vis absorption spectroscopy) are analyzed. Furthermore, the magnetic deformation of the magnetic microgels under geometric confinement at surfaces and the influence of the MNP loading on elastic properties of the microgels are investigated by means of atomic force microscopy (AFM).

To study the loading capacity of the microgels with MNPs the following microgels in *Table 4.1* were prepared.

Gel	c(BIS)[mol%]	AA[mol%]	Initiator	n(Initiator)[ $\mu\text{mol}$ ]
<i>bMG1</i>	5	0	APS	100
<i>bMG2</i>	5	5	APS	100
<i>bMG3</i>	5	5	APS	400
<i>bMG4</i>	7.5	2.5	AAPH	150

Table 4.1: The concentration in mol% is calculated for the total amount of used polymerization reactant.

## 4.3 Results

### 4.3.1 Pre-experiment: Effect of sign of microgel charge on MNP loading

In order to check the effect of sign of microgel charge on MNP loading the negatively charged reference system *bMG1* without any cationic comonomer AA and the same microgel but with 5 mol% AA were compared. *bMG1* has an EM of  $-0.45 \mu\text{mcmV}^{-1}\text{s}^{-1}$  and *bMG2*  $0.91 \mu\text{mcmV}^{-1}\text{s}^{-1}$ . TEM images of the samples, as shown in *Figure 4.1* show that the uptake was much more successful for the cationic P(NIPAm-co-allylamine) microgel *bMG2*. Sample *bMG1* shows MNPs for the most part only on the outside of the microgel.

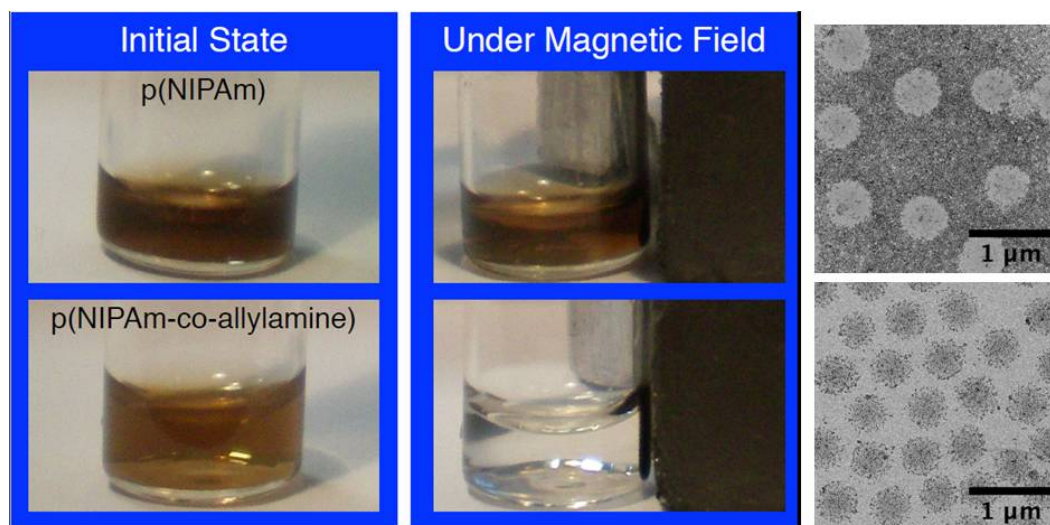


Figure 4.1: Upper row: PNIPAM microgels (sample *bMG1*) with MNP before and during application of a magnetic field and the respective TEM image; Bottom row: P(NIPAm-co-allylamine) with MNP before and during application of a magnetic field and the respective TEM image. This pre-experiment was performed by S. Aleed.

The separation properties of the magnetic microgels were tested with a permanent magnet. *Figure 4.1* shows the two magnetic microgel hybrids before and during appli-

cation of the gradient magnetic field. The PNIPAM microgel bMG1 shows that some degree of separation is achieved; however, the bulk solution still contains a high degree of MNPs. On the other hand, the P(NIPAm-co-allylamine) hybrids show a full separation of solution and hybrid nanoparticles after a couple of minutes in the presence of the magnetic field. This also suggests that more MNPs are located in or at the surface of the microgels, comparatively, allowing a stronger magnetic response. Due to the lack of embedded MNPs the reference system (bMG1) has not been considered for further investigations.

### 4.3.2 Hydrodynamic radius

The hydrodynamic radius was measured with DLS for the microgels (MGs) and the magnetic microgel (MMGs) at 20 °C. *Table 4.2* shows the hydrodynamic radii of the samples.

Microgel	$r_H(25^\circ\text{C})[\text{nm}]$	Ferrogel(magnetic microgel)	$r_H(25^\circ\text{C})[\text{nm}]$
<i>bMG1</i>	$249 \pm 10$	–	–
<i>bMG2</i>	$204 \pm 9$	<i>bMMG2</i>	$523 \pm 40$
<i>bMG3</i>	$240 \pm 6$	<i>bMMG3</i>	$527 \pm 15$
<i>bMG4</i>	$348 \pm 16$	<i>bMMG4</i>	$508 \pm 32$

Table 4.2: Increasing hydrodynamic radii of the gel particles after loading with MNP.

Loading of the microgel particles with MNPs leads to an increase in the hydrodynamic radius.

### 4.3.3 Electrophoretic Mobility

As a second characteristic measure of the microgels the electrophoretic mobility (EM) was measured. The EM changes with swelling and shrinking of the gels. Therefore, the EM of the microgels were measured as a function of temperature. *Figure 4.2 a)* and *Figure 4.2 b)* shows the EM before and after loading with MNPs, respectively.

The pure gels (bMG2, bMG3) show an increasing EM below and a decreasing EM above the VPTT, bMG4 shows an overall increase of the positive EM. At room temperature the loading of the positively charged microgel with negatively charged MNPs changes the EM from positive to negative values for all samples. *Tab. 4.3* shows the change of EM for 20 °C. For the negatively charged magnetic microgels (bMMG2, bMMG3, bMMG4) the EM becomes more negative with increasing temperature. For all magnetic microgels the volume phase transition at about 32 °C is still detectable.

### 4.3.4 Loading of microgels with MNP (TEM)

The amount of adsorbed MNPs and the distribution in the gels was investigated by TEM. *Figure 4.3* shows an exemplary TEM image of bMMG3. Small MNPs in the range of 15 nm and larger microgel particles with a broader density profile can be seen.

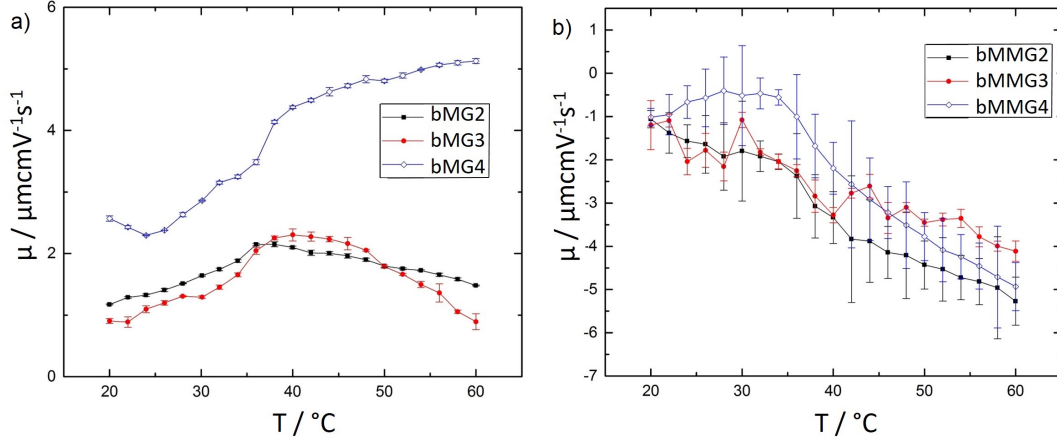


Figure 4.2: Graph a) is the electrophoretic mobility of the microgels and b) of the magnetic microgels in dependence of temperature.

Gel	$\mu / \mu\text{mcmV}^{-1}\text{s}^{-1}$	Ferrogel	$\mu \mu\text{mcmV}^{-1}\text{s}^{-1}$	$\Delta\mu / \mu\text{mcmV}^{-1}\text{s}^{-1}$	loading
<i>bMG1</i>	-0.45	-	-	-	-
<i>bMG2</i>	+1.17	bMMG2	-1.06	-2.23	$133 \pm 16$
<i>bMG3</i>	+0.91	bMMG3	-1.20	-2.11	$275 \pm 36$
<i>bMG4</i>	+2.57	bMMG4	-1.02	-3.59	$243 \pm 29$

Table 4.3: Electrophoretic mobility  $\mu$  at 20  $^{\circ}\text{C}$  and loading with MNPs for the MMGs (average number of NMPs per microgel particle).

Obviously, the microgel particles consist of a dense core and a rather fluffy shell, where most of the MNPs adsorb. The second information that can be obtained from the TEM image is the spacing between the MNPs. It shows that the MNPs are well separated and homogeneously distributed over the gel profile. A tendency for a hexagonal packing of the magnetic microgel particles is observed. Almost no single MNP exist between the magnetic microgels.

From the TEM images the loading with MNPs can be determined. *Table 4.3* shows the number of MNPs loaded into the microgels. Obviously, no systematic relation between EM and loading exists.

#### 4.3.5 Magnetic separability (Absorption measurement)

A first experiment to investigate the magnetic properties of the magnetic microgel is to pull them through the solution in an external magnetic field. Therefore, absorption measurements with a UV-Vis spectrometer were performed. The samples were measured under an external magnetic field. *Figure 4.4* shows a decreasing absorbance against the measuring time.

bMMG3 shows the fastest separation of the MMGs from dispersion and bMMG2 the

slowest. The absorbance of bMMG4 decreases down to 40 % of its starting value. For the samples bMMG2 and bMMG3 the absorbance decreases only to 60 %.

#### 4.3.6 Adsorbed microgels: Microgels under geometrical confinement

Since bMG3 (bMMG3) shows the highest loading with MNPs this MMG was used for further investigation at the surface. *Figure 4.5* shows a comparison of individually adsorbed magnetic microgels (bMMG3) and pure microgels (bMG3) without MNPs. The images were taken by SFM in air. For the magnetic microgels, the MNPs in the less dense shell of the microgel are clearly visible around the gel particles. In contrast, the pure gels have a smooth spherical shape.

The deformation of the magnetic microgel particles bMMG3, swollen in water, was observed using scanning force microscopy under the influence of a lateral magnetic field. The magnetic field was increased step-like from 0 T to 0.375 T three times and an image of ten particles was recorded after every change of the field. *Figure 4.6* shows the relative change in volume, height and width (width: parallel to the field direction and parallel to the slow scan direction). Each value with the magnetic field is normalized with respect

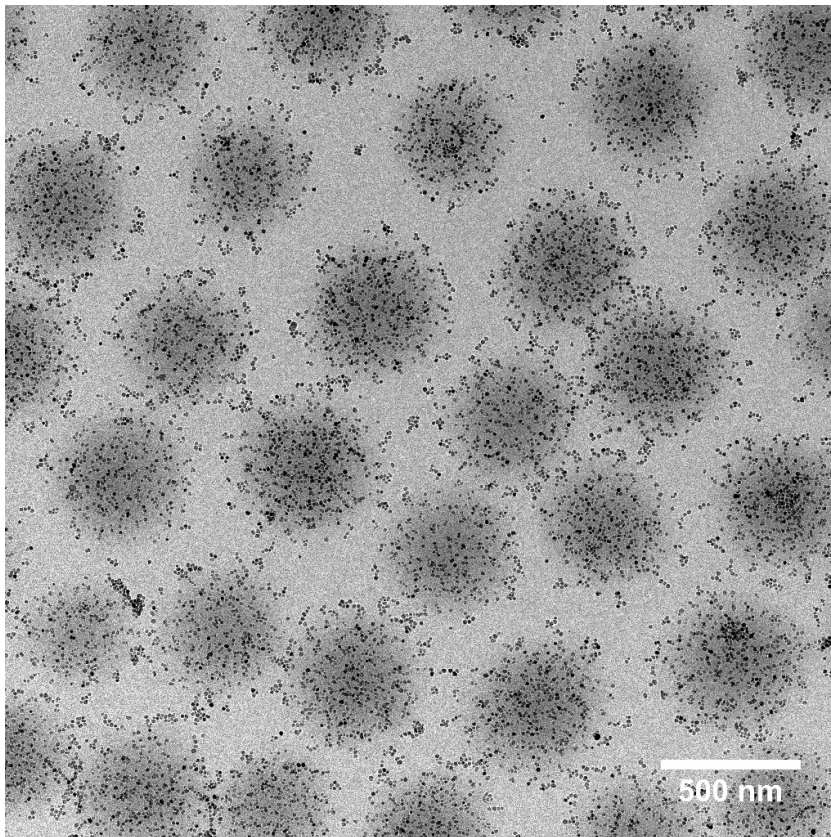


Figure 4.3: Transmission electron microscopy image of the bMMG2. The mean value for the embedded MNP is  $n = 275 \pm 36$ .

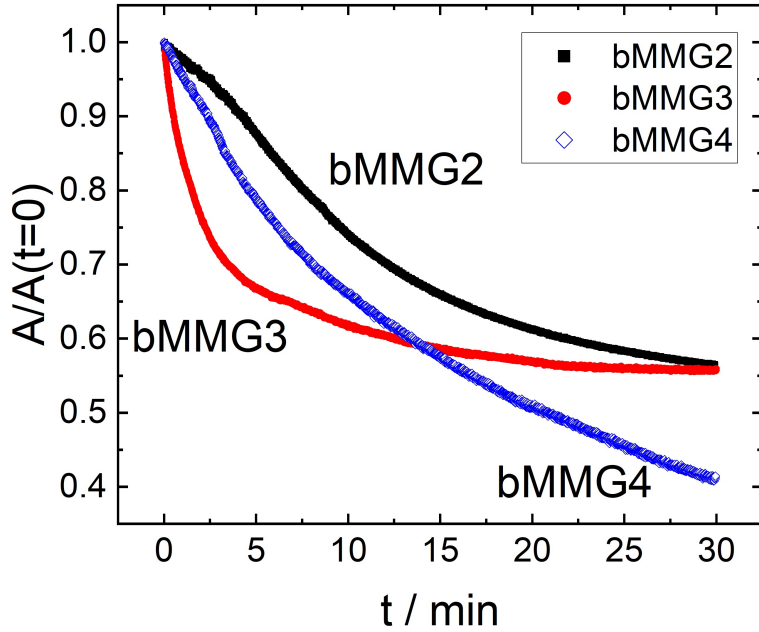


Figure 4.4: The absorbance in dependence of time during exposure to an external magnetic field. The absorbance is normalized to  $A(t=0)$ . Time "0" marks the time where the external magnetic field was applied. The magnetic microgel is pulled out of the beam path by the external magnetic field. To keep the graph clear, the error bars have been omitted.

to the cross section which was taken in the absence of the magnetic field. Both volume and height of the magnetic microgel decrease by up to 6% in the magnetic field, whereas the width increases by up to 7%. This means that the microgels are elongated in the direction of the magnetic field, which leads to a flattening and overall slightly smaller volume of the gels.

The elastic properties of the swollen magnetic microgels and their dependence on an external magnetic field were measured by force mapping of the area around a single particle. As has been shown before [2,3], the highest Young's modulus is found at the center of a microgel, whereas the modulus decreases as one gets closer to the edge of the gel. This is attributed to the fact that less dense materials are generally softer, and as the cross-linker density is lower in the outer regions of the gel, the Young's modulus decreases towards the outer periphery (core-shell structure). This is shown exemplary in *Figure 4.7*, which depicts the cross section and elastic properties of an exemplary magnetic microgel (without external field).

*Tab. 4.4* summarizes the Young's moduli. The values are the averaged Young's moduli in the center of three different particles. They were measured for pure microgels (bMG3), as well as magnetic microgels (bMMG3) with the external magnetic field being ramped up to 0.375 T and down again twice. Two results can be obtained here. First, the pure

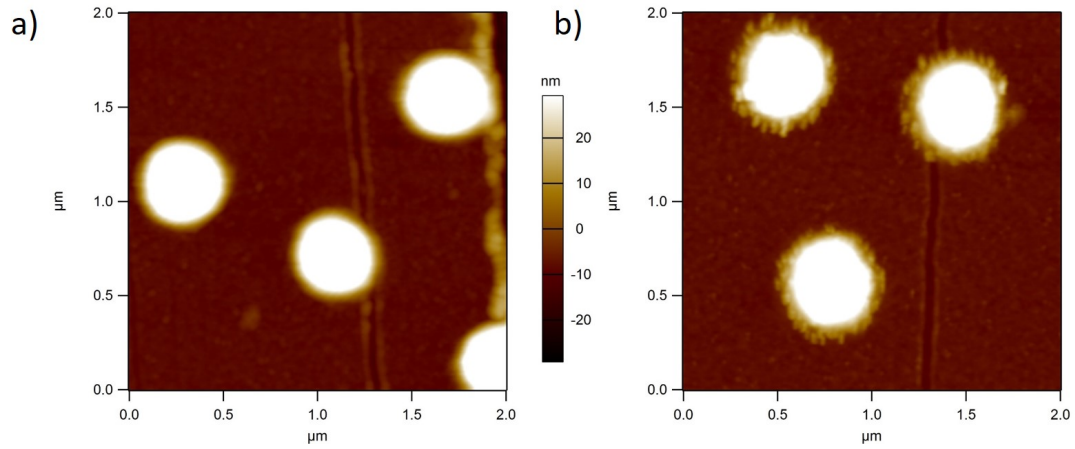


Figure 4.5: Comparison of adsorbed unloaded microgel bMG3 in a) and microgel particles loaded with magnetic nanoparticles bMMG3 in b) recorded by SFM in tapping mode against air. The scale bar is for both images identical.

microgels has a higher Young's modulus than the magnetic microgels. Second, there is no measurable influence of an external magnetic field on the Young's modulus of the magnetic microgels. bMG4 and bMMG4 show a similar trend, with values of 1453 kPa for bMG4, and only 623 kPa (at 0 T) and 767 kPa (at 0.375 T) for bMMG4.

Pure gel	0 T	0.375 T	0 T	0.375 T	0 T
$531 \pm 55$ kPa	$448 \pm 64$ kPa	$421 \pm 72$ kPa	$426 \pm 21$ kPa	$426 \pm 26$ kPa	$442 \pm 13$ kPa

Table 4.4: Averaged Young's moduli in the center of the magnetic microgel particles bMMG3.

Note that the MMG stickiness is strongly reduced compared to the pure MGs. Several magnetic microgels that could be observed in ambient air, detached from the surface by measuring in water.

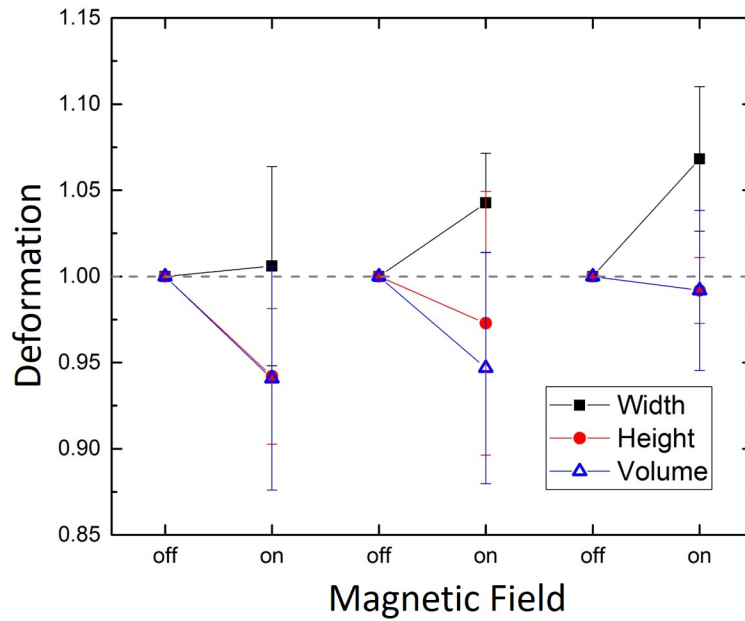


Figure 4.6: Relative change in volume, height and width parallel to the field direction of adsorbed magnetic microgels bMMG3 after applying a magnetic field of 0.375 T. The magnetic field was ramped up from 0 T to 0.375 T three times (three cycles).

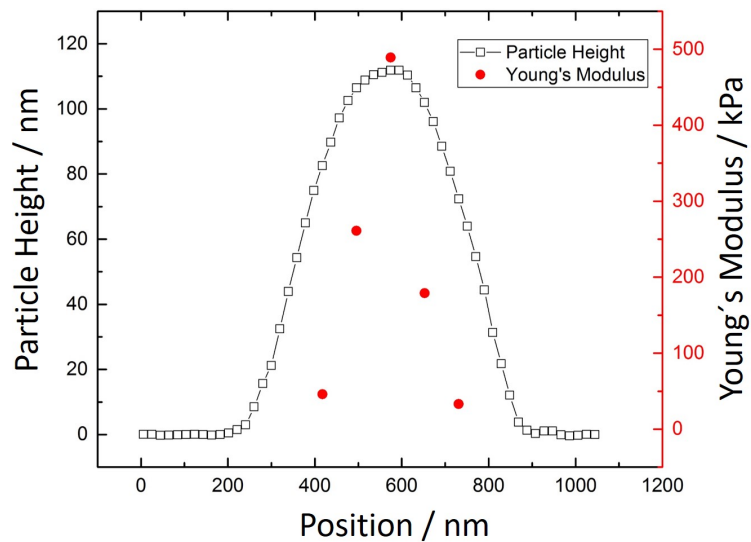


Figure 4.7: Cross section and Young's modulus of an exemplary magnetic microgel in the absence of an external field.

## 4.4 Discussion

The microgels with the highest positive EM (bMG4) could be obtained using a positively charged comonomer (AA) and a positively charged initiator (AAPH). Although the amount of comonomer was lower for bMG4 (2.5 mol%) than for bMG2 and bMG3 (5 mol%) the EM was twice as high ( $2.57 \mu\text{mcmV}^{-1}\text{s}^{-1}$  vs.  $1.17 \mu\text{mcmV}^{-1}\text{s}^{-1}$  and  $0.91 \mu\text{mcmV}^{-1}\text{s}^{-1}$ ). The reason might be the reduced tendency for aggregation between like charged comonomer and initiator. In case of oppositely charged comonomer (AA) and initiator (APS) aggregation was considered as a reason for uncontrolled polymerisation, especially for higher amounts of comonomer. The temperature dependent EM indicates a VPTT at about  $32^\circ\text{C}$ .

The sign of the microgel charge seems to have an important impact on the loading with MNPs. Microgels cannot be loaded with like charged MNPs, while oppositely charged MNPs lead to a pronounced loading. Comparing the different positively charged microgels (bMG2 (bMMG2), bMG3 (bMMG3), bMG4 (bMMG4)) it is obvious that electrostatic interaction is not the only important factor. Since there is no simple relation between EM and loading capacity it is assumed that also the internal structure of the microgels plays an important role for the MNP uptake. A decrease in starter concentration leads to a smaller amount of charged starter in the core. This may explain the difference in MNP uptake for bMG2 (bMMG2) and bMG3 (bMMG3). With bMG4 (bMMG4) the EM and the structure of the gel are changed to investigate the structural effect. The higher value of the EM for bMG4 than for bMG2 and bMG3 by increasing size is an effect due to higher particle charge. With increasing cross-linker concentration the internal structure changes to smaller meshes and therefore to a steric hinderance of the MNPs.

Loading with MNPs has several effects. First, the magnetic microgels show a higher hydrodynamic radius for all three microgels. This indicates that the repulsive force between the charged MNPs is stretching the microgel matrix. With the measured magnetic moment of  $3.77 * 10^{-19} \text{ Am}^2$  one can calculate  $\lambda$ , the ratio between the magnetic dipole-dipole interaction and the thermal energy at room temperature:

$$\lambda = \frac{\mu_0 m^2}{4\pi d^3 k_B T} \quad (4.1)$$

with the vacuum permeability  $\mu_0$ , the magnetic moment  $m$ , the particle diameter  $d$ , the Boltzman constant  $k_B$ , and the temperature  $T$ . The obtained value of  $\lambda = 0.58$  shows that the thermal energy dominates, which supports the observation that the particles are stable at  $20^\circ\text{C}$  and do not form aggregates due to magnetic interaction.

From the Grahame equation one can calculate the charge density  $\sigma$  [54]

$$\sigma = \frac{2\epsilon_0\epsilon_r k_B T}{e\delta} \sinh \frac{e\zeta}{2k_B T} \quad (4.2)$$

with the vacuum permittivity  $\epsilon_0$ , the relative permittivity  $\epsilon_r$ , the Debye length  $\delta$ , the zeta potential  $\zeta$ , and the elementary charge  $e$ . An average charge of  $Z = 14 \text{ e}$  per MNP

is obtained. The electrostatic repulsion is 6.4 times larger than the magnetic dipole dipole attraction.

Second, due to the negative charge of the MNPs ( $-70$  mV at pH 10) the positive EM of the microgel decreases and even leads to a charge reversal for bMG2 (bMMG2), bMG3 (bMMG3), and bMG4 (bMMG4). By increasing the temperature beyond the VPTT, the EM becomes more negative for all magnetic microgels. The MMGs show the typical behavior for microgels, i.e. the value of the EM increases above the VPTT since the charges are accumulated at the outer shell of the microgels. This non monotonic behavior is typical for oppositely charged starter and comonomer. After loading with MNPs this effect is not dominating anymore and the behavior becomes monotone.

The ability to pull the magnetic microgel out of the dispersion is a clear hint for a net magnetic moment which can be induced by the external inhomogeneous magnetic field. During loading, the MNP are not oriented and the directions of the dipole moments are isotropically distributed. That means, that the magnetic microgel has no net magnetic moment in absence of an external magnetic field. The fact that magnetic microgel particles can be moved by an external magnetic field is a clear hint that the MNPs can be oriented within the microgel along the axis of the magnetic field. Either the MNPs are not fixed and can rotate freely within the microgel network or they transfer the torque to the microgel structure. With increasing number of MNPs inside the microgels the separation speed increases. As it is expected with increasing number of MNPs the induced magnetic moment increases. The low separation yield of 40 % may originate from the non ideal measurement setup, e.g. the position of the magnet. Additionally, may be some pure microgels be still present in the dispersion. Furthermore, the data of bMMG4 suggest that the full separation process is not completed after 30 min. The origin of the different separation yields is unknown.

The TEM images show that the MNPs are isotropically distributed over the gel profile. For a homogeneous MNPs distribution within the microgel particles one would expect a higher concentration of MNPs in the center of the microgel particles. Since the TEM image is a 2D projection the observed isotropic distribution of MNPs for one microgel particle leads to the assumption that the MNPs are rather attached to the outer shell of the microgels. The increasing contrast of the microgel particles towards their center indicates a higher polymer density due to increasing concentration of cross-linker towards the center of the microgel particle. This is already known from literature [21] and is explained by faster reaction kinetics of the cross-linker in comparison to the monomer. The density gradient is also supported by mechanical studies, which show a higher Young's modulus for the center of the microgels than for the outer shell [2, 3, 112]. With increasing cross-linker concentration the mesh size decreases and the MNPs are not allowed to penetrate due to sterical hinderance. This also explains why the loading decreases for the bMMG4 (highest cross-linker concentration) although bMG4 has the highest positive charge.

The adsorbed magnetic microgels (bMMG3) elongate along the direction of the magnetic field, and contract perpendicular to the surface and to the field. This behavior corresponds to 2D simulations by Weeber *et al.* [100]. The MNPs are not chemically bound to the microgel and thus can rotate without strong interaction with the gel ma-

trix. In this case, the application of a magnetic field might lead to the formation of chain-like arrangements of MNPs parallel to the field. This could explain the observed deformation. Obviously, the arrangement of MNPs is not significant enough to influence the Young's moduli of the gels. The presence of the MNPs already decreases the Young's moduli. Furthermore, the MNPs are not present in the microgel core. The higher cross-linker content prevents the migration of the MNPs. Thus the microgel core is not reactive to the external magnetic field. This will further be discussed in *Chapter. 6*. This effect might be related to the increase in the microgel size after loading with MNPs. This increase is probably caused by repulsion between the MNPs, which makes the meshes inside the microgel grow. Hence, more water can get inside the gel and make it swell more. The fact that there is a charge reversal due to the loading with MNPs is a hint that not all charges are compensated and that additional counter ions are introduced into the system, that increases the osmotic pressure and thus might be another explanation for the swelling. This swelling could explain why the hybrid magnetic microgels are softer than pure microgels. The MMGs detach easily from the surface. The detachment is a large challenge for imaging the MMGs with the AFM. In *Chapter 11* the addition of allyl mercaptan is discussed as a additional bonding agent between the MG and the gold wafer.

## 4.5 Conclusion

Magnetic microgels made of PNIPAM based microgels and  $CoFe_2O_4@PAA$  MNPs have been successfully prepared and characterized. In case of oppositely charged microgels and MNPs a pronounced MNP uptake by the microgels could be detected. Furthermore, no simple relation between the value of the EM of the microgels and the MNP uptake could be found. This implies other factors like the internal structure being important for the loading capacity.

The hydrodynamic radius increases after the MNP loading due to the electrostatic repulsion of the MNPs and an increase in osmotic pressure. This is supported by the measurements of the elasticity and the decrease of the Young modulus for the magnetic microgels compared to the pure gels.

The magnetic microgels show a magnetic separability and their thermosensitive response is still preserved after loading with MNPs.

Additionally, a response of the ferrogel to an external magnetic field has been detected. Magnetic microgels elongate in field direction and their volume shrinks anisotropically. This effect is however not strong enough to induce a pronounced change in their elastic behavior. The type of magnetic microgel particles presented here are promising candidates for actuating systems. In *Chapter 6* the MNP distribution will be addressed. As this study has shown the number of MNPs inside the microgel is also influenced on the cross-linker concentration and most likely also on its distribution. *Chapter 5* will show the influence of different synthesis methods on the cross-linker distribution.

## 5 Kinetics of Microgel Formation

The experiments concerning the microgels *bMG7*, *fMG1*, *fMG2*, *fMG3*, *sbMG1* were carried out together with Zehn Zhang as part of her studies in Material Science. The mass spectrometry measurements were performed by the analytical service of the TU Berlin.

### 5.1 Abstract

This study examines several PNIPAM microgels, synthesized with different methods. The study aims to find differences in the resulting microgels, based on used synthesis method. For this, crucial parameters such as the monomer and cross-linker conversion rate is measured with mass spectroscopy. Additionally, several samples were taken after different reaction times during the polymerization to get information about the distribution of the cross-linker. It is shown that the swelling ratio as a function of particle size is not sufficient to distinguish between homogeneous or heterogeneous cross-linker microgels. The samples were analyzed with dynamic light scattering (DLS) and Zeta-sizer. Overall the study shows that the reaction time can be reduced from 90 min to 10 min. Additionally the most prominent parameter for the feeding method is the fed amount of monomer.

### 5.2 Introduction

In most of the studies, microgels have been synthesized with the batch method which produces heterogeneously cross-linked microgels with a dense core and a fluffy shell [112]. Also homogeneously cross-linked microgels were prepared to obtain a constant mesh size in the microgel network [89, 119]. The internal network structure plays an important role in the micromechanical properties. Increasing the cross-linker concentration increases the elastic modulus [118]. Acciaro *et al.* [89] proposed that the internal structure can be investigated by plotting the swelling ratio against the particle size. The idea is, that for homogeneously cross-linked microgels the average mesh size is constant over the whole microgel growth. This results in a constant swelling ratio as a function of particle size. The swelling ratio plotted against the particle size may not be the right strategy. Specially if both were measured with the DLS. The contrast variation between the microgel network and the water is different for these two types of microgels, because the density of the polymer is different. Therefore, the scattered light does not only depend on the particle motion/size but also on its internal structure. A same radius at 60 °C in the collapsed state suggests that the same amount of monomer is consumed. A

size difference at 20 °C for the same microgels suggests that their internal structure is different. This study aims to determine crucial parameters for the microgel synthesis for later investigations on the internal structure. Therefore, the reaction rate of NIPAM and BIS were measured. These parameters were used to synthesize microgels by different methods. These microgels were used to evaluate the proposed measure of homogeneity. Beside investigating the internal structure, this study also shows a way to decrease the workload and energy needed to perform such microgel syntheses. All microgels were prepared with the same amount of monomer and cross-linker. The first two microgel in this study were used to calculate the monomer and cross-linker conversion rate (bMG5, bMG6). The microgels bMG7, fMG1, fMG2, fMG3 and sbMG1 were studied to determine the difference in internal structure due to the different synthesis methods. *Table 3.1* shows the microgels composition.

## 5.3 Results

### 5.3.1 Mass Spectrometry

*Figure 5.1* shows the results of mass spectrometry measurements for bMG5 and bMG6 respectively. The amount of monomer is plotted against the reaction time. The absolute amount of monomer (*Figure 5.1*) is fitted with a simple exponential decay. For both microgels the amount of NIPAM and BIS decreases with increasing reaction time. The consumption of the corss-linker is faster. *Table 5.1* shows the reaction rate constants.

Sample	$k(NIPAM)/s^{-1}$	$k(BIS)/s^{-1}$
bMG5	0.0966	0.181
bMG6	0.309	0.386

Table 5.1: Reaction rate constants of NIPAM and BIS for the two samples bMG5 and bMG6. The constants are calculated from the simple exponential decay fitted to the mass spectrometry data.

The relative amount of NIPAM and BIS shows that the concentration of BIS decreases faster and can be used to easy compare both microgels.

### 5.3.2 Dynamic Light Scattering

*Table 5.2* lists the hydrodynamic radii of the microgels. *Figure 5.2* shows the hydrodynamic radii agains the reaction time for the microgels: bMG7, fMG1, fMG2, fMG3, sbMG1 at 20 °C and 60 °C. The hydrodynamic radius of the microgels increases with increasing reaction time. The type of increase in hydrodynamic radius at 20 °C can be divided in to two groups. One group consists of the batch and semi-batch microgels: bMG7 and sbMG1 and the grow process is flattened for  $r_H$  at higher reaction times. The other group consists of the feeding microgels. For the feeding microgels a strong increase in  $r_H$  is observed against reaction time. The hydrodynamic radius at 60 °C shows an increase in size with increasing reaction time as well. Furthermore, the radii

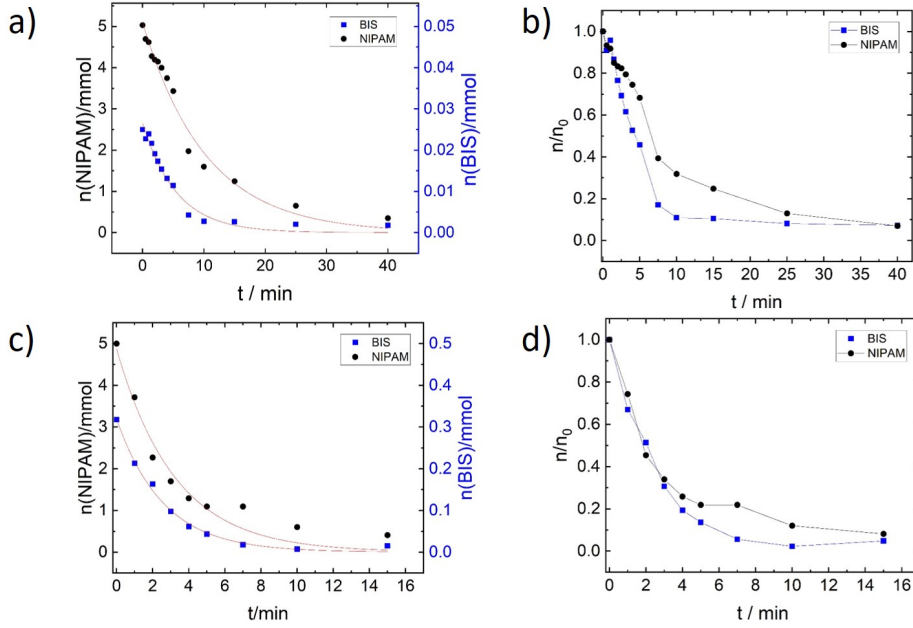


Figure 5.1: Mass spectrometry data for monomer consumption during the batch polymerization for bMG5 (a) and b)) and bMG6 (c) and d)). In a) and c) the absolute amount of substance against reaction time is shown and in b) and d) the relative concentration normalized with respect to the monomer concentration at  $t = 0$  min. The solid red line is the simple exponential decay fitted to the data. The estimated error bars are smaller as the symbols.

at 60 °C are smaller compared to the radii at 20 °C. One outlier (circled in red) can be seen for 60 °C and is excluded from further discussion.

In *Figure 5.3* the hydrodynamic radius is plotted against the feeding volume. It can be seen that for all microgels the particle size increases with increasing feeding volume and the growth rates are similar.

*Figure 5.4* shows the hydrodynamic radius in dependence of the temperature of the microgels after the full reaction time for bMG7, fMG1, fMG2, fMG3, sbMG1. In a) is a detailed view of bMG7 in b) the overview for the other MGs. The error bars for the overview are removed for sake of clarity. The heating measurements are colored in red and filled symbols and the cooling measurements in blue and empty symbols. All graphs show a decreasing hydrodynamic radius with increasing temperature. In the swollen state the microgels start to shrink for even small temperature changes. For higher temperatures above the VPTT the hydrodynamic radius is constant. The hydrodynamic radius before and after the heating/cooling cycle is the same. In the swollen state the microgel size is different. The feeding microgels are the smallest, the batch microgel is larger and the semi-batch microgel is the largest.

At the collapsed state (at 60 °C) all microgel radii are of similar size except the semi-batch. *Table 5.2* shows the hydrodynamic radius and the swelling ratio.

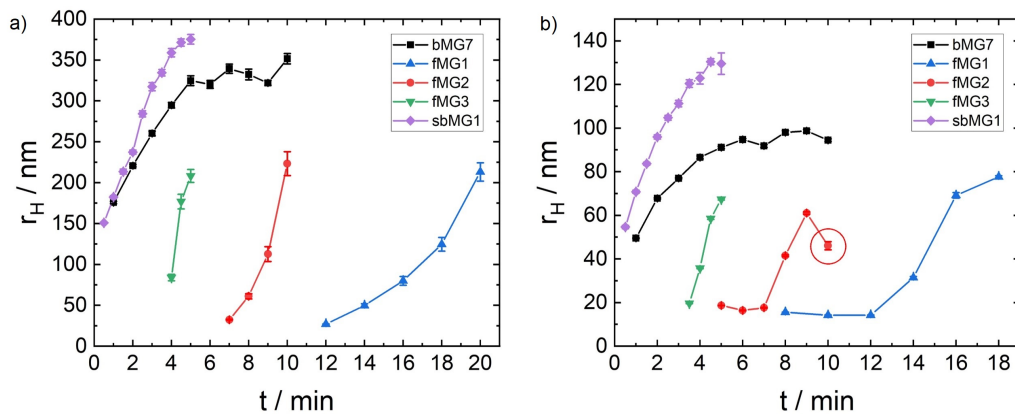


Figure 5.2: Hydrodynamic radius plotted against the reaction time. In a) the hydrodynamic radius at 20 °C and in b) at 60 °C. The red circle is a outlier that will not be taken into account for further discussion.

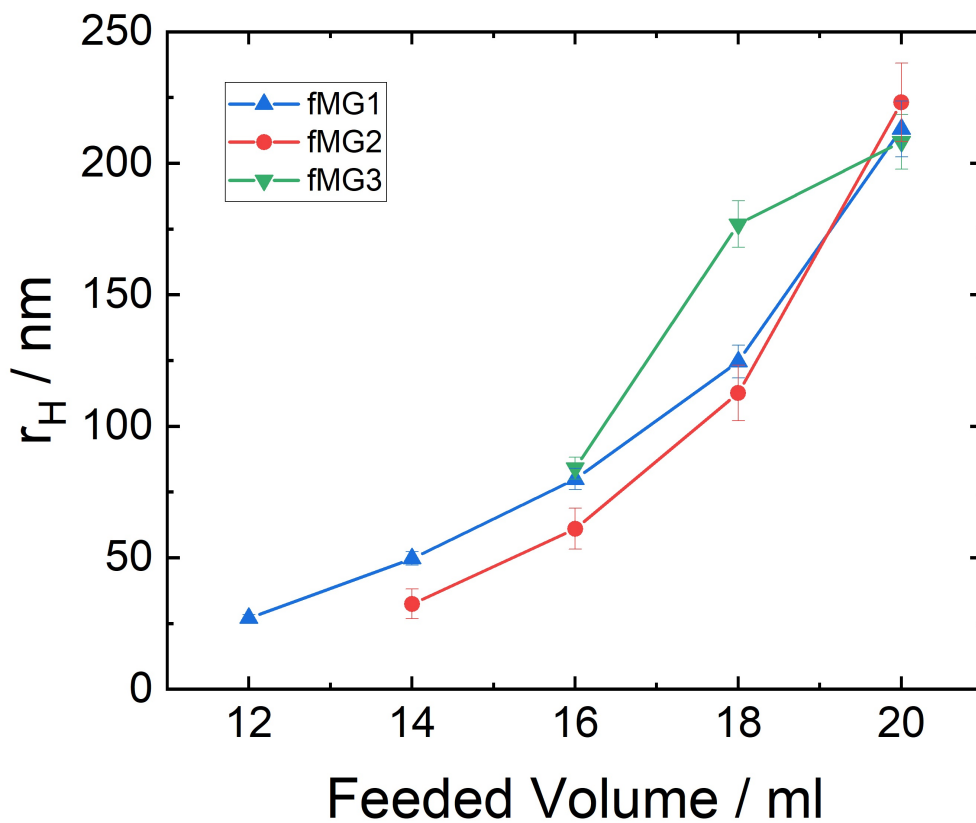


Figure 5.3: The hydrodynamic radius of microgels (fMG1, fMG2, fMG3) plotted against the feeding volume.

Acciario *et al.* suggested the swelling ratio as a measure for the cross-linker distribution. In *Figure 5.5* the swelling ratio ( $\alpha$ ) is plotted against the reaction time (see part a)) and against the hydrodynamic radius at 60 °C (see part b)). Beside for fMG3 all other microgels show a constant swelling ratio against reaction time. This effect is even more visible when plotting the swelling ratio against the hydrodynamic radius. For fMG3 the swelling ratio increases with increasing reaction time and particle size.

Sample	Polymerization Method	$r_H(20\text{ °C})$ in nm	$r_H(60\text{ °C})$ in nm	$\alpha$	VPTT in °C	$\mu(20\text{ °C})$ in $\mu\text{cmV}^{-1}\text{s}^{-1}$
<i>bMG5</i>	Batch	54	%	%	%	0.859
<i>bMG6</i>	Batch	248	%	%	%	1.31
<i>bMG7</i>	Batch	333.3	88.1	54.2	28.3	0.08
<i>fMG1</i>	Feeding (1 ml/min)	173.0	90.1	7.1	29.4	0.163
<i>fMG2</i>	Feeding (2 ml/min)	153.8	80.9	6.9	29.6	0.72
<i>fMG3</i>	Feeding (4 ml/min)	274.3	79.2	43.2	29.5	0.04
<i>sbMG1</i>	Semi-Batch	430.6	107.0	65.2	29.1	0.51

Table 5.2: Hydrodynamic radius and electrophoretic mobility of the studied microgels. The listed values were measured for the microgels after the synthesis was finished.

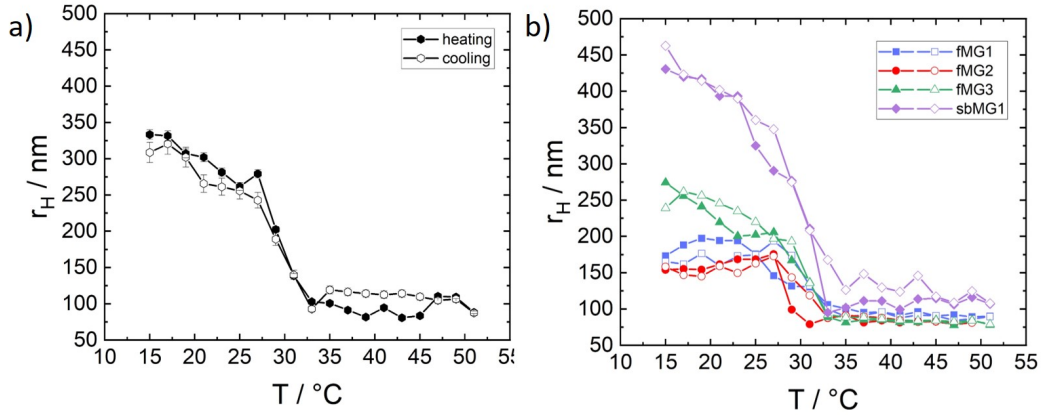


Figure 5.4: Hydrodynamic radius against temperature for the final microgels. In a) is exemplary the detailed graph shown for the heating (filled symbol) and cooling (empty symbols) of *bMG7*. In b) is a general overview shown of the heating and cooling for *fMG1*, *fMG2*, *fMG3*, *sbMG1*. In b) the error bars have been omitted for sake of clarity.

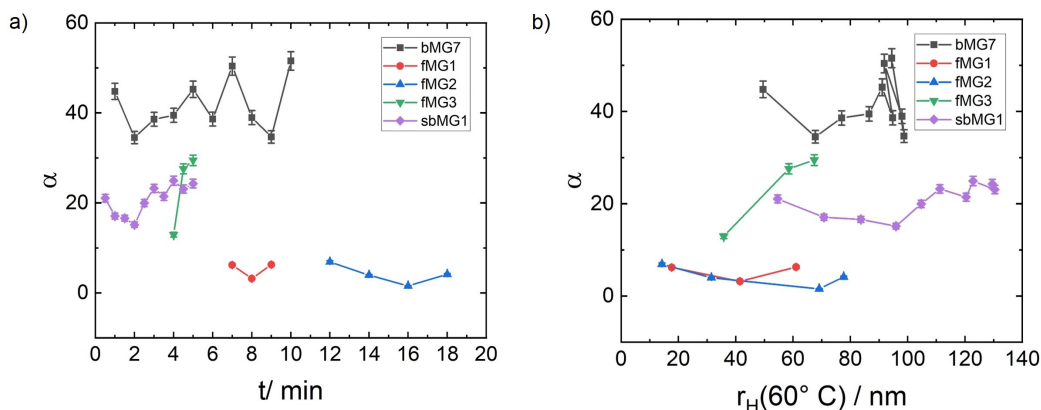


Figure 5.5: In a) is the swelling ratio plotted against reaction time and in part b) the hydrodynamic radius at  $60^\circ \text{C}$ .

### 5.3.3 Electrophoretic Mobility

Figure 5.6 shows the electrophoretic mobility ( $\mu$ ) plotted against the temperature. In part a) is in detail shown bMG7 and in part b) an overview for fMG1, fMG2, fMG3, sbMG1. The heating measurements are shown in red and filled symbols, the cooling measurements are shown in blue and empty symbol. The electrophoretic mobility is positive and increases with increasing temperature. The electrophoretic mobility above the VPTT reaches a plateau. The electrophoretic mobility for all microgels at  $20^\circ \text{C}$  is similar but varies at  $60^\circ \text{C}$ . After the complete heating/cooling cycle the electrophoretic mobility is back to its initial value. The highest  $\mu$  can be observed for fMG2 and the lowest for fMG3. Table 5.2 shows the electrophoretic mobility.

## 5.4 Discussion

Seven microgels have been successfully synthesized with various methods such as batch, feeding and semi-batch. The first two microgels (bMG5, bMG6) show that the amount of available monomer influences the reaction rate constant as well as the microgel size. With a higher amount of available monomer the microgels are growing faster and become larger. This is shown by the mass spectrometry data and DLS. For shorter times than 10 min the total consumption reaches 95 % and is in good agreement with literature values [89]. Furthermore, the consumption ratio of BIS to NIPAM is also in good agreement with the literature [62, 89]. The difference in consumption rate of monomer and cross-linker leads to a structure that is known as heterogeneously cross-linked microgels. They have a higher amount of cross-linker in the particle center and a fluffy shell [112].

The difference in reaction time between bMG5, bMG6 and bMG7 plays a minor role in the synthesis of suitable microgels. Reducing the reaction time from 90 min to 10 min is not influencing the microgels properties such as swelling and shrinking. It is unknown how the shortend reaction time influences the size of the MGs. 95 % of the monomers

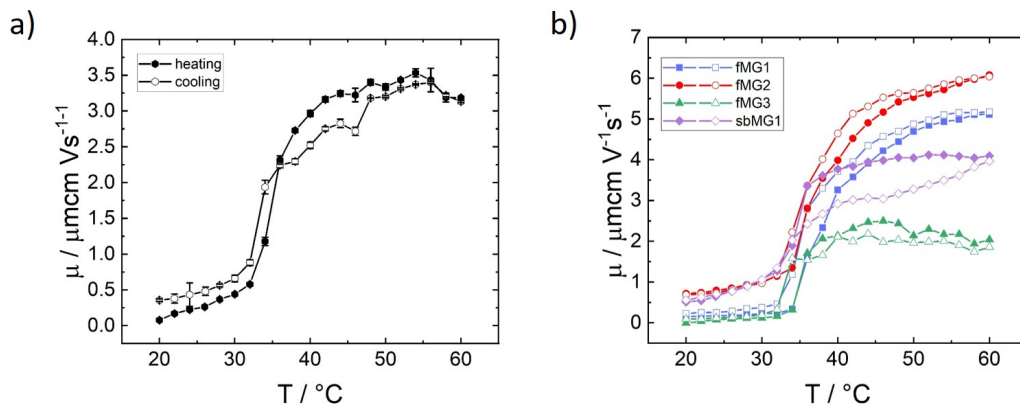


Figure 5.6: Electrophoretic mobility plotted against the temperature. In a) is exemplary the detailed graph shown for the heating (filled symbol) and cooling (empty symbols) of bMG7. In b) is a general overview shown of the heating and cooling for fMG1, fMG2, fMG3, sbMG1. In b) the error bars have been omitted for sake of clarity.

is already consumed. The microgel growth (volume) after 10 min can be considered small. Additionally, the radius scales with  $V^{1/3}$ . The shrinking and swelling of the microgels show the well known behavior with a VPTT close the literature value for the LCST of PNIPAM [58]. The small deviations in the size for cooling and heating cycle originate from internal relaxation processes during the first shrinking and swelling, as known from literature [80, 81, 101]. The hydrodynamic radius at 60  $^{\circ}\text{C}$  shows that the amount of polymerized monomers is similar for all three synthesis methods. This further supports the findings from the mass spectrometry data on bMG5 and bMG6. The size difference at 20  $^{\circ}\text{C}$  is indicates a different internal structure in dependence of the synthesis method. The batch method leads to the well known core/shell structure while the feeding and semi-batch method are suppose to give homogeneously cross-linked microgels. Acciaro *et al.* proposed that the internal cross-linking structure can be investigated by plotting the swelling ratio against the hydrodynamic radius in the shrunken state [89]. The expected results could not be reproduced (feeding and semi-batch MGs would give a constant, batch MGs an asymptotically increase). The swelling ratio plotted against the reaction time and the size gives a more or less constant value for all MGs, except for fMG3. This shows, that this evaluation is not suitable to get information about the cross-linker distribution inside the microgels. This finding is further supported by the work of Michael Eisele [34]. In contrast the findings in *Chapter 6* in *Figure 6.5* show that the cross-linker distribution can be seen in TEM images. They show that the batch microgel is heterogeneously cross-linked while the feeding microgel is homogeneously cross-linked. This will be discussed further in the next chapter. The batch and semi-batch microgels are growing faster compared to the feeding microgels and that the particle formation starts earlier during the reaction. This is caused by the abundance of the monomers. In the first few minutes the amount of available monomer

in these two methods is the highest. This also explains why no data points could be measured for the feeding microgels in the first few minutes, as the particle size is too small and the reaction kinetic is dominated by the feeding speed. fMG3 microgels grow the fastest. With increasing monomer concentration the polymerization speed increases. The final particle size is independent of the feeding speed, but strongly depends on the total amount of available monomer and therefore on the amount of fed monomers. The measured electrophoretic mobility shows that the microgels are positively charged. The temperature dependent change of  $\mu$  is as well reflecting the shrinking and swelling behavior of the microgels. While the number of surface charges remain roughly the same the particle size decreases. Therefore, the surface charge density increases and the electrophoretic mobility increases proportional to the microgel size. Overall the microgels are responsive to the environmental temperature.

## 5.5 Conclusion

This study shows that the synthesis method influences the internal structure of microgels. This structural difference is achieved by different synthesis methods. It could be shown that the batch method leads to heterogeneously cross-linked microgels. This finding is well known in literature as the cross-linker BIS is faster consumed as NIPAM. The proposed measure of homogeneity by Acciaro *et al.* could not be verified. The proposed constant swelling ratio against particle size was found for nearly all microgels and is therefore not suitable to determine the homogeneity of the cross-linker distribution. For future applications and microgel syntheses, it is therefore of great interest to find such a measure for the homogeneity. All microgels exhibit the VPT at a temperature close to 32 °C in accordance to the literature. The data show that with increasing monomer concentration the polymerization rate increases. For the feeding reaction the upper limit of the feeding speed would be the batch method. The batch and semi-batch method show that most of the particle formation takes place in the first few minutes. The findings on the reaction rate constant can lead to further developments in the field of homogeneously cross-linked microgels. Besides the crucial parameter for future feeding reactions, it is also important that the reaction time could be reduced from 90 to 10 minutes without a notable loss of microgel properties or responsiveness. This reduction in synthesis time reduces the energy consumption, nitrogen flow and workload. Therefore, the synthesis becomes more environmentally friendly. This is of special interest for future industrial applications and upscaling.

## 6 Distribution of $CoFe_2O_4$ Nanoparticles Inside PNIPAM Based Microgels of Different Cross-Linker Distributions

This study was performed in collaboration with Sebastian Friedrich (né Backes) and Nadir Möller. They performed the measurements of the elastic moduli. The magnetic nanoparticle were synthesized by Stephan Hinrichs. This study has been published in "Distribution of  $CoFe_2O_4$  Nanoparticles Inside PNIPAM Based Microgels of Different Crosslinker Distributions", Marcus U. Witt, Stephan Hinrichs, Nadir Möller, Sebastian Friedrich, Birgit Hankiewicz, Regine von Klitzing, *J. Phys. Chem. B*(2019), 123, 10, DOI:10.1021/acs.jpcc.8b09236

### 6.1 Abstract

The aim of this study is to tailor the inner structure of positively charged poly-(*N*-Isopropylacrylamid-co-allylamine) (P(NIPAM-co-AA)) microgels for a better control of the distribution of negatively charged magnetic cobaltferrite ( $CoFe_2O_4@CA$ ) nanoparticles (MNPs) within the microgels. Therefore, two different strategies are followed for the microgel synthesis: the (one pot) batch method which leads to a higher cross-linker density in the microgel core and the feeding method which compensates different reaction kinetics of the cross-linker and the monomers. The latter one is expected to result in a homogeneous cross-linker distribution. Information about the cross-linker distribution is indirectly gained by measuring the elastic modulus via indentation experiments with an atomic force microscope. While the batch method results in a higher elastic modulus in the center of the microgel indicating a core/shell structure the feeding method leads to a constant elastic modulus over the whole microgel. The loading with MNPs and their distribution is studied with transmission electron microscopy (TEM). The TEM images show a large difference in the MNP distribution which is correlated to the cross-linker distribution of both types of microgels. The batch method microgel has a low MNP concentration in the core. The feeding method microgel shows a much more homogeneous distribution of MNPs across the microgel. The latter one shows also a stronger charge reversal which is a hint for a higher loading of the microgel from the feeding method. Dynamic light scattering (DLS) and electrophoretic mobility (EM) measurements demonstrate that for both types of microgels the temperature sensitivity is preserved after loading with MNPs.

## 6.2 Introduction

The reported elongation of magnetic microgels in magnetic field direction in *Chapter. 4* is small. It is assumed that the empty core is unresponsive to external fields (magnetic or light). An obvious strategy to increase the response to external fields, is to increase the amount of NPs inside the microgel. The number of MNPs embedded within the microgels depends on the microgel composition, which was already demonstrated in *Chapter 4* [101].

In *Chapter 4* [101] it was shown that the amount of embedded MNPs within oppositely charged microgels does not increase systematically with increasing charge of the microgel. Besides the charge the steric hindrance of the nanoparticles inside the microgel is assumed to be a key parameter. The steric hindrance is directly correlated to the mesh size of the microgel network and the MNPs size (including stabilizing coatings). Gawlitza *et al.* [57] changed the cross-linker density of the microgels and found an increasing distribution gradient of AuNPs with increasing cross-linker density. This finding was related to the established opinion that the core is higher cross-linked than the shell. For high cross-linker densities the core of the microgel was almost particle free. Still some of the gold NP could be used as hot spots to increase the microgel temperature [76]. In addition, the response of the MMGs to an external magnetic field was smaller as predicted in literature (see *Chapter 4*). This also seems to be originated in an unloaded microgel core. This "inactive" volume is not contributing to the response to an external magnetic field.

To increase the response to external fields, the distribution of NPs has to be changed. Assuming a homogeneous distribution of NPs results a highly responsive microgel, because the core volume is also loaded. In none of the mentioned works the influence of the internal microgel structure on the MNP distribution was studied.

In former studies microgels have been synthesized with the batch method which produces heterogeneously cross-linked microgels with a dense core and a fluffy shell [112]. This results in a smaller mesh size in the particle center and an increasing mesh size towards the microgel surface. The heterogeneous co-polymerization of the cross-linker into the polymer network is due to the faster reaction kinetics of the cross-linker in comparison to the one of the monomer (compare *Chapter 5*). Therefore, the MNP distribution within the microgels is heterogeneous, with a higher concentration within the fluffy shell.

The present chapter addresses the tailoring of the inner microgel structure in order to control the MNP distribution within the microgel. Two synthesis strategies are pursued: the commonly used batch method which results in a heterogeneous cross-linker distribution and the feeding method [89] which compensates the faster consumption of cross-linker. Acciaro *et al.* [89] showed in their study the homogeneous cross-linker distribution by measuring the swelling ratio in dependence of the particle size during the polymerization. This method did not give consistent results for the used MGs in *Chapter 5*. Therefore, in the present work the cross-linker distribution will be studied by scanning the local elastic modulus of the microgels with the atomic force microscopy based indentation method.

The present chapter contributes to two interesting topics related to PNIPAM based microgels. The first contribution is to understand the distribution of cross-linker as a result of the batch and feeding synthesis method. The second contribution is the influence of the different cross-linker distribution on the distribution of MNPs inside the microgel network. In this study the samples bMG8 and fMG4 were used. *Table 3.1* shows the microgel composition.

## 6.3 Results

### 6.3.1 Microgels (MGs)

#### *Hydrodynamic Radius*

*Figure 6.2* (empty symbols) shows the hydrodynamic radii of the two types of microgels versus temperature. The microgels show the well known shrinking and swelling behavior in dependence on the temperature. The process of shrinking and swelling is reversible. *Tab.6.1* shows the hydrodynamic radii of the microgels as well as the swelling ratio. The radius at  $T = 20\text{ }^{\circ}\text{C}$  for the fMG4 (feeding method) is slightly larger than for bMG8 (batch method). At  $T = 50\text{ }^{\circ}\text{C}$  bMG8 and fMG4 have a similar size. The swelling ratio for both microgels is as well similar. *Figure 6.1* shows in detail the full swelling and shrinking curves, i.e. the change in hydrodynamic radius against the temperature change. The VPTT is close to the expected  $32\text{ }^{\circ}\text{C}$ .

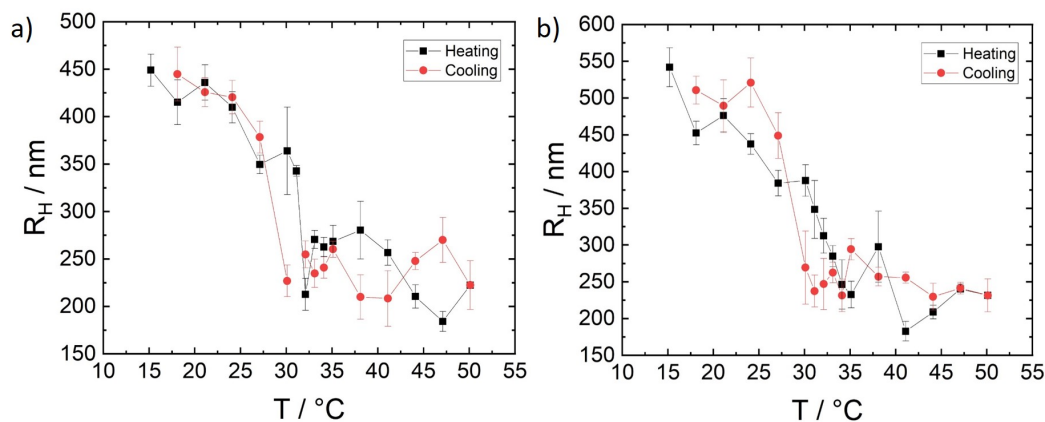


Figure 6.1: Swelling curves for the hydrodynamic radius in dependence of temperature for bMG8 in part a) (batch method) and fMG4 in part b) (feeding method).

#### *Electrophoretic Mobility (EM)*

*Figure 6.3* (empty symbols) shows the EM for microgel bMG8 (batch method) and fMG4 (feeding method). *Tab.6.1* shows the  $EM(\mu)$ . Both MGs have a positive electrophoretic mobility at  $T = 20\text{ }^{\circ}\text{C}$ . With increasing temperature the EM increases. The increase in EM is reversible for several cycles. At  $20\text{ }^{\circ}\text{C}$  the EM is similar for both gels.

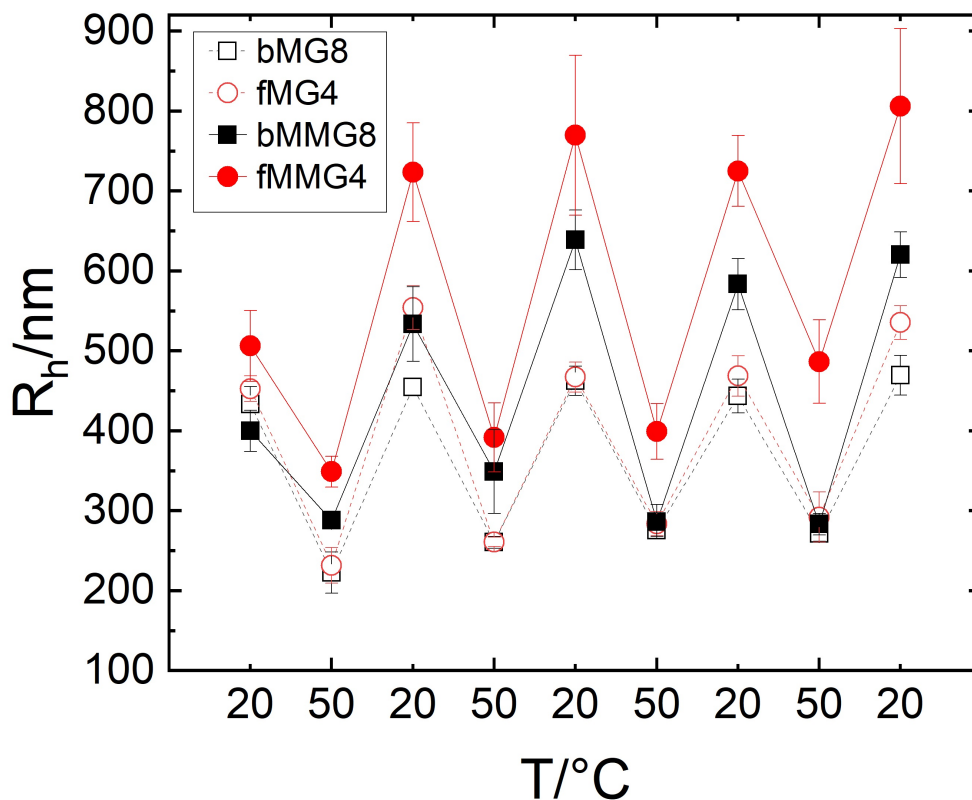


Figure 6.2: Hydrodynamic radius of the microgels and magnetic microgels, bMG8 (batch method) and fMG4 (feeding method) and bMMG8 and fMMG4 respectively in dependence on the temperature for four heating/cooling cycles.

At  $T = 50\text{ }^{\circ}\text{C}$  the EM is lower for fMG4 compared to bMG8. The difference in EM is constant for the different heating/cooling cycles.

#### *Nanomechanical Properties*

*Figure 6.4* shows the elastic modulus averaged over several particles. The range of the x-values reflects the lateral expansion of the microgels after adsorption. After adsorption onto the gold surface the difference in diameter is larger than before the adsorption. The diameter of bMG8 is around 500 nm and of fMG4 around 700 nm. This is a hint that the microgels are flattened on the surface. The elastic modulus is calculated from the force maps. For the bMG8 (batch method) the elastic modulus is higher in the particle center compared to the modulus at the circumference of the particles. In contrast the elastic modulus of the fMG4 (feeding method) is more or less constant over the whole particle diameter. This leads to the conclusion, that the cross-linker distribution inside the microgels (bMG8 and fMG4) is different. The overall elastic modulus of bMG8 is smaller as for fMG4.

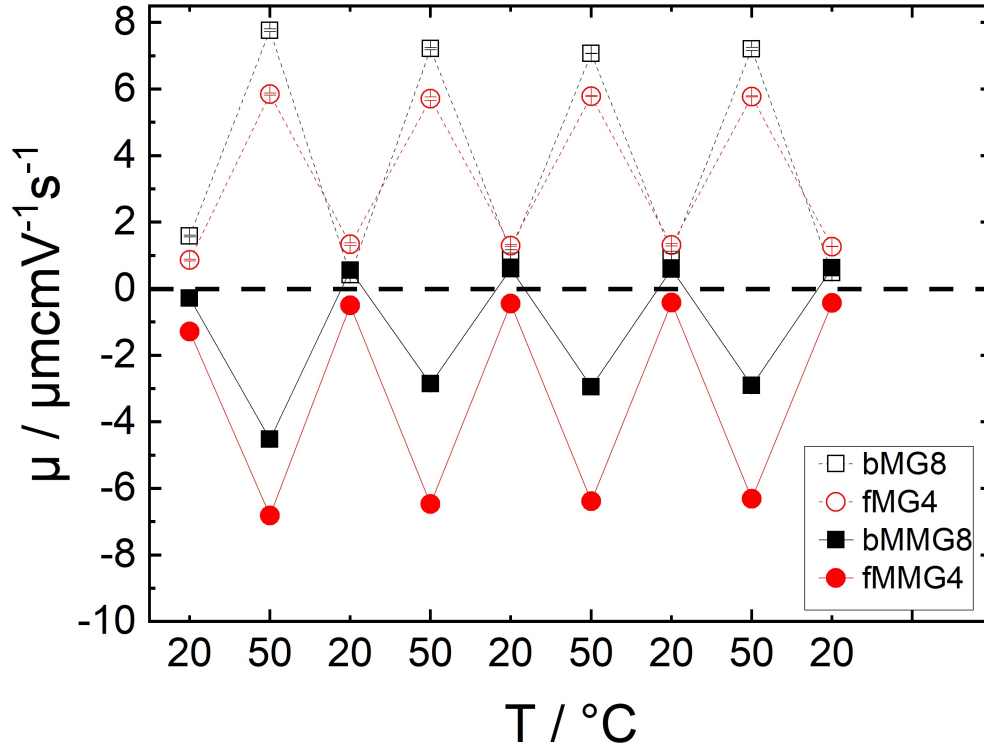


Figure 6.3: Electrophoretic mobility of the synthesized microgel and magnetic microgels, bMG8 (batch method) and fMG4 (feeding method) and bMMG8 and fMMG4 respectively in dependence on the temperature for four heating/cooling cycles.

#### *Transmission Electron Microscopy*

Figure 6.5 shows the TEM images of both MGs. bMG8 (batch method) shows a decreasing gray value from the particle center to the particle circumference. The contrast for fMG4 (feeding method) is constant through the whole particle.

### 6.3.2 Magnetic Microgels (MMG)

Based on these results the influence of the different cross-linker distributions on the MNP distribution can be investigated.

#### *Hydrodynamic Radius*

Figure 6.2 (filled symbols) shows the hydrodynamic radii for the magnetic microgels (bMMG8 and fMMG4). bMMG8 is smaller compared to fMMG4 at all measured temperatures. Again the process of shrinking and swelling is reversible over several heating/cooling cycles. Table 6.2 shows the hydrodynamic radii for the two magnetic microgels. The table shows as well the swelling ratio which is similar to the one before MNP incorporation (Table 6.1). The MMGs are larger compared to the unloaded MGs.

Sample	$r_H^{20\text{ }^\circ\text{C}} / \text{nm}$	$r_H^{50\text{ }^\circ\text{C}} / \text{nm}$	$\alpha$	$\mu^{20\text{ }^\circ\text{C}} / \mu\text{mcm V}^{-1}\text{s}^{-1}$	$\mu^{50\text{ }^\circ\text{C}} / \mu\text{mcm V}^{-1}\text{s}^{-1}$
bMG8	452	257	5.44	0.93	7.32
fMG4	495	266	6.44	1.21	5.78

Table 6.1: Characteristic measurements of the microgels, mean hydrodynamic radii  $R_h$  and the swelling ratio  $\alpha$  and mean electrophoretic mobility  $\mu$  (@20 °C and @50 °C). The mean values are calculated from several heating and cooling cycles.

### *Electrophoretic Mobility*

*Figure 6.3* (filled symbols) shows the EM for the magnetic microgels for several heating/cooling cycles, and *Tab.6.2* shows the mean EM at 20 °C and 50 °C. bMMG8 has a positive EM for temperatures below the VPTT. Above the VPTT the EM is negative. fMMG4 has a negative EM for all temperatures. This means that fMG4 exhibits a charge reversible by loading the microgel with MNPs. For bMG8(bMMG8) a charge reversal due to loading with MNPs can only be observed for the shrunken state (50 °C). The change of the EM against the heating/cooling cycles is reversible and constant.

Sample	$r_H^{20\text{ }^\circ\text{C}} / \text{nm}$	$r_H^{50\text{ }^\circ\text{C}} / \text{nm}$	$\alpha$	$\mu^{20\text{ }^\circ\text{C}} / \mu\text{mcm V}^{-1}\text{s}^{-1}$	$\mu^{50\text{ }^\circ\text{C}} / \mu\text{mcm V}^{-1}\text{s}^{-1}$
bMMG8	554	301	6.23	0.41	-3.
fMMG4	705	406	5.23	-0.62	-5.78

Table 6.2: Characteristic measurements of the magnetic microgels, mean hydrodynamic radii and mean electrophoretic mobility (@20 °C and @50 °C) and the swelling ratio.

### *Transmission Electron Microscopy*

*Figure 6.6* shows the TEM images of both MMGs. MNPs have a much higher contrast compared to the microgels and they dominate the TEM images. The polymer network of bMMG8 with its dangling ends becomes visible due to the adsorbed MNPs. fMMG4 has a more constant contrast for the whole microgel and the surface appears smoother with much less dangling polymer ends compared to bMMG8.

The number of MNP inside each microgel is so high that in the two dimensional image the particles overlap and vary strongly in contrast. A conventional analysis with *ImageJ 15.k* and the available features, such as *Particle Analysis* and *Watershed*, do not lead to a sufficient representation of the amount of MNPs inside the microgels. To determine the MNP distribution a self developed analysis with *ImageJ* was used. The TEM images are treated as follows: First, the background of the image was calculated using the rolling ball algorithm. Second, the calculated background is subtracted from the image. Third, the image is converted into a binary map. A box of constant length and width is extracted for each MMG. The box is slightly longer than the microgel to cover all MNP even for a more polydisperse microgel sample. The width of the box is chosen to

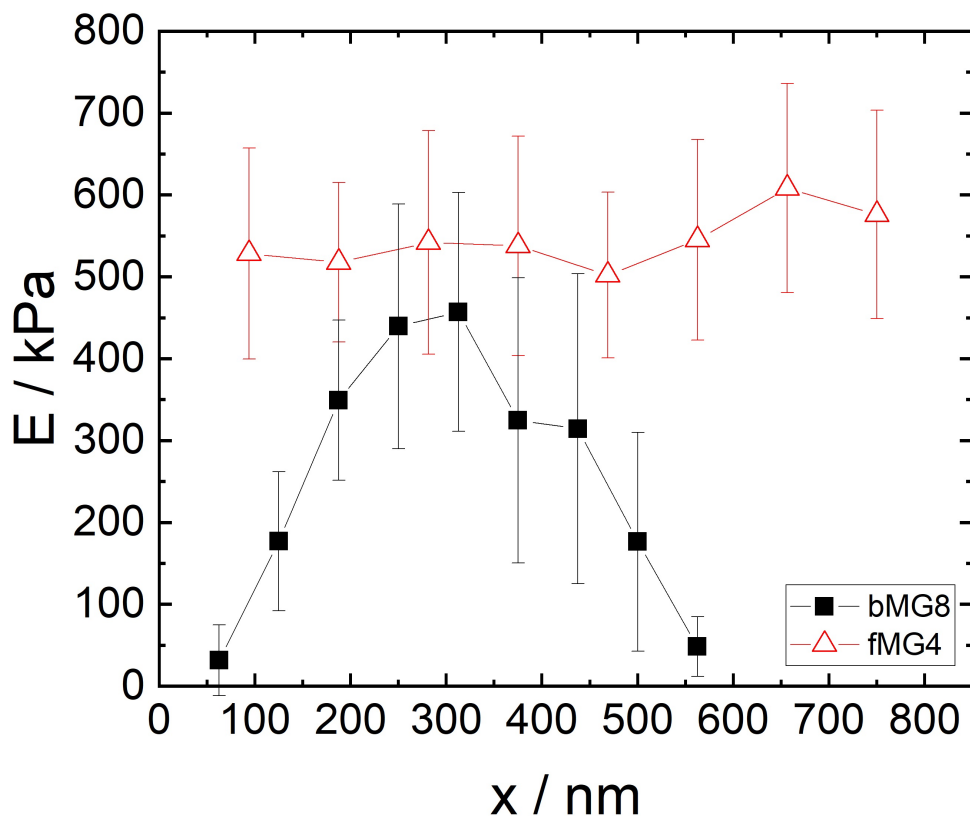


Figure 6.4: Elastic modulus for bMG8 (batch method) and fMG4 (feeding method) measured with AFM indentation method in water at 20 °C. The values are averaged over 10 microgels.

be as big as possible without getting any significant curvature effect. The treatment is depicted in *Figure 6.6-6.11* for both microgel systems. The black values along the width are summed up for 10 to 20 MMGs and averaged. The resulting values are called black pixel frequency. The black pixel frequency is a representation of the number of MNPs against the radius of the MMG.

*Figure 6.11* shows the black pixel frequency for the two MMGs. The histogram for bMMG8 (batch method) shows a more constant level for the black pixel frequency. With peaks of the black pixel frequency at both ends of the histogram. The histogram for fMMG4 (feeding method) shows a parabolic distribution of the black pixels, with the highest counts in the center.

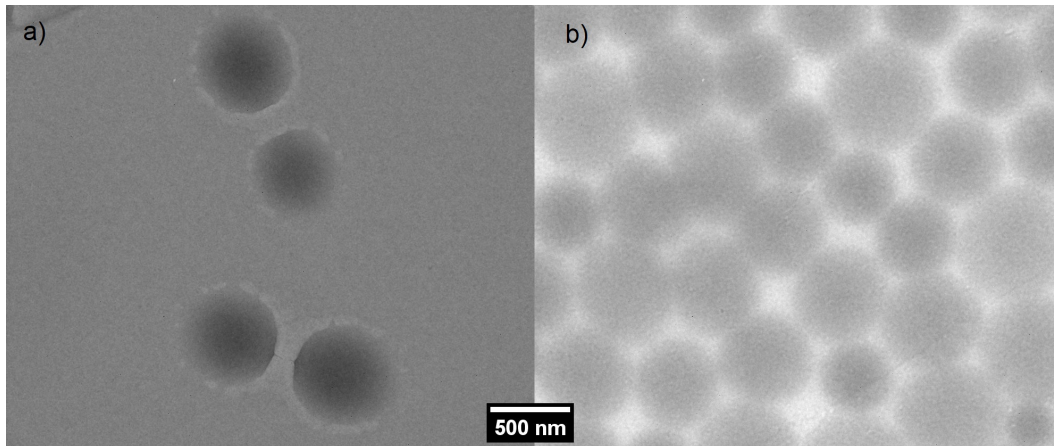


Figure 6.5: TEM images of bMG8 (batch method) in part a) and fMG4 (feeding method) in part b). The TEM images of both microgels are combined and the same contrast is applied to both images for better comparison.

## 6.4 Discussion

### *Microgels (MGs)*

Two different synthesis strategies were applied in order to tailor the inner structure of PNIPAM microgels. The PNIPAM microgels were synthesized with identical amounts of reactants via the batch method (bMG8) [94] and the feeding method (fMG4) [89]. Acciario *et al.* [89] used the swelling ratio against the particle size during the polymerization to verify the homogeneously cross-linked microgel (see *Chapter 5*). In the present study we use mainly the elastic modulus measured with AFM to determine the distribution of cross-linker inside the microgel. The measured elastic modulus is supported by TEM imaging.

The elastic modulus of the microgels (bMG8) from the batch method shows a well pronounced maximum in the particle center which has been already observed by former studies [4, 19]. It is explained by a dense core and a fluffy shell due to the faster consumption of the cross-linker in the polymerization compared to the monomer. The elastic modulus for the microgels (fMG4) from the feeding method is higher and constant over the whole diameter. This constant elastic modulus indicates a homogeneous distribution of cross-linker over the whole microgel. The TEM images support this findings of heterogeneously (bMG8) and homogeneously (fMG4) cross-linked microgels. The TEM images of the pure microgels bMG8 (batch method) and fMG4 (feeding method) (see *Figure 6.5*) show a decreasing contrast towards the particle circumference for bMG8 and a constant contrast for fMG4. This is the result of the different distribution of cross-linker in the two microgels systems with heterogeneously cross-linked microgel bMG8 and homogeneously cross-linked microgel fMG4. This is further supported by the TEM images of the MMGs. bMMG8 shows dangling ends of polymers loaded with MNPs. This supports the dense core/fluffy shell structure of the heterogeneously cross-linked

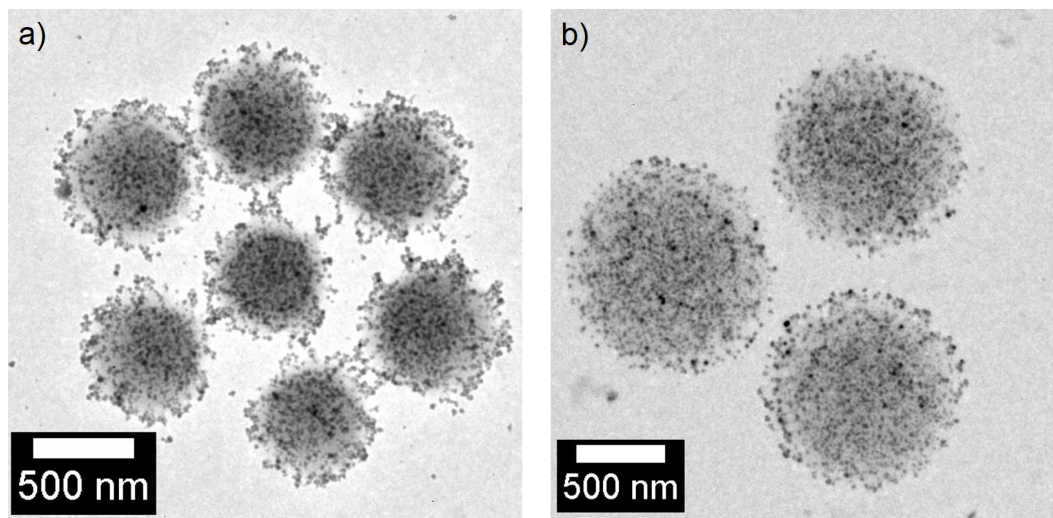


Figure 6.6: Untreated TEM images of PNIPAM microgels after loading with MNP. a) bMMG8 (batch method, bMG8,) b) fMMG4 (feeding method, fMG4).

bMG8.

The exact distribution of allylamine inside the microgel is unknown but can be estimated to be close to the cross-linker distribution as explained in the following. Two extreme cases are possible: First, the consumption rate of AA is faster than the consumption rate of the cross-linker. Because the distribution of AA in the batch synthesis would give a core/shell structure with a high amount of AA in the core and less in the shell. The distribution caused by feeding method would be homogeneous due to the constant feeding of AA during synthesis. In the second case the consumption rate of AA is slower as for the cross-linker. Then, the AA would be built in within the microgel with higher concentrations at the surface than in the center for both synthesis methods. The positive charges of the microgel would be located mainly on the surface. The core would be more or less charge neutral and the MNPs would accumulate on the microgel surface for both synthesis methods. In contrast, the present work shows clearly a homogeneous MNP distribution within homogeneously cross-linked microgels. This is a strong hint that the AA reaction kinetics is either similar or faster than the one of the cross-linker and the feeding speed is the dominating factor. Therefore the AA distribution is predicted to be similar to the cross-linker concentration in both synthesis methods. At a pH of 7 the microgels are slightly positive charge. To decrease the pH and therefore increase the charge of the microgels by protonating the AA is not desired due to the destabilization of the MNP suspension at lower pH. The MNPs are stabilized with citric acid and stable at pH 8. A pH below 7 would result in an aggregation of the MNPs before they can be embedded into the microgel.

The swelling and shrinking of the microgels in aqueous dispersions was studied with DLS. Both types of microgels shrink and swell reversibly. The size of the two microgels is nearly identical in the shrunken state, which is a strong hint that the same amount

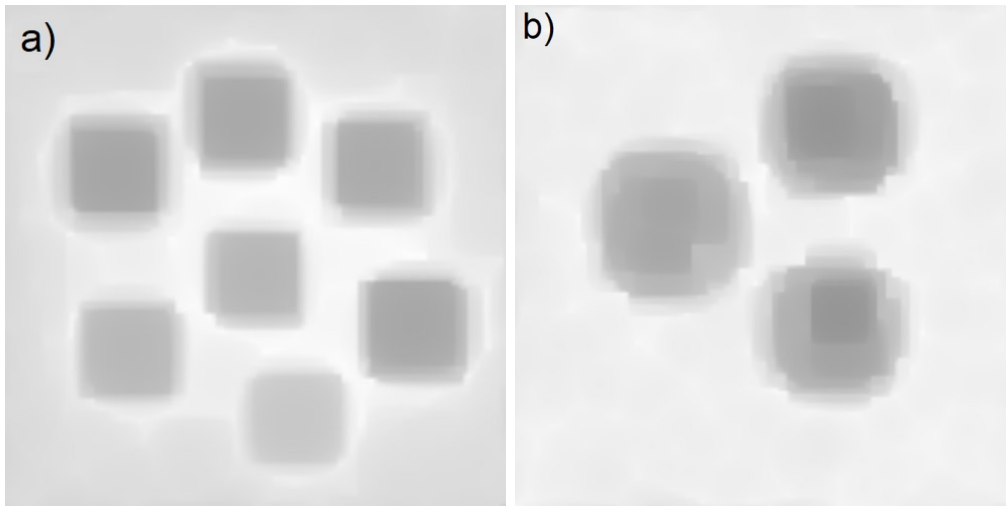


Figure 6.7: Background of the TEM images of bMMG8 (batch method) in part a) and fMMG4 (feeding method) in part b).

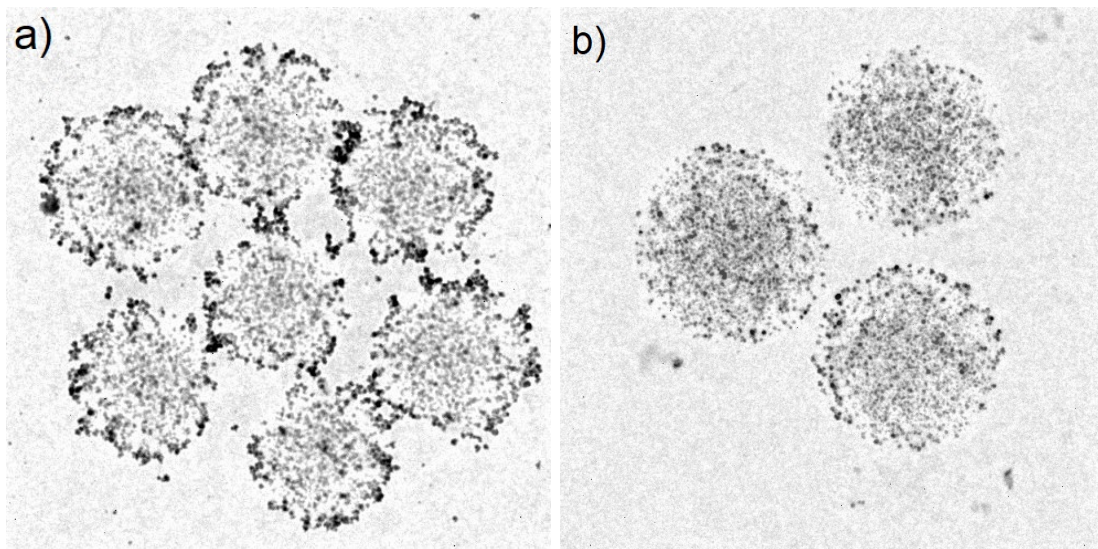


Figure 6.8: TEM images with subtracted background of bMMG8 (batch method) in part a) and fMMG4 (feeding method) in part b).

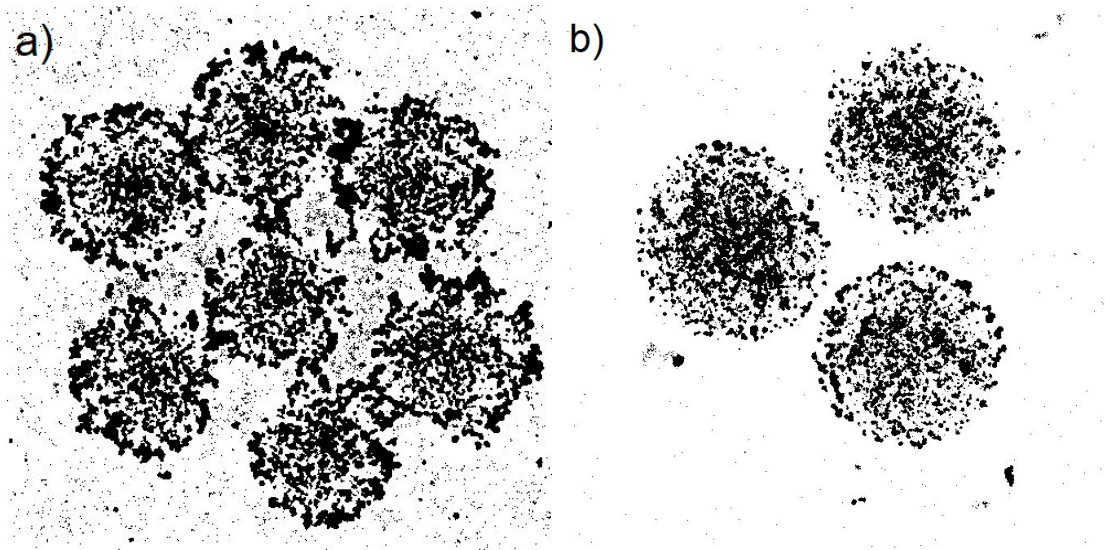


Figure 6.9: Binary map of bMMG8 (batch method) in part a) and fMMG4 (feeding method) in part b).

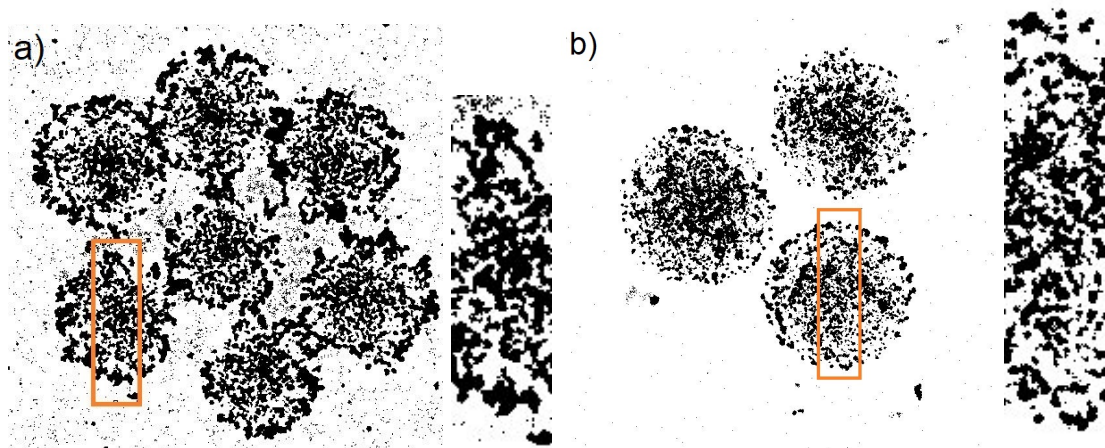


Figure 6.10: Binary map with highlighted area and extracted area. In part a) bMMG8 (batch method) and in part b) fMMG4 (feeding microgel)

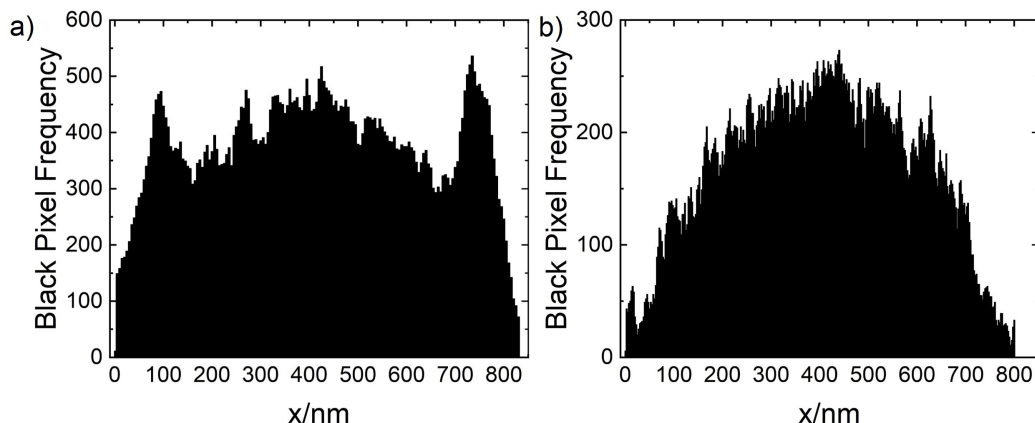


Figure 6.11: Black pixel frequency against the particle size for the magnetic microgels. bMMG8 (batch method) in part a) and fMMG4 (feeding method) in part b).

of monomer is consumed during the polymerization. This is important for the comparison of the two systems (batch and feeding). The shrinking and swelling influences the surface charge density of the microgels. This influence is shown in the temperature dependent EM. The EM confirms the desired positive charge of the microgels. Also the EM studies support the reversible shrinking and swelling during heating and cooling. In the shrunken state the EM is higher than in the swollen state which is explained by rearrangement of the charges towards the surface of the microgels [5], thus a higher surface charge density. Comparing PNIPAM based microgels co-polymerized with AA and pure PNIPAM based microgels the PNIPAM-co-allylamine microgels tend to have a larger hydrodynamic radius due to the internal repulsive force of the positively charged AA. This is already reported in literature [12, 38]. While DLS and EM measurements give similar results for both types of microgels the mechanical properties differ a lot.

#### *Magnetic Microgels (MMG)*

The magnetic microgels are larger compared to the unloaded microgels. This is already shown in *Chapter 4* [101] and is also known for brushes [104]. The increase in size (stretching of the microgel matrix) is explained by: First, the osmotic pressure, due to the increase of ion concentration in the sample. The ions drag water into the microgel. Second, the repulsive interaction between the MNPs and last, the volume of the MNPs itself. The shrinking/swelling behavior of the microgels is preserved after loading with MNPs. The shrinking/swelling is as well reversible for several heating/cooling cycles. After loading the microgels with MNPs the swelling ratio remains more or less the same compared to the pure microgels. Loading the positively charged microgels with negatively charged MNPs leads to a charge reversal at 50 °C. This charge reversal is more pronounced for the homogeneously cross-linked microgel (fMMG4) and is there also detected at 20 °C. The similar EM for the MGs and the difference in EM for the MMGs

is a strong hint that more MNPs are embedded into the homogeneously cross-linked microgel (fMMG4). This is supported by the increase in hydrodynamic radii which is much more pronounced for the homogeneously cross-linked magnetic microgel (fMMG4). The higher loading with MNPs leads to the conclusion that MNPs penetrate deeper into the microgel since the core is less dense cross-linked than for the heterogeneously cross-linked bMG8. This is supported by TEM images.

The TEM images show that the MNP distribution inside the two types of microgels (batch and feeding) are different. The MNP distribution for bMMG8 (batch method) shows a more constant black pixel frequency compared to the fMMG4 (feeding method). The rather flat 2D projection of the MNP distribution for bMMG8 is a result of a core/shell distribution of the MNPs. The electron beam passes the same amount of MNPs at all places, which means that there are less particles per probed volume in the core of the microgel than in the shell. For bMMG8 the MNPs are distributed in the shell of the core/shell structured microgel. Furthermore the higher number of black pixels at the ends of the histogram support the core/shell structure. This was already shown for gold nanoparticle by Gawlitza *et al.* [57] and Gelissen *et al.* [14]. Gelissen *et al.* also showed the ideal core/shell assembly and the corresponding nanoparticle distribution in such a histogram. The distribution of MNP in fMMG4 is homogeneous. The parabolic distribution of the 2D projection of the MNP distribution inside the microgels is the direct consequence of the homogeneously distributed MNPs. The black pixel frequency for ideal homogeneously distributed MNPs would be also parabolic. The observed MNP distribution is therefore close to ideal. The observed core/shell arrangement of the MNPs inside the microgel network supports the different cross-linker distributions inside the microgels. The highly cross-linked core of the batch microgel (bMG8) has a small mesh size and therefore sterically hinders the MNPs to penetrate deeper into the microgel network. For the feeding microgel (fMG4), this is not the case and the constant cross-linker density results in a constant mesh size. Thus allowing the MNPs to penetrate through the whole microgel particle. The pixel resolution of 2.5 nm per pixel is suitable to determine the MNP distribution in the microgel. The resolution of the TEM image is 5 times the average MNP size. Some drawbacks of the 2D images from 3D soft polymer microgels in high vacuum are to be kept in mind. Due to the high vacuum, the microgels are in a dried state adsorbed onto the surface and therefore flattened. This effect becomes more pronounced with softer microgel (less cross-linker). The used TEM techniques are not suitable to resolve or analyze particles that are laying on top of each other and limits the analysis for highly loaded hybrid systems.

The number of MNPs embedded into the microgel is significantly higher compared to the study in *Chapter 4*. In the presented study the MNPs are stabilized with citric acid and have a core diameter of around 12 nm while in *Chapter 4* [101] used Polyacrylic Acid (PAA) for the MNP stabilization and had a particle diameter of 15 nm. The zeta potential of the MNP@CA is lower ( $-56.9$  mV) compared to the MNP@PAA ( $-70$  mV). The bare magnetic nanoparticles are similar, but the PAA shell is much larger compared to the citrate shell. Therefore MNP@PAA are more sterically hindered, while the electrostatic attraction is increased.

## 6.5 Conclusion

The present study shows the influence of the inner microgel (MG) structure on the MNP distribution for positively charged microgels and oppositely charged magnetic nanoparticles (MNPs). Therefore, two synthesis strategies (batch and feeding) are realized. The batch method leads to a heterogeneously cross-linked structure of the microgel and the feeding method leads to homogeneously cross-linked structure. This was proven by AFM indentation experiments and supported by TEM images. The microgels synthesized with the batch method show a decreasing elastic modulus from the microgel center towards the outer shell, while the elastic modulus is constant across the whole microgel synthesized with the feeding method. The feeding method compensates successfully the different reaction kinetics of the used monomers, cross-linker and co-monomer. The difference in internal structure leads to different distributions of the MNPs. They are rather located in the outer shell of heterogeneous microgels and can enter more deeply into the core of homogeneously cross-linked microgels. The total amount of MNPs is higher in homogeneously cross-linked microgels leading to a stronger increase in size of the microgel than for the heterogeneous one. Both species of positively charged microgels exhibit a charge reversal during loading with negatively charged MNPs. A high loading with MNPs was achieved while preserving the microgel properties such as the reversible swelling and shrinking due to temperature cycling. A multi-responsive microgel that exhibit the VPT was designed. It could further be shown that the mesh size is a key parameter for embedding MNPs into the microgel. Homogeneously cross-linked microgels are interesting for future applications due to the higher loading with nanoparticles and the homogeneous distribution of the particles leading to a bigger "active" volume. This opens up future applications in drug delivery systems where the magnetic microgels act as a carrier system and can be guided by external magnetic fields. Furthermore, the magnetic microgels can be adsorbed at surfaces and work as haptic sensors in external magnetic fields.

# 7 Magnetic Response of $CoFe_2O_4$ Nanoparticles Confined in Microgel Meshes

This study was performed in collaboration with the workgroup of Prof. Wende at the University of Duisburg/Essen. The magnetic measurements and analysis at the superconducting quantum interference device (SQUID) were performed by Joachim Landers, Soma Salamon and Juri Kopp in Duisburg. The magnetic nanoparticles were synthesized by Stephan Hinrichs. This study is to be published in the journal *Soft Matter* by Marcus U. Witt, Joachim Landers, Stephan Hinrichs, Soma Salamon, Juri Kopp, Birgit Hankiewicz, Heiko Wende and Regine v. Klitzing.

## 7.1 Abstract

The chapter addresses the coupling of magnetic nanoparticles (MNPs) to the polymer matrix of temperature-sensitive microgels and their response to magnetic fields. Therefore,  $CoFe_2O_4@CA$  (CA= citric acid) NPs are embedded within *N*-isopropylacrylamid (NIPAM) based microgels. The resulting magnetic microgels and the respective pure microgels are analyzed by dynamic light scattering and measurements of the electrophoretic mobility. Furthermore, the interaction between the MNPs and the microgel network is studied via magnetometry and AC-susceptometry using a superconducting quantum interference device (SQUID). The performed experiments show that by crossing the volume phase transition temperature (VPTT) the magnetic properties of the system change dramatically. These changes are related to the confinement of the MNPs inside the microgel network. Modification of the microgel by co-polymerization of hydrophobic allylmercaptan (AM) shows a pronounced effect on the swelling ability and on the magnetic response, i.e. the coupling of MNPs with the polymer matrix. Additionally, an effective size distribution has been extracted from modeling AC-susceptibility data, representing the different degrees of constraint in MNP rotation and motion in microgel meshes. These findings help to understand the interaction between MNPs and the microgel matrix to design such multi responsive systems with tunable particle matrix coupling strength for future applications.

## 7.2 Introduction

Various realizations are reported on how the polymer matrix binds to the MNPs. Such a system could be realized through MNPs covalently bound to the polymer network [88, 125] or non covalently bound hybrid materials. Such a non covalently bound system is achieved by embedding MNPs into brushes [36] or microgels (see *Chapter 4* and *6*) [16, 81, 101]. In *Chapter 4* the magnetic microgels were analyzed according to their deformability [100, 101] and separability [15, 61, 101]. To the best of my knowledge, there have been no studies on the internal interaction between MNPs and the microgel network. This interaction is a crucial parameter to design multi responsive microgels. Forces acting upon the MNPs are transferred to the polymer matrix, with this transfer being dominated by the interaction between MNPs and polymer matrix. The interaction can be probed by studying the Brownian relaxation of the embedded magnetic nanoparticles, with its frequency determined by the viscosity of the surrounding medium, as long as the particles experience free Brownian motion/rotation. Introducing spatial constraints (the polymer chains) additionally affects the Brownian relaxation. By using thermoresponsive microgels like PNIPAM microgels for embedding the MNPs, the spatial expansion of the microgel meshes can be varied by changing the temperature. Therefore, the interaction between MNPs and the polymer network can be controlled. This work shows the first step to investigate the interaction of the MNPs with the surrounding polymer network. This is realized by looking at the partially quenched magnetic Brownian relaxation of the MNPs embedded into PNIPAM microgels. Furthermore, the influence of a hydrophobic co-monomer (allyl mercaptan) on the microgel properties and the distribution of MNPs embedded into the microgel is shown. The microgel properties are measured with dynamic light scattering and electrophoretic mobility. Magnetometry and AC-susceptibility measurements were used to study the interaction between MNPs and polymer matrix. For this study the following samples were used fMG5 and fMG6 to see the influence of the hydrophobic allyl mercaptan. Additionally, it was expected to increase the interaction strength between MMG and the gold surface. As the thio (-SH) moiety is attracted to gold [87]. The stickiness of the MMGs could not be improved, but this topic will be discussed in more detail in the appendix. For the MG composition see *Table 3.1*.

## 7.3 Results and Discussion

### 7.3.1 Structure of (Magnetic) Microgels

#### Dynamic Light Scattering

The microgels and magnetic microgels show the typical expected temperature responsive behavior. The DLS data are shown in *Figure 7.1 a*). A more detailed view of the first heating/cooling cycle is shown in *Figure 7.2* for the MGs and in *Figure 7.3* for the MMGs.

The VPTT of fMG5 and fMG6 are  $31 \pm 1$  °C and  $28 \pm 1$  °C respectively. The VPTT for

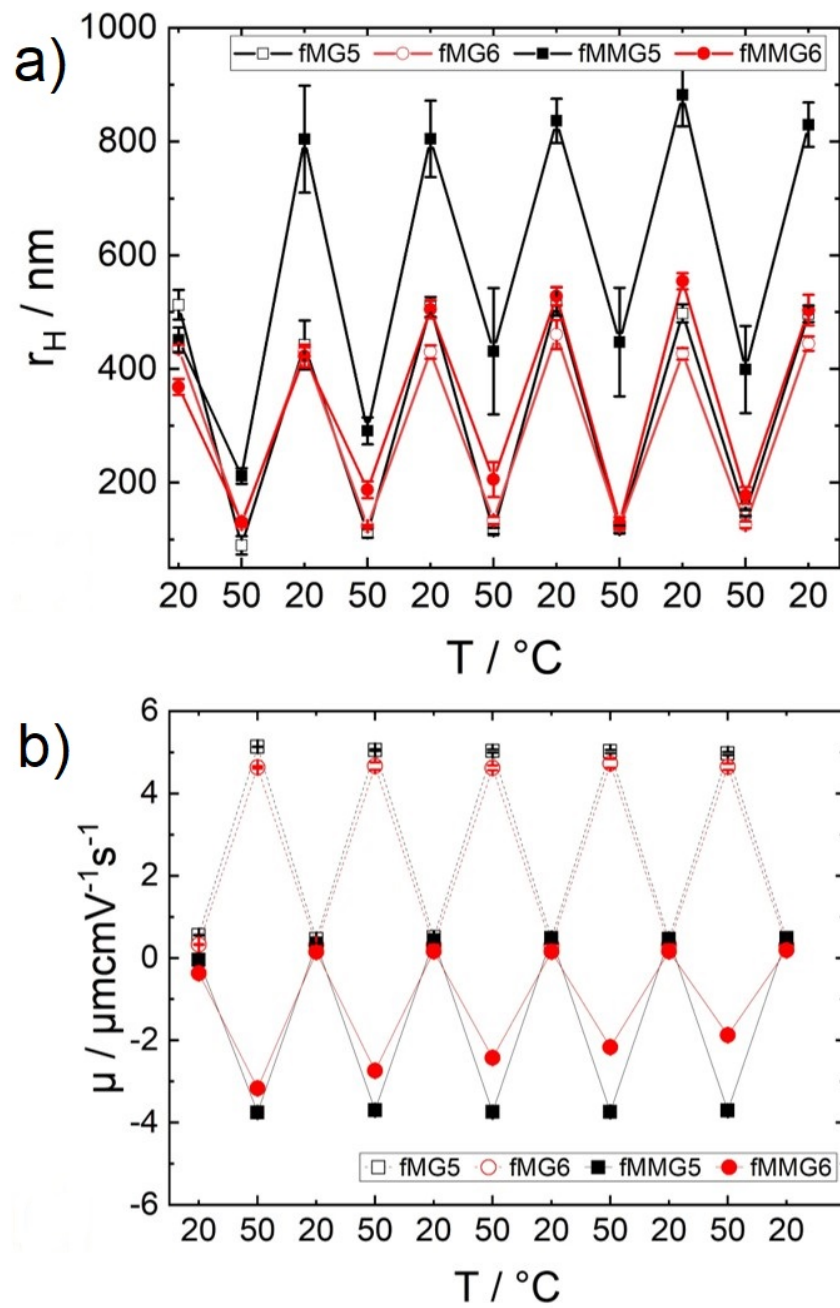


Figure 7.1: a) hydrodynamic radii and b) the electrophoretic mobility plotted against several heating/cooling cycles. The microgels (fMG5 and fMG6) are plotted with open symbols and the magnetic microgels (fMMG5 and fMMG6) are plotted with closed symbols. In b) the error bars are smaller than the symbol size.

fMG5 is in good agreement with the literature, while for fMG6 the VPTT is noticeable lower. This already indicates an influence of the AM on the microgel structure. For fMG5 (fMG6) the hydrodynamic radius decreases from an average of 495 nm (437 nm) to an average of 115 nm (126 nm) by increasing the temperature from 20 °C to 50 °C. The hydrodynamic radius stays constant above a temperature of 40 °C. The VPTT for fMMG5 (fMMG6) is 32.2 °C (30.9 °C respectively). The rise in VPTT for MMGs in comparison to the MGs may be a consequence of the MNP embedding, which increases the energy needed to break the hydrogen bonds inside the network structure or indicates a steric reorientation. Both microgels show a similar size in the shrunken state, thus indicating that the same amount of monomers is built into the microgels. This is supported by the fact that the syntheses are identical until the ninth minute. Small differences are expected due to the addition of AM to fMG6 in the synthesis time between the 9th and 10th minute. This difference becomes more prominent in the swollen state where fMG6 is smaller than fMG5. The size difference as well as the shifted and broadened VPTT of fMG6 might originate from the hydrophobicity due to the addition of AM.

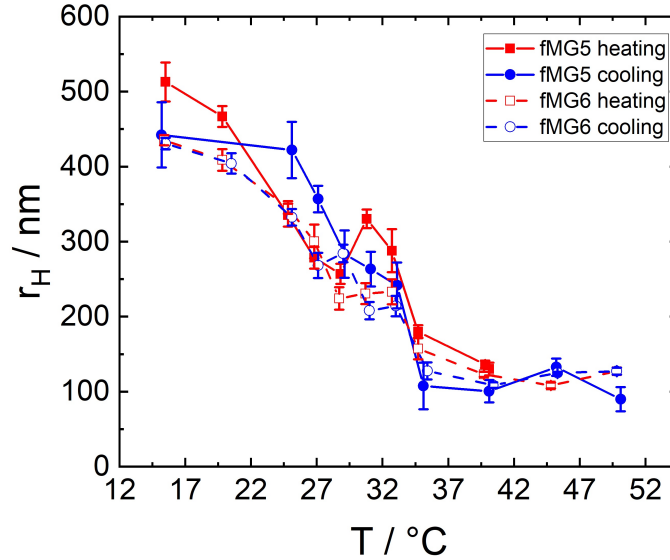


Figure 7.2: Hydrodynamic radius of the synthesized microgels fMG5 (no AM) and fMG6 (with AM) in dependence of the temperature for the first heating and cooling cycle. The MGs show the well known shrinking and swelling behavior with a VPTT close to 32 °C.

In the first temperature cycle the hydrodynamic radii of the magnetic microgels (fMMG5 and fMMG6) is smaller than the ones of the corresponding pure microgels (fMG5 and fMG6) (compare *Figure 7.2* and *Figure 7.3*), while it is larger for all subsequent cycles. The overall trend of a larger size for MMGs compared to the respective MGs is well known in the literature and is originating from the Gibbs-Donnan effect [81,101]. The change in size after the first heating/cooling cycle is more pronounced for fMMG5 compared to fMMG6. This rearranging of the magnetic microgel structure is well known

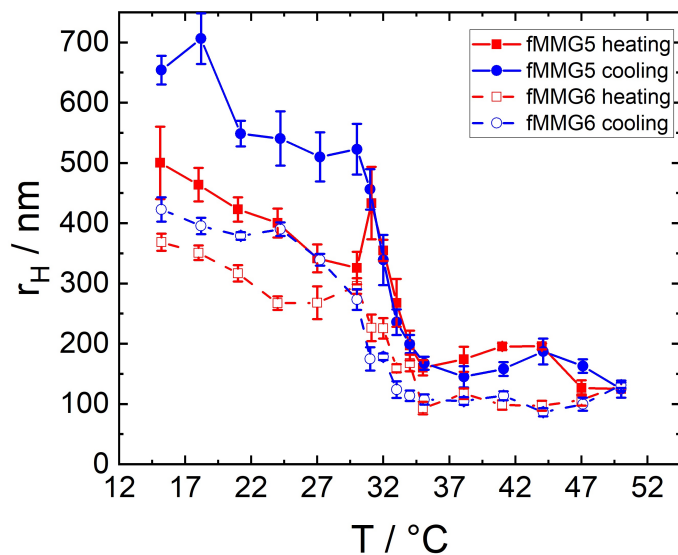


Figure 7.3: Hydrodynamic radius of the magnetic microgels fMMG5 (no AM) and fMMG6 (with AM) in dependence of the temperature for the first heating and cooling cycle. The MMGs show the preserved shrinking and swelling behavior with a VPTT close to 32 °C.

for microgels loaded with MNPs [81,101]. The microgel sizes above and below the VPTT are constant for both MMGs after the first cycle. This shows that the re-arrangement of the internal microgel structure as well as the MNPs position became stable after an initial shrinking/swelling cycle. *Figure 7.1* shows the hydrodynamic radius of the microgels (open symbols) and magnetic microgel (closed symbols) at two different temperatures (20 °C and 50 °C) for several cycles. This graph shows that the shrinking/swelling is completely reversible and reproducible over several cycles.

The change in hydrodynamic radius corresponds to a swelling ratio of  $\alpha = 86.3$  ( $\alpha = 10.1$ ) for fMG5 (fMMG5) and  $\alpha = 41.7$  ( $\alpha = 28.0$ ) for fMG6 (fMMG6) respectively. The ability to swell decreases after loading with MNPs. The hydrodynamic radius and swelling ratio of the two microgels are shown in *Table 7.1* for easier comparison.

### Electrophoretic Mobility

In *Figure 7.1 b*) the electrophoretic mobility (EM) of fMG5 and fMG6 (open symbols) and fMMG5 and fMMG6 (closed symbols) is plotted against several temperature cycles (between 20 °C and 50 °C). Both microgels show a positive charge measured by the (positive) electrophoretic mobility. With rising temperature the surface charge density increases and therefore also the electrophoretic mobility. The change of electrophoretic mobility is reversible and is shown for several heating/cooling cycles. *Table 7.1* shows the average electrophoretic mobility at 20 °C and 50 °C. The positive charge of the MGs originates from the used positively charged reactants in the synthesis. In *Chapter. 6* it is shown that the AA distribution is homogeneous within the microgel [81].

Sample	$r_H^{20\text{ }^\circ\text{C}} / \text{nm}$	$r_H^{50\text{ }^\circ\text{C}} / \text{nm}$	$\alpha$	$\mu^{20\text{ }^\circ\text{C}} / \mu\text{m cm V}^{-1}\text{s}^{-1}$	$\mu^{50\text{ }^\circ\text{C}} / \mu\text{m cm V}^{-1}\text{s}^{-1}$
<i>fMG5</i>	495	115	86.3	0.47	5.04
<i>fMG6</i>	437	126	41.7	0.32	4.66
<i>fMMG5</i>	767	355	10.1	0.44	-3.73
<i>fMMG6</i>	491	161	28.0	0.16	-2.47

Table 7.1: Characteristic measurements of the microgels, mean hydrodynamic radii  $r_H$  and the swelling ratio  $\alpha$  and mean electrophoretic mobility  $\mu$  (@20 °C and @50 °C) .

The magnetic microgels exhibit a reduced electrophoretic mobility compared to the corresponding pure microgels, since the positive charges of the microgel are partially neutralized by the embedded negatively charged MNPs. For both magnetic microgels the electrophoretic mobility becomes negative at 50 °C, where the magnetic microgels exhibit a charge reversal. The change in EM is reversible and reproducible. For fMMG6 the EM seems to decrease linearly with an increasing number of cycles. A detachment of the MNPs is not expected as this would have been visible in the measurements with the DLS. The MMGs are larger in size compared to their MG counterpart. A loss of MNPs would result in a shrinking of the MMGs. The charge reversal observed by crossing the VPTT can be explained by the decreased surface area but constant number of charges provided by the MNPs. Combining these findings with the DLS measurements it can be concluded that the MMGs retain their gel like properties after being loaded with MNPs.

### Transmission Electron Microscopy

*Figure 7.4* displays magnetic microgels, fMMG5 (no AM) shown in part a) and fMMG6 (with AM) in part b) after preparation. The microgels themselves are not visible due to the low electron density and the resulting low TEM contrast. However, their shape and position can easily be inferred from the well visible MNPs arranged in circular patterns. The microgels exhibit different distributions of MNPs: For fMMG5 the MNPs are well separated, with only small clusters being present, while for fMMG6 the MNPs are arranged in small clusters or short chains, respectively. The different MNP arrangement is expected to originate from the AM in fMG6 (fMMG6), because fMG5 shows similar MNP distribution as reported *Chapter 6*. AM reduces the microgel charge and increases the hydrophobicity. This may lead to an increased MNP aggregation.

## 7.3.2 Magnetic Properties

### Magnetometry

In *Figure 7.5* the magnetization of the magnetic microgels is plotted against the temperature. Both samples show qualitatively similar behavior, with the overall magnetization of fMMG6 being two to three times smaller compared to fMMG5. Minor differences in the concentration of magnetic material in the different microgel samples are possible. The variations in the maximum magnetization reached in the ZFC-FC measurements

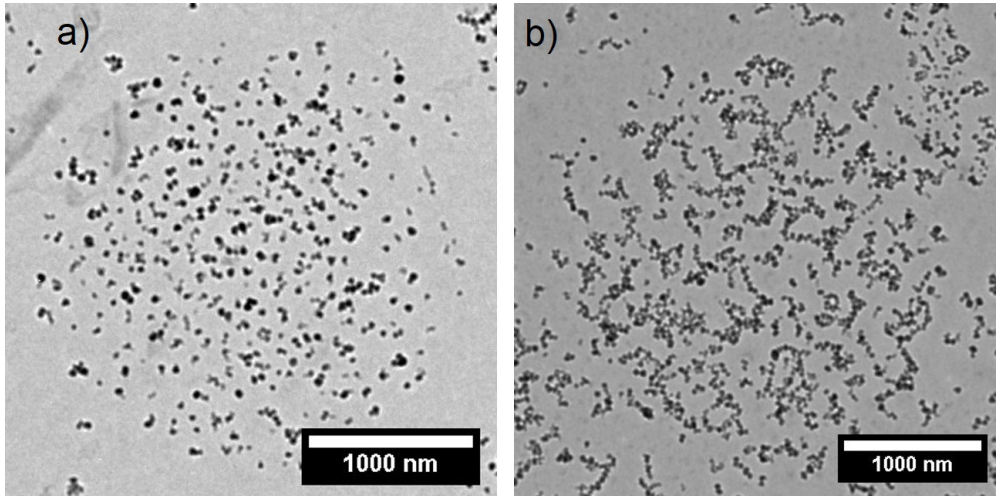


Figure 7.4: TEM images of the magnetic microgels. a) shows the fMMG5 (no AM) and b) shows the fMMG6 (with AM). The MNPs are arranged in a circular pattern, reproducing the shape of the microgel particles they are embedded in.

can most likely be explained by a different number of magnetic nanoparticles reaching the completely superparamagnetic state. Therefore, the difference in amplitude of  $m_{ZFC}$  may be a result of the difference in MNP distribution inside the microgels. The lower amplitude for fMMG6 compared to fMMG5 could indicate the presence of agglomerates, also observed in the TEM images, as they seem to be more resilient to the applied magnetic field. In the magnetic agglomerates the resulting magnetic moment is reduced due to partial cancellation of their magnetic moments. In the temperature range between  $-173$  °C and about  $0$  °C the splitting between the ZFC- and FC- magnetization branch ( $m_{ZFC}$ ,  $m_{FC}$ ) decreases moderately. This reflects the minor fraction of small  $\text{CoFe}_2\text{O}_4$  nanoparticles experiencing sufficiently fast Néel-type superparamagnetic relaxation at such low temperatures, thus allowing the dynamic realignment of the individual particle's magnetic moment. A first fast increase in the ZFC-magnetization close to the water melting point is easily explained by the onset of Brownian particle motion. This permits the partial alignment of larger particles along field direction still blocked in terms of Néel relaxation. A second, less pronounced increase in  $m_{ZFC}$  is visible at higher temperatures, possibly originating from faster microgel particle rotation close to the VPTT, crossing the timescale of the magnetization measurement. Sample fMMG5 shows no splitting of the ZFC- and FC- branch above the VPTT of the microgels, indicating that a complete superparamagnetic state is reached with no further change in particle dynamics. The magnetization curves of fMMG6 on the other hand are split up to the maximum measurement temperature, revealing an ongoing magnetic relaxation even at temperatures clearly above the VPTT, as also visible at  $40$  °C when switching from heating to cooling by the time-dependent increase in magnetization. The latter indicates a fraction of magnetic nanoparticles or microgel particles, respectively, which are

still magnetically blocked on the timescale of the experiment. As is later on illustrated in detail in terms of AC-susceptometry, the different behavior close to the VPTT could be explained by a higher mobility of MNPs in the wider PNIPAM microgel meshes in fMMG5 compared to fMMG6. That would be in agreement with the moderately higher water uptake of this microgel as pointed out by its higher swelling ratio. This is further supported by the findings of the TEM images showing lower inclination for clusters to manifest in sample fMMG5 as compared to fMMG6. On the contrary, MNPs in fMMG6 only display completely superparamagnetic behavior in case of sufficiently fast microgel particle rotation. This can be assumed, as their trapped state in the gel meshes should not allow spatial reorientation of individual magnetic nanoparticles and small MNP clusters. *Figure 7.5 b)* shows a close-up of the high-temperature region for both samples. A rapid decrease in  $m_{ZFC}$  can be seen above 34 °C for both samples, expected to correspond to the VPTT of the MMGs, both being slightly higher as compared to DLS measurements. The higher VPTT found here in magnetization measurements relative to those from DLS may be a result of the different experimental setup and measurement principles.

In the FC branch of the measurement, both samples display a spontaneous drop in  $m_{FC}$  at about  $-18$  °C, where the sample is undergoing the transition from the supercooled liquid to the solid state. This phenomenon has recently been discussed for ferrofluids based on polyethylene (PEG)-solutions. It was assigned to torques acting on individual nanoparticles during the phase separation (crystallization) process. These may originate either from enhanced interparticular magnetic interaction within the remaining fluid volume or mechanical or hydrodynamic interaction with forming ice-crystal structures [110].

### Temperature Dependent AC-Susceptibility

To gather closer information on temperature dependent relaxation dynamics of individual MNPs and the magnetic microgel particles, magnetic AC-susceptometry measurements were performed at temperatures of 0 – 50 °C. Results are shown exemplarily in *Figure 7.6* for 20 °C.

To ensure easier comparability of particle dynamics in both microgel systems, the magnetic susceptibility is normalized with respect to the highest value. One can observe a dominant peak in the imaginary part of the magnetic susceptibility  $\chi''$  close to 1 Hz, being more pronounced for fMMG6 than for fMMG5. A minor broad susceptibility component stretches up to maximum attainable frequencies of about 1.5 kHz, showing higher intensity and an increase upon rising frequency for sample fMMG5. Solid lines in *Figure 7.6* are from theoretical modeling of the experimental data points. Here, an extended Debye model was used, describing the distribution of Brownian- and Néel-type relaxation times ( $\tau_B$ ,  $\tau_N$ ) for an ensemble of magnetic nanoparticles, as defined in *Eq. 7.1* and *Eq. 7.2*:

$$\tau_B = \frac{4\pi\eta r_H^3}{k_B T} \quad (7.1)$$

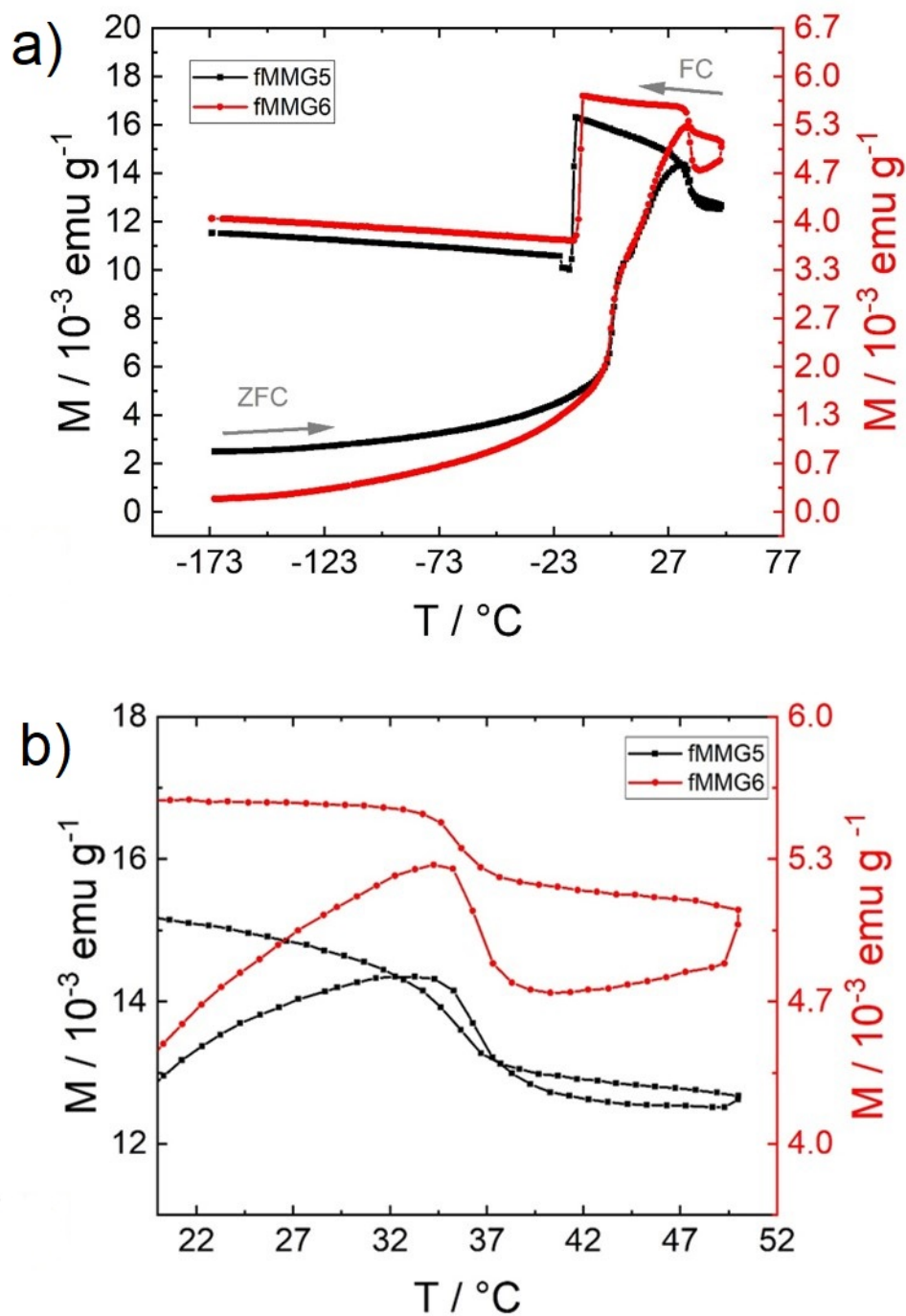


Figure 7.5: ZFC-FC magnetization curves of fMMG5 (black) and fMMG6 (red) recorded from  $-173$  to  $50$   $^\circ\text{C}$  in an external magnetic field of  $10$  mT. In a) the complete temperature range is plotted while in b) the temperature range is focused around the VPTT from  $20$  to  $50$   $^\circ\text{C}$ . To keep the graph clear, the error bars have been omitted.

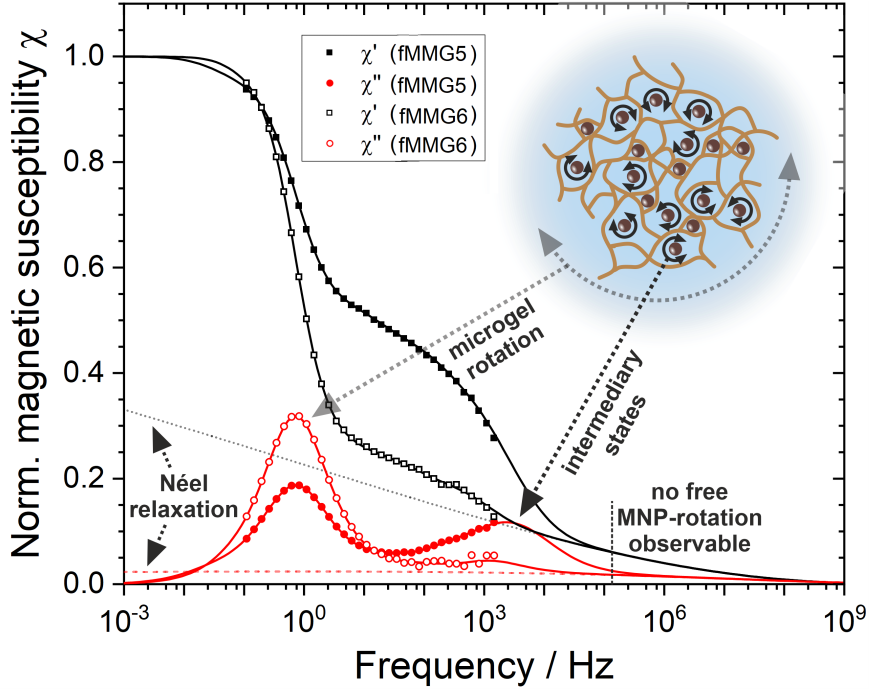


Figure 7.6: Magnetic susceptibilities  $\chi$  of fMMG5 (filled) and fMMG6 (open symbols) recorded at 20 °C. Data points were theoretically reproduced via a phenomenological model as described in the text (solid lines). Frequency regions are labeled with regard to their predominant relaxation mechanism as illustrated by the schematic structure of a microgel particle, showing contributions of free as well as trapped magnetic nanoparticles: microgel rotation ( $\sim 1$  Hz), intermediary states ( $1 \text{ Hz} < f < 100 \text{ kHz}$ ), free nanoparticle rotation at ca. 120 kHz (not observed), and Néel relaxation (background signal, visible at  $f > 100 \text{ kHz}$ ). For comparison, the Néel-type background signal ( $\chi'$  grey dotted,  $\chi''$  red dashed) was added as simulated for identical relaxation parameters in absence of Brownian motion. To keep the graph clear, the error bars have been omitted.

$$\tau_N = \tau_0 \exp\left(\frac{K_{eff}V_c}{k_B T}\right). \quad (7.2)$$

Here  $k_B T$  is the thermal energy,  $\eta$  the dynamic viscosity of the solvent surrounding the MNPs,  $\tau_0$  a relaxation factor for magnetic nanoparticles often assumed to be in the range of  $10^{-9}$  to  $10^{-13}$  s [107], which is fixed to  $\tau_0 = 1$  ps,  $K_{eff}$  the effective magnetic anisotropy energy density and  $V_c$  the particle core volume. The utilized model is similar to that described by Hankiewicz neé Fischer et al. [20]. In the present study a log-normal distribution is used with a core diameters of  $d_C = 12.2 \pm 3.2$  nm, as determined for the

spherical cobalt ferrite (CFO) NPs without citrate shell via TEM analysis. However, up to this point we lack an adequate theoretical model to describe the complex AC-susceptibility signal structure of MNPs experiencing varying degrees of confinement. Depending on the microgel mesh size, one would expect the MNPs e.g. to perform free rotation in wider meshes and dampened or decelerated rotation in meshes of intermediate size, due to repeated contact with the surrounding polymer strings. When trapped in even narrower spaces, i.e. meshes of minimum size close to the MNP diameter or in the collapsed PNIPAM microgel state, spatial realignment of the particles should not longer be possible.

Therefore, the following phenomenological model is applied to reproduce the Brownian contributions to the magnetic susceptibility signal: To describe different degrees of particle confinement, core-shell nanoparticles are modeled, with core diameters as described above and a free distribution of non-magnetic shell thicknesses. The particle is assumed to move through water, with the temperature-dependent variation in water viscosity being considered by using literature values of  $\eta_{H_2O}(T)$  [52]. Here a minimum total particle hydrodynamic diameter  $d_H$  of 15 nm (CFO-core plus citrate coating) represents contributions of free MNP rotation in water. Higher effective hydrodynamic diameters correspond to slower Brownian rotation, representing higher degrees of spatial particle confinement, where the friction acting on the rotating MNPs is increased. The maximum values of  $d_H$  are thus expected for narrow microgel pores, where trapped MNPs can only add to the magnetic susceptibility signal by the rotation of the whole microgel particle they are embedded in. The upper end of the distribution  $P(d_H)$  thereby labels the microgel particle diameter. Alternatively, as discussed in more detail below, the simulation results can be understood as distributions of effective viscosities of the medium the MNPs are moving in. Thereby a fixed value of  $d_H = 15$  nm is assumed, corresponding to identical values of  $\eta \cdot d_H^3$ , i.e. identical distributions of relaxation times. The latter interpretation may be more intuitive to describe hindered MNP motion when coming from soft matter dynamics. As can be seen below, this model can successfully reproduce experimental AC-susceptometry data, while being limited to the above-mentioned effective parameters, as interaction between MNPs and the local environment are not considered explicitly.

The magnetic nanoparticles which are completely mechanically blocked by their surrounding only contribute to the susceptibility via rotation of the whole microgel particle. The low-frequency peak in  $\chi''$  in *Figure 7.6* at about 1 Hz can easily be assigned to microgel particle rotation using *Equation 7.1*. Therefore, it will contribute at a rotation frequency corresponding to the hydrodynamic microgel diameter dependent on the specific sample and measurement temperature. On the contrary, free rotation of the MNPs in large microgel pores assuming a hydrodynamic diameter  $d_H$  of about 15 nm and a viscosity of water of  $\eta(20^\circ \text{C}) \approx 1$  mP, would translate to a Brownian rotation frequency of about 120 kHz. This frequency is not directly observable in the attainable frequency range here. However, the absence of free MNPs can be inferred for both samples from the low value of  $\chi'$  at about 1 kHz. Contributions in the intermediate frequency range of about  $1 \text{ Hz} < f < 10^5 \text{ Hz}$  are assigned to different states of particle confinement, which will be discussed in the next paragraph in detail, concerning temperature dependent

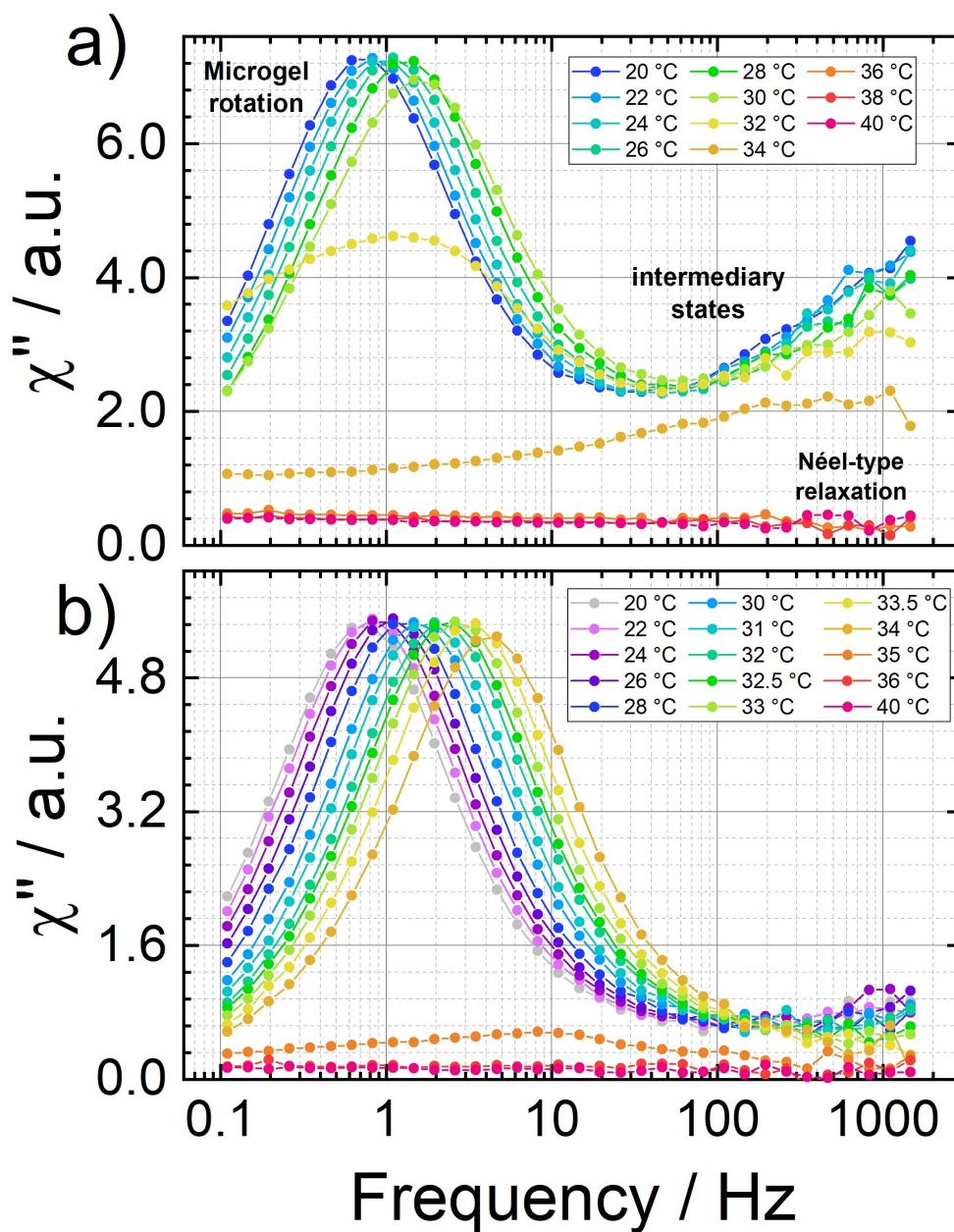


Figure 7.7: Magnetic susceptibility data of fMMG5 (a) and fMMG6 (b) recorded at 20 – 40 °C. The enhanced high-frequency component in fMMG5 is clearly visible, representing partially free MNP rotation, as well as the shift in the microgel rotation signal to higher frequencies when approaching the VPTT. To keep the graph clear, the error bars have been omitted.

variations in the MMG diameter.

In addition to Brownian contributions one can also analyze to some extent the frequency dependent Néel relaxation of the particles. This can be done based on the susceptograms taken above the VPTT at about  $34^{\circ}\text{C}$  as shown in *Figure 7.8*. For sake of comparison, the pure Néel-type signal is also displayed in *Figure 7.6* (grey and red) as it would appear in absence of any Brownian processes. The signal is being calculated for identical parameters  $\tau_0$  and  $K_{eff}$  as in the complete model stated below. Information on the magnetic anisotropy energy barrier of the nanoparticles can be extracted from the remaining Néel susceptibility signal, stretching almost constantly over several orders in frequency due to the exponential dependence on the magnetic anisotropy energy. The ratio of  $\chi'$  to  $\chi''$  in the measured frequency interval can be reproduced well using values of  $\tau_0 \sim 10^{-12}$  s and  $K_{eff} \sim 70$  kJ/m<sup>3</sup>. As expected, the CFO MNPs display a relatively high magnetic anisotropy energy density compared to other ferrite nanoparticles. As illustrated by Cannas et al., the magnetic anisotropy for such particles does not only depend on their size, but also strongly on the Co<sup>2+</sup> site occupation in the spinel lattice. That depends on the degree of structural order as well as on the particle preparation approach [24].

By doing so the amplitude of the Néel relaxation background in the intermediate frequency region is known, which is necessary for the correct simulation of the dominant Brownian contribution. It becomes evident that the difference between fMMG5 and fMMG6 in partially free MNP motion assigned to susceptibility contributions in the range of ca. 1 kHz is even more pronounced. It can therefore be concluded that sample fMMG5 has a much lower degree of constraint in mobility as analyzed below for varying temperatures.

*Figure 7.6* demonstrates that it is easier to identify the contributions of different relaxation mechanisms via the Debye-peak features in  $\chi''$  as compared to  $\chi'$ . Therefore, *Figure 7.7* displays  $\chi''$  for fMMG5 and fMMG6 recorded upon rising temperature between  $20^{\circ}\text{C}$  and  $40^{\circ}\text{C}$ . This is providing information on effects on both primary Brownian contributions - microgel rotation and (partially) free MNP rotation - across the VPTT-region. The signal does not change above  $40^{\circ}\text{C}$  (*Figure 7.8*). *Figure 7.7 a*) depicts a shift of the low-frequency microgel rotation peak to higher frequencies for fMMG5. The peak shift is in agreement with shorter Brownian rotation times being expected for decreasing microgel hydrodynamic diameters and viscosity when approaching the VPTT. The peak distinctly broadens at around  $32^{\circ}\text{C}$  and is no longer visible as a distinguishable feature above the VPTT. In sample fMMG5 the signal at about 1 kHz is assigned to partially dampened rotation of MNPs, located in microgel pores of intermediate size.

The lack of further change in the susceptibility signal above  $34^{\circ}\text{C}$  indicates Néel relaxation to be the primary magnetic relaxation process remaining above the VPTT. It is not completely clear, why no signal corresponding to the rotation of the "collapsed" MMGs is visible at/above the VPTT. Based on the radius as shown in *Figure 7.3*, these should exhibit rotational frequencies of about  $10^2$  Hz. This frequencies are well observable with the used measurement setup. A possible explanation is a higher tendency of the PNIPAM particles to agglomerate at these temperatures on the timescale of hours. That would be comparable to the timescale of the measurement of  $\chi(f)$  at an individual

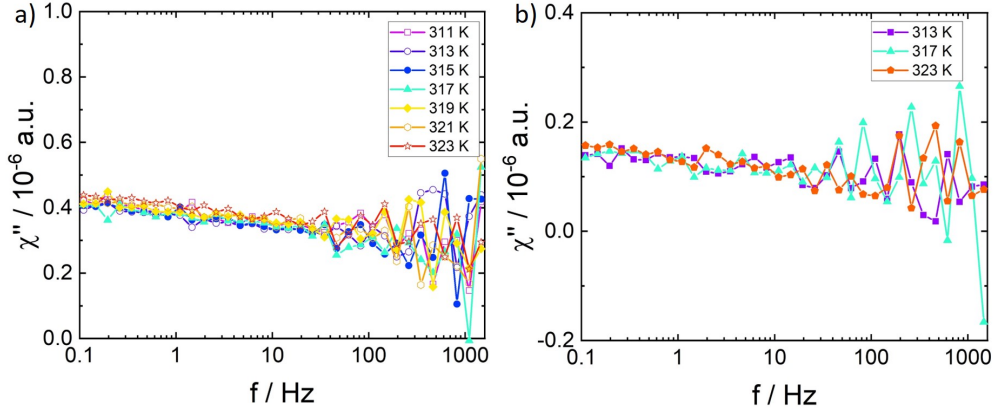


Figure 7.8: AC susceptibility measurements of fMMG5 in part a) and fMMG6 in part b).  $\chi''$  is plotted against the AC excitation frequency for temperatures between 40 °C and 50 °C. The AC susceptibility measurements above 40 °C show no distinctive peak. For fully collapsed MMGs the peak is expected to be at  $\approx 10$  Hz. Above 40 °C the signal amplitude for fMMG5 is 15 times smaller and for fMMG6 it is 24 times smaller than for below 40 °C.

temperature. Agglomeration may be favored due to the microgel particles' much higher effective density in the collapsed state. However, this could not be observed in time-dependent UV/Vis absorption experiments. They were conducted at 20 °C as well as at 50 °C, showing no considerable decrease in sample stability at high temperatures. The measured integrated absorbance remained constant ( $0.288 \pm 0.001$  before heating and  $0.297 \pm 0.002$  after heating).

In general, sample fMMG6 exhibits similar behavior, showing a clear temperature dependent shift of the microgel rotation peak up to about 34 °C (*Figure 7.7 b*). Similar to fMMG5 the AC-susceptibility measurements show a much lower signal contribution assigned to free or partially free MNPs. The different modes of the particle mobility will be analyzed in the next paragraph. The spacial confinement of the MNPs is now analyzed in more detail.

*Figure 7.9* shows the distribution of effective diameters ( $P(d_{eff})$ ) and the distribution of effective viscosity ( $P(\eta_{eff})$ ). Part (a) of *Figure 7.9* shows sample fMMG5 and (b) shows fMMG6. The values  $d_{eff}$  and  $\eta_{eff}$  are calculated as described above in *Equation 7.1*, assuming constant values of  $\eta \cdot d_H^3$  for each given temperature. When discussing the thus extracted distributions, the limitations of this approach have to be kept in mind. For example the maximum and minimum frequencies measurable by the utilized AC-susceptometer are 1500 Hz and 0.1 Hz. These correspond to Brownian rotation timescales for effective particle diameters  $D_{eff} \approx 1600$  nm - 65 nm (or, alternatively for 15 nm MNPs in a medium of  $\eta_{eff} \approx 0.08$  Pas -  $10^3$  Pas).

While the contributions of small particles at high frequencies can be extrapolated to some extent from the trend in  $\chi'$  in the high-frequency range close to 1 kHz, no information on particles much larger than 1600 nm is contained in the data. Also, the chosen

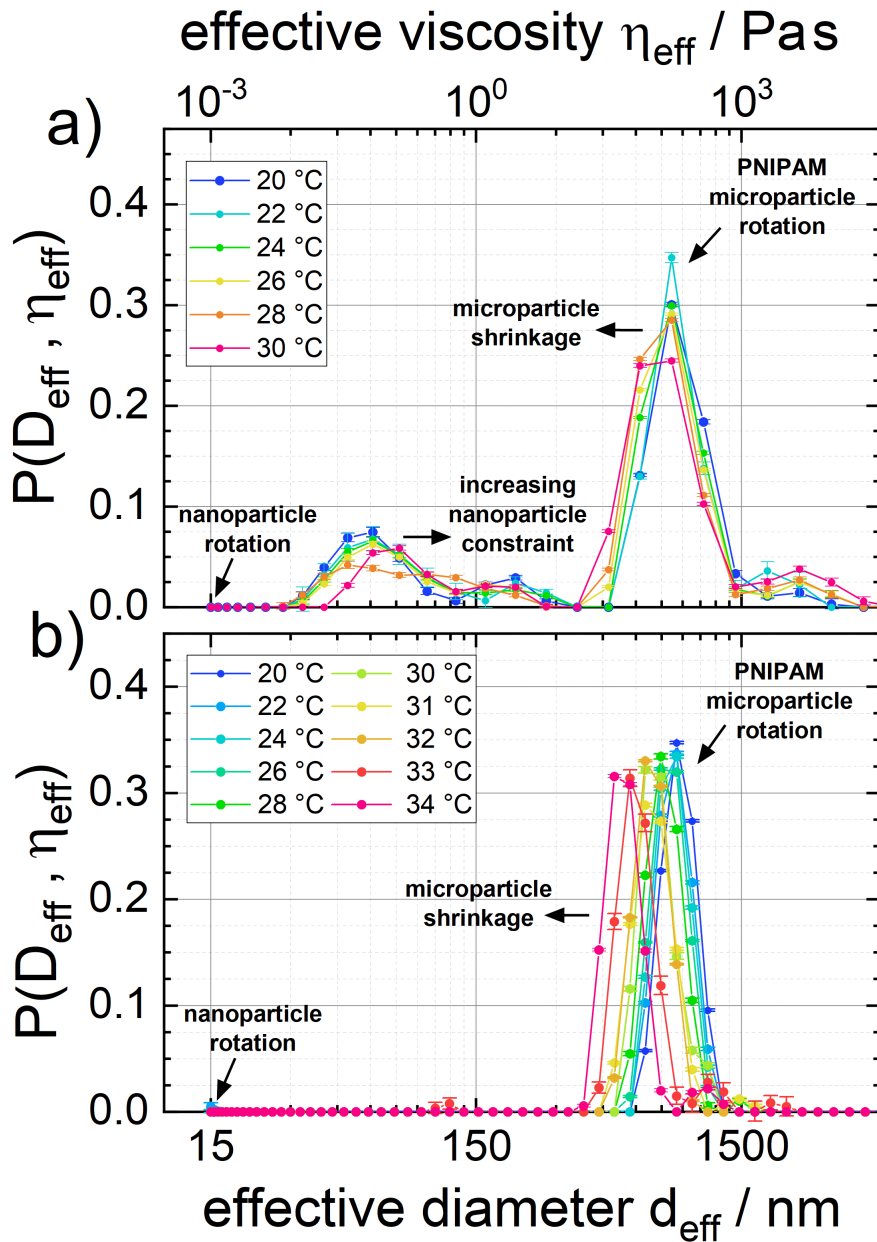


Figure 7.9: Distributions of effective particle diameters and dynamics viscosities extracted from the modeling of rotational frequencies as determined from AC-susceptometry measurements of sample fMMG5 (a) and fMMG6 (b). Different signal distributions and noise levels have been evaluated and taken into account by choosing different numbers of sampling points of 30 (a) and 60 (b) in the  $d_{\text{eff}}$  - interval of 15 nm to 5000 nm, corresponding to MNP motion in dynamic viscosities of  $\eta_{\text{eff}} \approx 1$  mPas to  $4 \cdot 10^4$  Pas.

number  $n$  of the distributions' sampling points as well as the smoothing factor  $\lambda$  applied to  $P(d_{eff})$  have some effect on the fine structure of the resulting distribution. However, as TEM and DLS results indicate that most of the microgels are of about 800 nm in diameter and since the low relative value of  $\chi'(1.5 \text{ kHz})$  points to a negligible number of freely rotating MNPs assuming a continuous distribution  $P(d_{eff})$ , these limitations do not obstruct the analysis in terms of microgel rotation and partially free (intermediary) MNP states.

All this considered, both microgel samples do not display high-frequency free rotation of individual MNPs, which could have been registered via enhanced values of  $\chi'(1.5 \text{ kHz})$ , despite being outside the directly accessible frequency range in a strict sense. This reveals the limited freedom for nanoparticle motion within the microgel pores even down to room temperature. Both samples display a similar position of the primary microgel peak, being slightly broader for fMMG5. Here, a small contribution of larger microgels is indicated in  $P(d_{eff})$ , which could explain the higher average hydrodynamic diameter determined via DLS for fMMG5. At the same time, a considerable amount of intermediary diameters is present, assumed to represent partially constrained MNP rotation. This could presumably be explained by the higher average microgel diameter caused by moderately higher swelling compared to fMMG6, leading to an expansion of the microgel pores and more space for the MNP rotation. fMMG6 on the other hand (*Figure 7.9 (b)*), only exhibits the main microgel particle rotation, allowing for a more precise determination of temperature-dependent size variation: For fMMG5 between 20 °C and 30 °C, the main signal shifts from about 900 nm to 700 nm and for fMMG6 between 20 °C and 34 °C from 850 nm to 530 nm. These effective diameters are in good agreement with the general trends and for fMMG6 also with absolute diameters from DLS, as shown in *Figure 7.3*. A further dampening of (partially) free MNP dynamics in fMMG6 may be introduced by slightly larger MNP structures as evident in TEM images. The size of fMMG6 determined with ACS and DLS can be compared in more detail in *Figure 7.10*, where the hydrodynamic radius is plotted against the temperature. The hydrodynamic radius  $r_H(ACS)$  is extracted by fitting a Gaussian profile to the effective diameter peaks.

One final observation for fMMG5 is worth mentioning: The low-frequency contribution representing partially limited MNP dynamics starts to decrease and shift slightly to higher frequencies at about  $\approx 27 \text{ °C}$  as visible in *Figure 7.7 a*). When approaching the VPTT, the temperature-dependent increase in effective diameter (or effective viscosity, vice versa) accelerates. This could be ascribed to the reduction in microgel pore size, which accompanies the general shrinking of the microgel particle. This results in further constraint of the MNP rotational dynamics and is therefore shifting the contributions into the microgel rotation, which previously were part of the intermediary states (partially constrained MNP dynamics).

While up to this point the extracted distributions of effective parameters were interpreted in terms of MNP mobility, a direct assignment to the number of MNPs exposed to a specific degree of confinement from those distributions is hindered due to uncertainties regarding the microgels' internal magnetic structure. With a core diameter of about 12 nm, the MNPs carry a considerable net magnetic moment ( $\mu_{MNP}$ ), leading to strong magnetic dipole interaction when being in close distance, explaining the minor tendency

to form agglomerates even within the microgel particle structures (see *Figure 7.4*). Therefore, it is unclear whether interparticle interaction will lead to some degree of alignment of easy magnetic directions, when embedding adjacent nanoparticles in the microgel or during the formation of minor MNP clusters. This essentially determines what fraction of MNP magnetic moments cancels each other out, and which remains to contribute to the microgel's net magnetic moment, i.e. to the magnetic susceptibility signal.

Assuming an array of  $N$  more or less aligned MNPs within a microgel particle, the latter will exhibit a net magnetic moment ( $\mu_{MG}$ ) approximately given by the sum of nanoparticle superspins ( $\mu_{MG} \sim N \cdot \mu_{MNP}$ ). However, magnetic moments of  $N$  MNPs completely uncorrelated in terms of easy magnetic direction will partially cancel each other out. This will strongly reduce the microgel particle net magnetic moment ( $\mu_{MG} \sim \sqrt{N} \cdot \mu_{MNP}$ ), as is sometimes observed in magnetic nanoparticle agglomerates [35, 53]. Thereby, the distribution extracted from the phenomenological model cannot be converted easily into a number distribution of MNPs in a specific state of confinement. For this, further knowledge about the microgels' magnetic structure including nanoparticle interaction effects and nanoparticle rheology would be required. A more sophisticated analysis taking these effects into account is planned after a more detailed study of the internal magnetic structure of the microgels via a combination of neutron scattering with remanent magnetometry experiments.

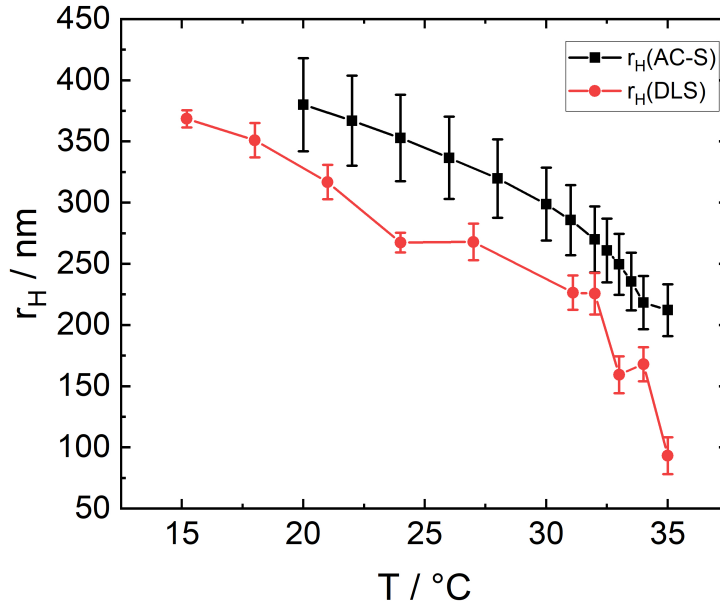


Figure 7.10: The hydrodynamic radius for fMMG6 is plotted against the temperature. In black are the simulated sizes (extracted via a Gaussian fit from effective diameters) from the AC susceptibility measurements and in red from the dynamic light scattering.

## 7.4 Summary and Conclusion

This work shows a measure for the interaction strength between  $CoFe_2O_4$  NPs and the PNIPAM microgel matrix. The system is described utilizing a phenomenological model, which represents the Brownian and Néel relaxation. To some extent, both can be separated and interpreted independently. All together the MNPs are used to probe the inner structure of the microgels and the impact of the microgel mesh size on the magnetic properties and their interaction strength. Additionally, the interaction strength can be controlled indirectly by varying the temperature and therefore the mesh size.

The TEM images of the MMGs show the influence of AM on the MNP distribution. The MNPs form small clusters inside the microgel in the presence of AM while without AM the MNPs are well separated. The majority of the MNPs are inside the microgels. One of the observed relaxation peaks ( $\approx 1$  Hz) shifts to higher frequency with increasing temperature, corresponding to smaller particles sizes, originating in the collapse of the MG by crossing the VPTT. The VPTT of the MMGs was observed with DLS, EM, FC-ZFC measurements and with AC-susceptibility. But the reversible process could not be observed with AC-susceptibility. The Brownian relaxation peak vanishes above  $34$  °C and does not re-appear upon cooling down. Until now the origin of this effect remains unknown as stability experiments with UV/Vis absorption measurements and DLS do not show any aggregation. A second observed Brownian relaxation peak originates from the damped MNP relaxation of partially free MNP inside the meshes. These partially free MNPs are more confined in sample fMMG6 (with AM) compared to fMMG5 as they form small clusters in fMMG6. The formation of MNP clusters is favored for the MG with AM (fMMG6) as it appears to be more hydrophobic compared to its counterpart without AM (fMMG5). The addition of AM also influences the swelling ratio of the MGs and their electrophoretic mobility.

The findings open up various possible applications, such as tuneable drug delivery systems that change their magnetic response in dependence on the external environment. The combination of MNPs and microgels can be used for the creation of sensors, sensitive to multiple external stimuli. Additionally, the sensitivity of the device may be tuned or the sensor position adjusted within an external magnetic field. Furthermore, the interaction between MNPs and microgel network can be studied and may give a better understanding on polymer dynamic processes on a small scale. The studied magnetic microgel may serve as a starting point for designed magnetic polymers with tuneable interactions strength. Over all the studied MMGs are a suitable starting point for further investigations on the interaction strength between MNPs and MG matrix as well as a guideline for future applications with tunable MMGs.

## 8 Conclusion and Future Work

### 8.1 Conclusion

This PhD thesis focuses on combining magnetic nanoparticles (MNPs) with *N*-isopropylacrylamide (NIPAM) based microgels (MGs). Numerous studies have been done on core/shell structured magnetic microgels (MMGs). For MNPs with thin polymer coatings the whole polymer volume is affected by the MNP. With increasing polymer shell size the affected volume decreases. The magnetic response of such a system is reduced. This thesis shows the combination of hundred MNPs with a microgel matrix, which are distributed in a defined way. This results in a reduced non-reactive volume. Various microgels have been synthesized and were loaded with MNPs. The microgels and the MMGs were analyzed with dynamic light scattering (DLS), Zetasizer, atomic force microscopy (AFM) and transmission electron microscopy (TEM) in dependence of temperature, resulting in information about the size, shape, swelling ratio, electrophoretic mobility and elastic modulus.

The microgel properties (such as the swelling) were preserved after the MGs were loaded with MNPs. The MMGs show a volume phase transition temperature (VPPT) close to the literature value of 32 °C and a response to external magnetic fields. They can be separated from dispersion by a magnetic field and deformed, while adsorbed on a surface. This gives rise to future applications in guided drug delivery systems or magnetic sensor/actuator applications, but the deformation in external magnetic fields was smaller than predicted in simulations.

In order to enhance the response, two strategies were tested. The first was to increase the number of MNPs inside the microgel. This was achieved by changing the MNP stabilization from PAA to CA. The second strategy focuses on the above mentioned non-responsive volume, that also occurred in the MMGs from *Chapter 4*. The MNPs could not be embedded in the highly cross-linked microgel core. Several polymerization methods have been tested and showed a faster consumption rate of the cross-linker compared to NIPAM. The consumption rates are in good agreement with literature values. Using the feeding polymerization method, microgels with a homogeneous cross-linker distribution were obtained. The homogeneous distribution of the cross-linker is proven with TEM images and measurements of the elastic modulus. The homogeneous cross-linker distribution is visible by the constant elastic modulus over the whole microgel and the contrast in the TEM images is as well constant. Loading the homogeneously cross-linked microgels with MNPs results in MMGs, with a homogeneous distribution of MNPs and a minimized non-reactive volume. The magnetic response, such as the deformation in field direction, could not be tested due to difficulties by adsorbing the MMGs onto a surface.

To increase the stickiness of the MMGs, a thiol (-SH) moiety was polymerized into the microgels to increase the attractive interaction between the MGs and the gold surface by the formation of covalent sulfur-gold bonds. The hydrophobic allyl mercaptan resulted in structural differences within the microgels and changed the distribution of the embedded MNPs. The different agglomeration size of the MNPs inside the microgel posed a good opportunity to measure the magnetic relaxation time of the MMGs and MNPs. This provides insight into the coupling strength of the MNPs with the microgel network. Increasing the temperature (the gel starts to collapse) results in an increased interaction strength between the MNPs and the microgel matrix. Further measurements are required to quantify the interaction strength. Nevertheless, the desired increased attractive interaction between MMGs and the gold surface could not be proven undoubtedly. Some indications are given in the appendix.

To summarize, this thesis provides a better understanding of the microgel structure and its influence on the distribution of MNPs. Two driving factors for the MG loading could be identified (electrical charge and cross-linker distribution/concentration). This offers a suitable parameter set for designing MMGs with specific properties. Furthermore, the thesis proves the concept to measure the interaction strength between MNP and microgel matrix via AC-susceptibility. This can be used for designing MMGs with controllable sensitivity to external magnetic fields. The MMGs are suitable candidates for guided drug delivery systems due to their magnetic response and their swelling/shrinking. Furthermore, the MMGs may be used in sensors and actuators with adjustable sensitivity. Also the found measure for the interaction strength may be used in future simulations of magnetic polymer hybrid materials.

## 8.2 Future Work

The thesis provides insight into the microgel structure and influence on the combination with MNPs. Future research may focus on the distribution of different co-polymers that influence the loading with MNPs, e.g. the distribution of allylamine or allyl mercaptan. Also the distribution of cross-linker may be a subject in future experiments. Possible future measurements include dielectric spectroscopy to determine the water mobility inside the microgel meshes. Further experiments with the SQUID may offer a better understanding of the interaction strength between the MNP and the polymer network. Furthermore, this may lead to quantitative description of the binding energy. One big question still remains and could not be answered during this thesis: does the higher loaded MMGs from *Chapter 6* have a higher response to external magnetic fields, e.g. is the deformation in external magnetic fields increased compared to the results from *Chapter 4*? The used MNPs are spherical, future work may include non spherical MNPs such as ellipsoids or rods. The higher aspect ratio poses a higher potential for deforming the polymer matrix by aligning the MNPs in the magnetic field direction.

## 9 Danksagung

An erster Stelle möchte ich Prof. Dr. Regine von Klitzing für die Möglichkeit danken, meine Promotion in ihrer Gruppe schreiben zu dürfen. Ich bin dankbar für die Unterstützung und Führung, die sie mir in den Jahren angedeihen lassen hat. Zusätzlich hat sie immer Verständnis gezeigt für all die kleinen und großen Probleme während der Promotion, unabhängig davon, ob die Probleme mit der Arbeit zusammenhängen, wie z.B. der Umzug von Berlin nach Darmstadt, oder ob es Probleme privater Natur, wie meine Operationen, waren. Des Weiteren bin ich dankbar für die Freiheit in der Forschung, mit all den kleinen Nebenprojekten, die sie mir gegeben hat. Die Möglichkeit die Forschungsdaten auf nationalen und internationalen Kongressen vorzustellen war ebenfalls eine unschätzbare Bereicherung. Damit einher geht die Möglichkeit, sich mit Kollegen anderer Universitäten und anderer Länder über die Forschung auszutauschen und so neue Ideen und Einsichten zu bekommen.

Im Rahmen dessen möchte ich der TU Berlin, TU Darmstadt und der DFG für die finanziellen Mittel meiner Forschung danken.

Darüber hinaus möchte ich mich bei meinen Kollegen bedanken. Sie haben mir nicht nur mit ihrem Fachwissen geholfen, sondern auch eine sehr angenehme Arbeitsatmosphäre geschaffen. Ein besonderer Dank gilt auch allen Kollegen, die den Umzug von Berlin nach Darmstadt mitgemacht haben bzw. auch in Darmstadt von der Lichtwiese in die Stadtmitte. Es war eine anstrengende Zeit, die wir gemeinsam gemeistert haben. Wir sind gemeinsam an der Herausforderung gewachsen. Durch die gute Zusammenarbeit waren die Messaperaturen sehr schnell wieder funktionsbereit. Einige Kollegen möchte ich namentlich hervorheben, angefangen mit Dmitrij Stehl. In den Jahren, in denen wir das Büro geteilt haben, ist eine gute Freundschaft entstanden. Außerdem danke ich Maren Lehmann, die mir am Anfang meiner Promotion viel zur Synthese von Mikrogelen beigebracht hat und auch danach ein guter Diskussionspartner war, in allen Belangen der Mikrogele. Matthias Kühnhammer hat mir einige Male mit seinem Fachwissen aus der Chemie geholfen und war ein sehr angenehmer Zimmergenosse in Japan. Ebenfalls möchte ich noch Sebastian Backes erwähnen, der viele AFM Messungen für mich und unser gemeinsames Projekt durchgeführt hat. Ich danke auch Adrian Carl, Samantha Micciulla und Oliver Löhmann für ihren Beitrag, mich in der Gruppe wohl zu fühlen.

Neben meinen Kollegen, möchte ich auch meinen studentischen Hilfskräften danken, die mich während meiner Promotion unterstützt haben, darunter: Julia Strebe, Valeria Kolosova, Sandra Forg und Anahid Amiri. Auch Nadir Möller hat mir, in Rahmen seiner Masterarbeit, bei der Veröffentlichung meines ersten Papers sehr mit den AFM-Messungen geholfen.

Zuletzt möchte ich noch meiner Familie und meinen Freunden danken, für die viele

Ablenkung zu Stressbewältigung und zum Abschalten, um am nächsten Montag wieder frisch ans Werk gehen zu können. Besonders möchte ich Maximilian Neumann nennen, mit dem ich viele Jahre lang abschalten konnte und der immer ein offenes Ohr hatte. Auch Christian und Heike Presse möchte ich danken für die viele Unterstützung und die familiäre Atmosphäre und zum Schluss Julia Krok, die mich die letzten Jahre meiner Dissertation begleitet hat.

## 10 Abbreviations

AA	allylamine
AAPH	2,2'-Azobis(2-methylpropionamidine) dihydrochloride
AFM	atomic force microscopy
AM	allylmercaptan
APS	ammonium persulfate
BIS	<i>N,N'</i> -methylenebis(acrylamide)
CA	citric acid
DLS	dynamic light scattering
EM	electrophoretic mobility
KPS	potassium persulfate
LCST	lower critical solution temperature
MMG	magnetic microgel
MNP	magnetic nanoparticle
MG	microgel
<i>NP</i>	nanoparticle
NIPAM	<i>N</i> -isopropylacrylamide
PAA	poly acrylicacid
PNIPAM	poly- <i>N</i> -isopropylacrylamide
STM	scanning tunneling microscopy
SPM	scanning probe microscopy
SQUID	superconduction quantum interference device
TEM	transmission electron microscopy
UCST	upper critical solution temperature
UV	ultra violet
VIS	visible
VPT	volume phase transition
VPTT	volume phase transition temperature
$c_i$	concentration of component $i$
$d$	particle diameter
$d$	cuvette length
$D$	distance between two particles
$D$	diffusion coefficient
$e$	elementary charge
$E$	Energy

$E$	electrical field
$f$	number of counter ions
$f(ka)$	Henry parameter
$F$	force
$g^1$	field correlation coefficient
$g^2$	intensity correlation coefficient
$H$	enthalpy
$k$	reaction rate constant
$k_B$	Boltzmann constant
$K_{eff}$	effective magnetic anisotropy constant
$K_s$	surface anisotropy constant
$\vec{L}$	orbital angular momentum
$m$	mass of particle
$\vec{M}$	magnetization
$n$	refractive index
$\underline{N}$	diagonalized demagnetization tensor
$N_A$	Avogadro constant
$N_c$	number of chains in gel
$\vec{q}$	scattering vector
$q$	number density
$r$	particle radius
$r_H$	hydrodynamic radius
$S$	entropy
$\vec{S}$	spin angular momentum
$t$	time
$T$	temperature
$v$	molar solvent volume
$v$	particle velocity
$V$	volume
$V_0$	volume of relaxed Gaussian gel
$V_H$	hydrodynamic volume
$Z$	ion valency
$\alpha$	swelling ratio
$\beta$	geometry factor in light scattering
$\chi$	Flory-Huggins parameter
$\eta$	viscosity
$\epsilon$	permittivity
$\epsilon_\lambda$	molar attenuation coefficient
$\gamma$	friction coefficient
$\Gamma$	decay rate
$\kappa$	Debye length
$\lambda$	wavelength
$\mu$	electrophoretic mobility

$\mu_0$	magnetic permeability of vacuum
$\mu_2$	moment of second order
$\mu_3$	moment of third order
$\mu_B$	Bohr magneton
$\mu_r$	magnetic permeability of materials
$\sigma$	charge density
$\tau$	time constant
$\tau$	transmittance
$\theta$	angle between easy axis and magnetization
$\theta$	scattering angle
$\Theta$	rotation angle
$\Phi$	volume fraction
$\Pi$	osmotic pressure
$\zeta$	zeta potential

## Bibliography

- [1] A. Ahiabu and M. J. Serpe. Rapidly responding ph- and temperature-responsive poly (n-isopropylacrylamide)-based microgels and assemblies. *ACS Omega*, 2(5):1769–1777, 2017.
- [2] A. Burmistrova, M. Richter, C. Üzüüm, and R. von Klitzing. Effect of cross-linker density of p(nipam-co-aac) microgels at solid surfaces on the swelling/shrinking behaviour and the young’s modulus. *Colloid Polym. Sci.*, 289:613–624, 2011.
- [3] A. Burmistrova, M. Richter, M. Eisele, C. Üzüüm, and R. von Klitzing. The effect of co-monomer content on the swelling/shrinking and mechanical behaviour of individually adsorbed pnipam microgel particles. *Polymers*, 3:1575–1590, 2011.
- [4] A. Burmistrova, M. Richter, M. Eisele, C. Üzüüm, and R. von Klitzing. The effect of co-monomer content on the swelling/shrinking and mechanical behaviour of individually adsorbed pnipam microgel particles. *Polymers*, 3:1575–1590, 2011.
- [5] A. Burmistrova, R. Steitz, and R. von Klitzing. Temperature response of pnipam derivatives at planar surfaces : Comparison between polyelectrolyte multilayers and adsorbed microgels. *Chem. Phys. Chem.*, 11:3571–3579, 2010.
- [6] A. Burmistrova and R. von Klitzing. Control of number density and swelling/shrinking behavior of p(nipam-aac) particles at solid surfaces. *J. Mat. Chem.*, 20:3502–3507, 2010.
- [7] A. E. Deatsch and B. A. Evans. Heating efficiency in magnetic nanoparticle hyperthermia. *J. Magn. Magn. Mater.*, 354:163–172, 2014.
- [8] A. Fernández-Nieves, A. Fernández-Barbero, B. Vincent, and F. J. de las Nieves. Charge controlled swelling of microgel particles. *Macromolecules*, 33(6):2114–2118, 2000.
- [9] A. Fernandez-Nieves, A. Fernandez-Barbero, B. Vincent, and F. J. de las Nieves. Charge controlled swelling of microgel particles. *Macromolecules*, 33:2114–2118, 2000.
- [10] A. Fernandez-nieves, H. M. Wyss, J. Mattsson, and D. a Weitz. *Microgel Suspensions*. Wiley-VCH Verlag GmbH & Co. KGaA, 2011.
- [11] A. Gandhi, A. Paul, S. Oommen Sen, and K. K. Sen. Studies on thermoresponsive polymers: Phase behaviour, drug delivery and biomedical applications. *Asian Journal of Pharmaceutical Sciences*, 10(2):99–107, 2015.

- [12] A. Garcia, M. Marquez, T. Cai, R. Rosario, Z. Hu, D. Gust, M. Hayes, S. A. Vail, and C. Park. Photo-, thermally, and ph-responsive microgels. *Langmuir*, 23(1):224–229, 2007.
- [13] A. Mukhopadhyay and S. Granick. Micro- and nanorheology. *Curr. Opin. Colloid Interface Sci.*, 6(5-6):423–429, 2001.
- [14] A. P. H. Gelissen, A. Oppermann and T. Caumanns, P. Hebbeker, S. K. Turnhoff, R. Tiwari, S. Eisold, U. Simon, Y. Lu, J. Mayer, W. Richtering, A. Walther, and D. Wöll. 3d structures of responsive nanocompartmentalized microgels. *Nano Letters*, 16(11):7295–7301, 2016.
- [15] A. Pich, S. Bhattacharya, Y. Lu, V. Boyko, and H. P. Adler. Temperature-sensitive hybrid microgels with magnetic properties. *Langmuir*, 20(24):10706–10711, 2004.
- [16] A. Seyfoori, S. A. Seyyed Ebrahimi, E. Samiei, and M. Akbari. Multifunctional Hybrid Magnetic Microgel Synthesis for Immune-Based Isolation and Post-Isolation Culture of Tumor Cells. *ACS Appl. Mater. Interfaces*, 11(28):24945–24958, 2019.
- [17] A. Y. Zubarev and D. Y. Borin. Effect of particle concentration on ferrogel magnetodeformation. *Journal of Magnetism and Magnetic Materials*, 377:373–377, 2015.
- [18] A. Amikam. *Introduction to the Theory of Ferromagnetism*. Oxford University Press, 2001.
- [19] E. Daly and B. R. . Temperature-dependent electrophoretic mobility and hydrodynamic radius measurements of poly(n-isopropylacrylamide) microgel particles: structural insights. *Phys. Chem. Chem. Phys.*, 2(14):3187–3193, 2000.
- [20] B. Fischer, B. Huke, M. Lücke, and R. Hempelmann. Brownian relaxation of magnetic colloids. *J. Magn. Magn. Mater.*, 289:74–77, 2005.
- [21] B. R. Saunders and B. Vincent. Microgel particles as model colloids: Theory, properties and applications. *Advances in Colloid and Interface Science*, 80(1):1–25, 1999.
- [22] S. Backes. *PNIPAM Microgels in External Fields*. PHD-Thesis, Technische Universität Berlin, Fakultät für Chemie, März 2018.
- [23] W. F. Brown. Thermal fluctuations of a single-domain particle. *Phys. Rev.*, 130(5):1677–1686, 1963.
- [24] C. Cannas, A. Musinu, G. Piccaluga, D. Fiorani, D. Peddis, H. K. Rasmussen, and S. Mørup. Magnetic properties of cobalt ferrite-silica nanocomposites prepared by a sol-gel autocombustion technique. *The Journal of Chemical Physics*, 125(16):164714, oct 2006.

- [25] C. Dagallier, H. Dietsch, P. Schurtenberger, and F. Scheffold. Thermoresponsive hybrid microgel particles with intrinsic optical and magnetic anisotropy. *Soft Matter*, 6(10):2174–2177, 2010.
- [26] C. Liu, J. Guo, W. Yang, J. Hu, C. Wang, and S. Fu. Magnetic mesoporous silica microspheres with thermo-sensitive polymer shell for controlled drug release. *J. Mater. Chem.*, 19(27):4764–4770, 2009.
- [27] C. Y. Kuo, T. Y. Liu, K. S. Wang, A. Hardiansyah, Y. T. Lin, H. Y. Chen, and W. Y. Chiu. Magnetic and thermal-sensitive poly(N-isopropylacrylamide)-based microgels for magnetically triggered controlled release. *J. Vis. Exp.*, 125, 2017.
- [28] D. Subhash, H. Mody, R. Banerjee, D. Bahadur, and R. Srivastava. Poly(n-isopropylacrylamide) based polymer nanogels for drug delivery applications. In *2011 11th IEEE International Conference on Nanotechnology*, pages 1741–1744, 2011.
- [29] E. A. Appel, X. J. Loh, S. T. Jones, F. Biedermann, C. A. Dreiss, and O. A. Scherman. Ultrahigh-water-content supramolecular hydrogels exhibiting multistimuli responsiveness. *J. Am. Chem. Soc.*, 134(28):11767–11773, 2012.
- [30] E. C. Stoner and E. P. Wohlfarth. A mechanism of magnetic hysteresis in heterogeneous alloys. *R. Soc.*, 240(826):599–642, 1948.
- [31] E. Roeben, L. Roeder, S. Teusch, M. Effertz, U. K. Deiters, and A. M. Schmidt. Magnetic particle nanorheology. *Colloid Polym. Sci.*, 292(8):2013–2023, 2014.
- [32] A. Einstein. Ueber die von der molekularkinetischen Theorie der Waerme geforderte Bewegung von in ruhenden Flüssigkeiten suspendierten Teilchen. *Ann. d. Phys.*, 322(8):549–560, 1905.
- [33] A. Einstein. Zur Theorie der Brownschen Bewegung. *Ann. d. Phys.*, 324(5):371–381, 1906.
- [34] M. Eisele. *Kinetic studies on PEG-based microgels with different cross-linker and their influence on structure and properties*. Diploma thesis, Technical University Berlin, 2015.
- [35] F. Ludwig, A. Guillaume, M. Schilling, N. Frickel, and A. M. Schmidt. Determination of core and hydrodynamic size distributions of CoFe<sub>2</sub>O<sub>4</sub> nanoparticle suspensions using ac susceptibility measurements. *Journal of Applied Physics*, 108(3):033918, aug 2010.
- [36] F. Xu, J. H. Geiger, G. L. Baker, and M. L. Bruening. Polymer brush-modified magnetic nanoparticles for his-tagged protein purification. *Langmuir*, 27(6):3106–3112, 2011.
- [37] G. Binnig, C. F. Quate, and C. Gerber. Atomic force Microscope. *Phys. Rev. Lett.*, 56(9):930–934, 1986.

- [38] G. Huang and Z. Hu. Phase behavior and stabilization of microgel arrays. *Macromolecules*, 40, 2007.
- [39] H. Lange, B. H. Juárez, A. Carl, M. Richter, N. G. Bastús, H. Weller, C. Thomsen, R. von Klitzing, and A. Knorr. Tunable plasmon coupling in distance-controlled gold nanoparticles. *Langmuir*, 28(24):8862–8866, 2012.
- [40] H. S. Ashbaugh and M. E. Paulaitis. Monomer hydrophobicity as a mechanism for the lcst behavior of poly(ethylene oxide) in water. *Industrial & Engineering Chemistry Research*, 45(16):5531–5537, 2006.
- [41] H. Senff and W. Richtering. Temperature sensitive microgel suspensions: Colloidal phase behavior and rheology of soft spheres. *The Journal of Chemical Physics*, 111(4):1705–1711, 1999.
- [42] H. Senff and W. Richtering. Temperature sensitive microgel suspensions: Colloidal phase behavior and rheology of soft spheres. *J. Chem. Phys.*, 111:1705–1711, 1999.
- [43] H. Herz. Über die berührung fester elastischer körper. *Journal für die reine und angewandte Mathematik*, 92(16):156–171, 1881.
- [44] I. Berndt and W. Richtering. Doubly temperature sensitive core–shell microgels. *Macromolecules*, 36(23):8780–8785, 2003.
- [45] I. Gorelikov, L. M. Field, and E. Kumacheva. Hybrid microgels photoresponsive in the near-infrared spectral range. *J. Am. Chem. Soc.*, 126:15938–15939, 2004.
- [46] I. Kamal and S. Al-Naimi. In ' *Polymers and Nanotechnology* '. *Proceedings of the Knowledge Based Industries & Nanotechnology Conference. 11th-12th February (2008), Doha-Qatar.*, 02 2008.
- [47] J. C. Rose, M. Fölster, L. Kivilip, J. L. Gerardo-Nava, E. E. Jaekel, D. B. Gehlen, W. Rohlf, and L. De Laporte. Predicting the orientation of magnetic microgel rods for soft anisotropic biomimetic hydrogels. *Polym. Chem.*, 11:496–507, 2020.
- [48] J. Cai, J. Guo, M. Ji, W. Yang, C. Wang, and S. Fu. Preparation and characterization of multiresponsive polymer composite microspheres with core – shell structure. *Colloid Polym Sci*, 285:1607–1615, 2007.
- [49] J. Dieckhoff, D. Eberbeck, M. Schilling, and F. Ludwig. Magnetic-field dependence of Brownian and Néel relaxation times. *J. Appl. Phys.*, 119(4), 2016.
- [50] J. E. Wong, A. K. Gaharwar, D. Mueller-Schulte, D. Bahadur, and W. Richtering. Layer-by-layer assembly of a magnetic nanoparticle shell on a thermoresponsive microgel core. *J. Magn. Magn. Mat.*, 311:219–223, 2007.
- [51] J. Feng, S. Xuan, Z. Lv, L. Pei, Q. Zhang, and X. Gong. Magnetic-Field-Induced Deformation Analysis of Magnetoactive Elastomer Film by Means of DIC, LDV, and FEM. *Ind. Eng. Chem. Res.*, 57(9):3246–3254, 2018.

- [52] J. Kestin, M. Sokolov, and W. A. Wakeham. Viscosity of liquid water in the range  $-8\text{ }^{\circ}\text{C}$  to  $150\text{ }^{\circ}\text{C}$ . *Journal of Physical and Chemical Reference Data*, 7(3):941–948, jul 1978.
- [53] J. Landers, S. Salamon, H. Remmer, F. Ludwig, and H. Wende. In-field orientation and dynamics of ferrofluids studied by mössbauer spectroscopy. *ACS Applied Materials & Interfaces*, 11(3):3160–3168, dec 2018.
- [54] J. N. Israelachvili. *Intermolecular and Surface Forces*. Academic Press, 2nd ed. edition, 1998.
- [55] J. Rubio-Retama, N. E. Zafeiropoulos, C. Serafinelli, R. Rojas-Reyna, B. Voit, E. Lopez Cabarcos, and M. Stamm. Synthesis and characterization of thermosensitive pnipam microgels covered with superparamagnetic g-fe<sub>2</sub>o<sub>3</sub> nanoparticles. *Langmuir*, 23(20):10280–10285, 2007.
- [56] J. Witte, T. Kyrey, J. Lutzki, A. M. Dahl, J. Houston, A. Radulescu, V. Pipich, L. Stingaciu, M. Kühnhammer, M. U. Witt, R. von Klitzing, O. Holderer, and S. Wellert. A comparison of the network structure and inner dynamics of homogeneously and heterogeneously crosslinked PNIPAM microgels with high crosslinker content. *Soft Matter*, 15(5):1053–1064, 2019.
- [57] K. Gawlitza, S. T. Turner, F. Polzer, S. Wellert, M. Karg, P. Mulvaney, and R. von Klitzing. Interaction of gold nanoparticles with thermoresponsive microgels: influence of the cross-linker density on optical properties. *Phys. Chem. Chem. Phys.*, 15(37):15623–15631, 2013.
- [58] K. Jain, R. Vedarajan, M. Watanabe, M. Ishikiriya, and N. Matsumi. Tunable lcst behavior of poly(n-isopropylacrylamide/ionic liquid) copolymers. *Polym. Chem.*, 6(38):6819–6825, 2015.
- [59] K. Kratz, T. Hellweg, and W. Eimer. Influence of charge density on the swelling of colloidal poly(n-isopropylacrylamide-co-acrylic acid) microgels. *Colloids Surf. A*, 170:137–149, 2000.
- [60] K. Kratz, T. Hellweg, and W. Eimer. Structural changes in pnipam microgel particles as seen by sans, dls, and em techniques. *Polymer*, 42:6631–6639, 2001.
- [61] A. Khan. Preparation and characterization of magnetic nanoparticles embedded in microgels. *Mater. Lett.*, 62(6-7):898–902, 2008.
- [62] D. E. Koppel. Analysis of macromolecular polydispersity in intensity correlation spectroscopy: The method of cumulants. *J. Chem. Phys.*, 57(11):4814–4820, 1972.
- [63] L. Roeder, M. Reckenthäler, L. Belkoura, S. Roitsch, R. Strey, and A. M. Schmidt. Covalent ferrohydrogels based on elongated particulate cross-linkers. *Macromolecules*, 47(20):7200–7207, 2014.

- [64] L. Schulz, W. Schirmacher, A. Omran, W. R. Shah, P. Böni, W. Petry, and P. Müller-Buschbaum. Elastic torsion effects in magnetic nanoparticle diblock-copolymer structures. *J. Phys. Condens. Matter*, 22:346008, 2010.
- [65] L. V. Nikitin, L. S. Mironova, G. V. Stepanov, and A. N. Samus. The influence of a magnetic field on the elastic and viscous properties of magnetoelastics. *Polym. Sci. Series A*, 43:443–450, 2001.
- [66] L. Wang, R. M. Liao, and X. Z. Li. Layer-by-layer deposition of luminescent polymeric microgel films on magnetic fe<sub>3</sub>o<sub>4</sub>@sio<sub>2</sub> nanospheres for loading and release of ibuprofen. *Powder Techn.*, 235:103–109, 2013.
- [67] J. Landers. *Study of magnetic relaxation dynamics in soft matter nanoparticle composite systems*. PHD-Thesis, Universität Duisburg-Essen, Fakultät für Physik, November 2016.
- [68] P. Langevin. Sur la théorie du mouvement brownien. *C. R. Acad. Sci.*, 146:530–533, 1908.
- [69] M. Bañobre-López, A. Teijeiro, and J. Rivas. Magnetic nanoparticle-based hyperthermia for cancer treatment. *Reports Pract. Oncol. Radiother.*, 18(6):397–400, 2013.
- [70] M. Bonini, S. Lenz, E. Falletta, F. Ridi, E. Carretti, E. Fratini, A. Wiedenmann, and P. Baglioni. Acrylamide-based magnetic nanosponges: a new smart nanocomposite material. *Langmuir*, 24(21):12644–12650, 2008.
- [71] M. Das, N. Sanson, D. Fava, and E. Kumacheva. Microgels loaded with gold nanorods: Photothermally triggered volume transitions under physiological conditions. *Langmuir*, 23:196–201, 2007.
- [72] M. J. Snowden, B. Z. Chowdhry, B. Vincent, and G. E. Morris. Colloidal copolymer microgels of n-isopropylacrylamide and acrylic acid: ph, ionic strength and temperature effects. *J. Chem. Soc., Faraday Trans.*, 92(24):5013–5016, 1996.
- [73] M. J. Snowden, B. Z. Chowdhry, B. Vincent, and G. E. Morris. Colloidal copolymer microgels of n-isopropylacrylamide and acrylic acid: ph, ionic strength and temperature effects. *J. Chem. Soc. Faraday Trans.*, 92:5013–5016, 1996.
- [74] M. Karg, I. Pastoriza-Santos, B. Rodriguez-Gonzalez, R. von Klitzing, S. Wellert, and T. Hellweg. Temperature, ph, and ionic strength induced changes of the swelling behavior of pnipam-poly(allylacetic acid) copolymer microgels. *Langmuir*, 24:6300–6306, 2008.
- [75] M. Karg, Y. Lu, E. Carbó-Argibay, I. Pastoriza-Santos, J. Pérez-Juste, L. M. Liz-Marzán, and T. Hellweg. Multiresponsive hybrid colloids based on gold nanorods and poly(nipam-co-allylacetic acid) microgels: Temperature- and ph-tunable plasmon resonance. *Langmuir*, 25(5):3163–3167, 2009.

- [76] M. Lehmann, W. Tabaka, T. Möller, A. Oppermann, D. Wöll, D. Volodkin, S. Wellert, and R. von Klitzing. Dls setup for in situ measurements of photoinduced size changes of microgel-based hybrid particles. *Langmuir*, 34(12):3597–3603, 2018.
- [77] M. R. Islam and M. J. Serpe. Poly(n-isopropylacrylamide) microgel-based thin film actuators for humidity sensing. *RSC Adv*, 4(60):31937–31940, 2014.
- [78] M. Shibayama, F. Ikkai, S. Inamoto, S. Nomura, and C. C. Han. pH and salt concentration dependence of the microstructure of poly(n-isopropylacrylamide-co-acrylic acid) gels. *J. Chem. Phys.*, 105:4358–4366, 1996.
- [79] M. Stieger, J. S. Pedersen, P. Lindner, and W. Richtering. Are thermoresponsive microgels model systems for concentrated colloidal suspensions? a rheology and small-angle neutron scattering study. *Langmuir*, 20(17):7283–7292, 2004.
- [80] M. U. Witt, J. Landers, S. Hinrichs and S. Salamon, J. Kopp, B. Hankiewicz, H. Wende, and R. v. Klitzing. Determination of core and hydrodynamic size distributions of CoFe<sub>2</sub>O<sub>4</sub> nanoparticle suspensions using ac susceptibility measurements. *Soft Matter*,
- [81] M. U. Witt, S. Hinrichs, N. Möller, S. Backes, B. Fischer, and R. von Klitzing. Distribution of CoFe<sub>2</sub>O<sub>4</sub> Nanoparticles Inside PNIPAM-Based Microgels of Different Cross-linker Distributions. *J. Phys. Chem. B*, 123(10):2405–2413, 2019.
- [82] M. Zrinyi, L. Barsi, and A. Buki. Ferrogel: a new magneto-controlled elastic medium. *Polym. Gels Netw.*, 5:415–427, 1997.
- [83] N. Sahiner and P. Ilgin. Soft core-shell polymeric nanoparticles with magnetic property for potential guided drug delivery. *Curr. Nanosci.*, 6:483–491, 2010.
- [84] L. Néel. Théorie du traînage magnétique des substances massives dans le domaine de Rayleigh. *J. Phys. le Radium*, 11(2):49–61, 1950.
- [85] P. J. Flory and J. Rehner. Statistical mechanics of cross-linked polymer networks I. Rubberlike elasticity. *J. Chem. Phys.*, 11(11):512–520, 1943.
- [86] P. Li, A. M. Zhu, Q. L. Liu, and Q. G. Zhang. Fe<sub>3</sub>O<sub>4</sub>/poly(n-isopropylacrylamide)/chitosan composite microspheres with multiresponsive properties. *Industrial & Engineering Chemistry Research*, 47(20):7700–7706, 2008.
- [87] G. Pacchioni. A not-so-strong bond. *Nat. Rev. Mater.*, 4(4):226, 2019.
- [88] Q. Wu, X. Wang, C. Liao, Q. Wei, and Q. Wang. Microgel coating of magnetic nanoparticles via bienzyme-mediated free-radical polymerization for colorimetric detection of glucose. *Nanoscale*, 7(40):16578–16582, 2015.
- [89] R. Acciaro, T. Gilányi, and I. Varga, Imre. Preparation of monodisperse poly(n-isopropylacrylamide) microgel particles with homogenous cross-link density distribution. *Langmuir*, 27(12):7917–7925, 2011.

- [90] R. Gui and H. Jin. Temperature-regulated polymerization and swelling/collapsing/flocculation properties of hybrid nanospheres with magnetic cores and thermo/ph-sensitive nanogel shells. *RSC Adv*, 4(6):2797–2806, 2014.
- [91] R. L. Snyder, V. Q. Nguyen, and R. V. Ramanujan. Design parameters for magneto-elastic soft actuators. *Smart Mater. Struct.*, 19:055017, 2010.
- [92] R. M. Torre and E. Della. Theoretical aspects of demagnetization tensors. *IEEE Trans. Magn.*, 2(4):739–744, 1966.
- [93] R. Pelton. Temperature-sensitive aqueous microgels. *Advances in Colloid and Interface Science*, 85(1):1–33, 2000.
- [94] R. Pelton. Temperature-sensitive aqueous microgels. *Adv. Colloid Interface Sci.*, 85:1–33, 2000.
- [95] R. Pelton. Poly(n-isopropylacrylamide) (pnipam) is never hydrophobic. *Journal of Colloid and Interface Science*, 348(2):673–674, 2010.
- [96] R. Pelton and P. Chibante. Preparation of aqueous lattices with n-isopropylacrylamide. *Colloids Surf*, 20:247–256, 1986.
- [97] R. Turcu, V. Socoliuc, I. Craciunescu, A. Petran, A. Paulus, M. Franzreb, E. Vasile, and L. Vekas. Magnetic microgels, a promising candidate for enhanced magnetic adsorbent particles in bioseparation: synthesis, physicochemical characterization, and separation performance. *Soft Matter*, 11(5):1008–1018, 2015.
- [98] R. Turcu, V. Socoliuc, I. Craciunescu, A. Petran, A. Paulus, M. Franzreb, E. Vasile, and L. Vekas. Magnetic microgels, a promising candidate for enhanced magnetic adsorbent particles in bioseparation: synthesis, physicochemical characterization, and separation performance. *Soft Matter*, 11:1008–1018, 2015.
- [99] R. Weber, S. Kantorovich, and C. Holm. Deformation mechanisms in 2d magnetic gels studied by computer simulations. *Soft Matter*, 8:9923–9932, 2012.
- [100] R. Weber, S. Kantorovich, and C. Holm. Deformation mechanisms in 2d magnetic gels studied by computer simulations. *Soft Matter*, 8(38):9923–9932, 2012.
- [101] S. Backes, M. U. Witt, E. Roeben, L. Kuhrts, S. Aleed, A. M. Schmidt, and R. von Klitzing. Loading of pnipam based microgels with  $\text{CoFe}_2\text{O}_4$  nanoparticles and their magnetic response in bulk and at surfaces. *The Journal of Physical Chemistry B*, 119(36):12129–12137, 2015.
- [102] S. Bhattacharya, F. Eckert, V. Boyko, and A. Pich. Temperature-, ph-, and magnetic-field-sensitive hybrid microgels. *Small*, 3(4):650–657, 2007.
- [103] S. Bohlius, H. R. Brand, and H. Pleiner. Macroscopic dynamics of uniaxial magnetic gels. *Phys. Rev. E*, 70:061411, 2004.

- [104] S. Christau, Z. Yenice, and J. Genzer. Brush/gold nanoparticle hybrids: Effect of grafting density on the particle uptake and distribution within weak polyelectrolyte brushes. *Langmuir*, 30, 2014.
- [105] S. J. Kemp, R. M. Ferguson, A. P. Khandhar, and K. M. Krishnan. Monodisperse magnetite nanoparticles with nearly ideal saturation magnetization. *RSC Adv.*, 6(81):77452–77464, 2016.
- [106] S. Monz, A. Tschöpe, and R. Birringer. Magnetic properties of isotropic and anisotropic coFe<sub>2</sub>O<sub>4</sub>-based ferrogels and their application as torsional and rotational actuators. *Phys. Rev. E*, 78(2):021404, 2008.
- [107] S. Mørup, E. Brok, and C. Frandsen. Spin structures in magnetic nanoparticles. *Journal of Nanomaterials*, 2013:1–8, 2013.
- [108] S. Mørup, M. F. Hansen, and C. Frandsen. *Magnetic Nanoparticles*, volume 1, pages 437–491. Elsevier, United Kingdom, 2011.
- [109] S. Sarkar, N. T. Ponce, A. Banerjee, R. Bandopadhyay, S. Rajendran, and E. Lichtfouse. Green polymeric nanomaterials for the photocatalytic degradation of dyes: a review. *Environ. Chem. Lett.*, 2020.
- [110] S. Webers, M. Hess, J. Landers, A. M. Schmidt, and H. Wende. Effect of phase transitions in polymer solutions on the magnetic response of embedded nanoparticles. *ACS Applied Polymer Materials*, 2(7):2676–2685, jun 2020.
- [111] S. Yan, C. Jiang, J. Guo, Y. Fan, and Y. Zhang. Synthesis of silver nanoparticles loaded onto polymer-inorganic composite materials and their regulated catalytic activity. *Polymers (Basel)*, 11(3), 2019.
- [112] Brian R. Saunders. On the structure of poly(N-isopropylacrylamide) microgel particles. *Langmuir*, 20(10):3925–3932, 2004.
- [113] T. Hoare, B. P. Timko, J. Santamaria, G. F. Goya, S. Irusta, S. Lau, C. F. Stefanescu, D. Lin, R. Langer, and D. S. Kohane. Magnetically triggered nanocomposite membranes: A versatile platform for triggered drug release. *Nano Letters*, 11:1395–1400, 2011.
- [114] T. Hoare and R. Pelton. Highly pH and temperature responsive microgels functionalized with vinylacetic acid. *Macromolecules*, 37(7):2544–2550, 2004.
- [115] T. Hoare and R. Pelton. Highly pH and temperature responsive microgels functionalized with vinylacetic acid. *Macromolecules*, 37:2544–2550, 2004.
- [116] T. Hoare and R. Pelton. Engineering glucose swelling responses in poly(n-isopropylacrylamide)-based microgels. *Macromolecules*, 40(3):670–678, 2007.

- [117] T. Kyrey, J. Witte, A. Feoktystov, V. Pipich, B. Wu, S. Pasini, A. Radulescu, M. U. Witt, M. Kruteva, R. von Klitzing, S. Wellert, and O. Holderer. Inner structure and dynamics of microgels with low and medium crosslinker content prepared: Via surfactant-free precipitation polymerization and continuous monomer feeding approach. *Soft Matter*, 15(32):6536–6546, 2019.
- [118] T. R. Matzelle, G. Geuskens, and N. Kruse. Elastic properties of poly(N-isopropylacrylamide) and poly(acrylamide) hydrogels studied by scanning force microscopy. *Macromolecules*, 36(8):2926–2931, 2003.
- [119] T. Still, K. Chen, A. M. Alsayed, K. B. Aptowicz, and A. G. Yodh. Synthesis of micrometer-size poly(N-isopropylacrylamide) microgel particles with homogeneous crosslinker density and diameter control. *J. Colloid Interface Sci.*, 405:96–102, 2013.
- [120] T. Tanaka. Collapse of Gels and the Critical Endpoint. *Phys. Rev. Lett.*, 40(12):820–823, 1978.
- [121] V. E. Shashoua and R. G. Beaman. Microgel : An idealized polymer molecule. *J. Polym. Sci.*, 33:101–117, 1958.
- [122] M. von Smoluchowski. Zur kinetischen Theorie der Brownschen Molekularbewegung und der Suspensionen. *Bullet. Int. Crac.*, 326(14):756–780, 1906.
- [123] W. Coffey, P. J. Cregg, and Y. Kalmykov. On the theory of debye and néel relaxation of single domain ferromagnetic particles. *Advances in Chemical Physics*, 83:263–464, 01 1993.
- [124] X. Batlle and A. Labarta. Finite-size effects in fine particles: Magnetic and transport properties. *J. Phys. D. Appl. Phys.*, 35(6), 2002.
- [125] X. Liang, Y. Deng, X. Pei, K. Zhai, K. Xu, Y. Tan, X. Gong, and P. Wang. Tough, rapid-recovery composite hydrogels fabricated via synergistic core-shell microgel covalent bonding and  $\text{Fe}^{3+}$  coordination cross-linking. *Soft Matter*, 13(14):2654–2662, 2017.
- [126] Y. Hirokawa and T. Tanaka. Volume phase transition in a nonionic gel. *The Journal of Chemical Physics*, 81(12):6379–6380, 1984.
- [127] Y. Lu and M. Ballauff. Thermosensitive core-shell microgels: From colloidal model systems to nanoreactors. *Prog. Polym. Sci.*, 36(6):767–792, 2011.
- [128] Y. Suzuki, G. Hu, R.B. Van Dover, and R.J. Cava. Magnetic anisotropy of epitaxial cobalt ferrite thin films. *J. Magn. Magn. Mater.*, 191(1-2):1–8, 1999.
- [129] Z. Hedayatnasab, F. Abnisa, and W. M. A. W. Daud. Review on magnetic nanoparticles for magnetic nanofluid hyperthermia application. *Mater. Des.*, 123:174–196, 2017.

# 11 Appendix

## 11.1 Magnetic Microgels: Different Approaches via Synthesis

The used MMGs in this thesis were formed by simple mixing of MNPs and MGs (see *Chapter 2*). Stronger interactions between the MNP and the microgel matrix may be created by synthesizing the microgels around the MNPs. Therefore, the microgels were polymerized in the presence of MNP.

### *Experimental Setup*

The performed microgel polymerization resembles the one discussed in *Chapter 3*. The batch and feeding methods were used. For the batch method, the MNP suspension was added to the reactants before the reaction started, i.e. before the starter was added. For the feeding reaction, the MNP suspension was added before the feeding started and the polymerization initiator was added. In several trials one parameter was varied keeping the others constant. The tested parameters include: concentration of MNPs, concentration of NIPAM/BIS, addition of acid (acetic acid) or base (sodium hydroxide), stirring speed and different MNPs. *Table 11.1* lists the different MNPs.

Material	Geometry	size / nm	Supplier	Institute
magnetite@CA	spherical	5.5 nm	Behrens	KIT
cobalt ferrite@PAA	spherical	5	Schmidt	Uni. Cologne
cobalt ferrite@CA	spherical	15	Schmidt	Uni. Cologne
cobalt ferrite@CA	spherical	15	Hankiewicz	Uni. Hamburg
nickel	rod	20x200	Birringer	Uni. Saarland
cobalt ferrite@salt	rod	8x50	Behrens	KIT

Table 11.1: The tested MNPs are listed with their stabilization, size and origin. CA is citric acid and KIT is the Karlsruher Institute of Technology. No information were provided on the stabilizer "salt" as the data are still unpublished.

A successful microgel polymerization (feeding method) was achieved with a cross-linker concentration of 5 mol%, the polymerization initiator was AAPH ( $n = 240 \mu\text{mol}$ ) and 1 ml of magnetite@CA (from Silke Behrens and Ingo Appelt,  $\beta = 3.1 \text{ mg/ml}$ ) was added. The feeding and reaction time was 10 min. Dialysis and freeze drying were performed as mentioned in *Chapter. 3*.

### *Results and Discussion*

Most of the performed polymerization failed due to a separation of MNPs and gel. Shortly after the polymerization started, the MNPs agglomerated and were coated with an inhomogeneous polymer structure. These agglomerates reached a size of up to a few millimeter. Additionally, macrogels formed around the stirring rod. Presumably the oppositely charge polymerization initiator and the MNPs attract each other, the attraction results in an agglomeration. Immediately after initiating the polymerization, the agglomeration started and was visible shortly after. In a different test base was added to increase the stabilization of the MNPs in suspension by creating more surface charges by deprotonating the citric acid. Also the addition of acid was tested. Both tests were unsuccessful. Increasing the stirring speed from 1000 rpm to 1500 rpm (a higher rotation speed was unsafe for the glass reactor) was also tested and as well unsuccessful. Different MNPs, different coatings and different concentrations were also tested, without success.

The first performed polymerization produced microgels in the desired size range, but most of the MNPs were agglomerated. *Figure, 11.1* shows a TEM image of the produced microgels. The polymerization was done without any modifications and similar to *Chapter 3*, beside the addition of MNP.

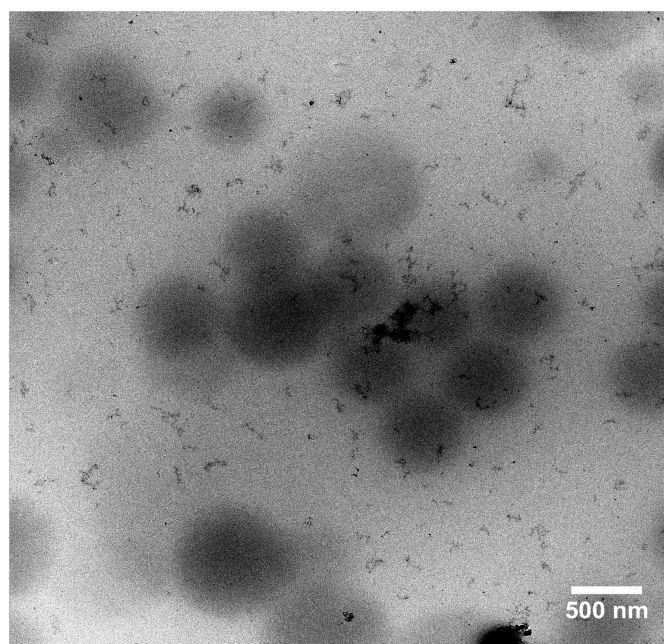


Figure 11.1: TEM image of microgels created in the synthesis with MNP present. The image was captured with a decreased acceleration voltage of 80 kV to increase the contrast of the microgels.

The image shows pure microgel particles with several MNP agglomerates around them. No usable MMGs could be produced.

### *Conclusion and Outlook*

During this study the polymerization of the microgels in presence of the MNPs was not successful. The biggest challenge is to prevent the MNP agglomeration. The tested parameter matrix is large and finding a suitable set of synthesis parameters would require more time. Only the first polymerization resulted in microgels, but the MNPs were agglomerated. So far no MMGs could be produced with this routine.

## **11.2 Allyl Mercaptane as "Glue"**

In *Chapter 4* and *6* the adsorption of the MMGs onto a surface plays an important role. During the performed experiments it became clear, that the MMGs are easily washed off from the surface. To increase the attraction between MMG and surface, several different surfaces have been tested (silica, gold and Mica). Using a gold coated surface leads to the highest amount of MMGs sticking to the surface. Also with the gold surface the smallest number of MMGs was washed off, during the AFM measurements in water. The advantage of gold coated surfaces is the formation of mirror charges. These mirror charges increase the interaction strength between the surface and the MMG. The number of detached MMGs was still high. To increase the interaction strength even further the co-polymer allyl mercaptan (AM) was polymerized into the microgels. The literature shows that gold and thiol (-SH) moieties form a bound [87] and this increases the MMG stickiness.

### *Experimental Setup*

The measured MMGs were fMMG5 (without AM) and fMMG6 (with AM). The full microgel synthesis is described in *Chapter 3*. In short: AM was added in the last minute of the feeding reaction. The last minute was chosen to increase the number of AM moieties on the MG surface and therefore, increase the number of possible binding points. The AFM was used to image the number of MMGs adsorbed onto the gold surface. The MMGs were spin coated onto the gold wafer as mentioned in *Chapter 3*. The prepared surface was scratched twice with a needle to form a cross. The imaged area was  $50 \times 50 \mu\text{m}$ . The position of the cantilever was marked with respect to the cross section of the scratches. An image of this process is shown in *Figure 11.2*. To always measure the same spot on the wafer, screen shots were made to note the exact position of the intersection between cantilever and the scratches. Furthermore, the z position and the focus of the microscope was noted to reproduce the magnification of the optical image.

After the first image the sample was submerged in water for 10 min and dried at  $60^\circ\text{C}$  for 10 min and re-imaged at the same position. The number of MMGs attached to the surface was counted for both images.



Figure 11.2: Photo taken before the sample was removed for washing. The edges of the cantilever and their intersection with the scratches were used to find the same spot.

#### *Results and Discussion*

*Figure 11.3* shows the imaged surfaces coated with fMMG5 (without AM) part a) before and b) after washing. The blue circle marks a spot on the wafer that can easily be recognized on both images. In both images the number of MMGs is constant: 40 individual MMGs. Washing the MMG coated wafers did not lead to a detachment of the MMGs.

*Figure 11.4* shows the imaged surfaces, coated with fMMG6 (with AM) part a) before and b) after washing. Also in this sample the number of observable MMG was constant (70 MMGs). No MMG was washed off.

The surface coverage was  $3.2 \pm 0.4$  % for fMMG5 and  $2.8 \pm 0.3$  % for fMMG6. Within the first error margin the surface coverage for both samples is equal. None of the adsorbed MMGs were washed off. No change of stickiness during the washing process was observed.

#### *Conclusion and Outlook*

The AM was successfully polymerized into the microgels as the differences in microgel properties in *Chapter 7* shows. The increased interaction strength between the MMGs and the gold surface could not be observed. A detachment of the MMGs was not

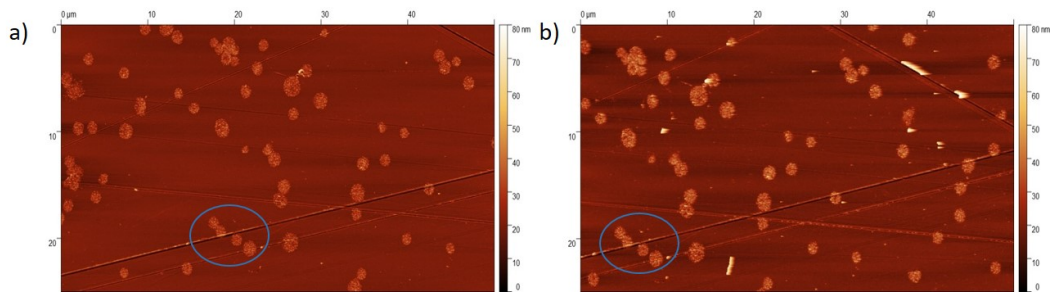


Figure 11.3: The AFM image shows the gold surface coated with fMMG5 (without AM) part a) before and b) after washing. The blue circles highlights four MMGs that can be used as reference points.

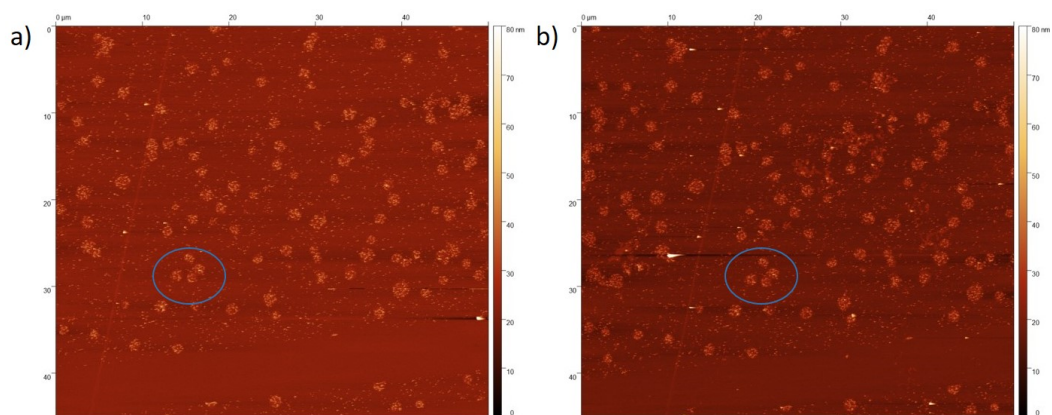


Figure 11.4: The AFM image shows the gold surface coated with fMMG6 (with AM)(a) before and b) after washing). The blue circles highlights four MMGs that can be used as reference points.

observed. In future experiments, the interaction strength between the MMG and the gold surface could be measured via colloidal probe AFM with a gold sphere attached to the cantilever. Also the washing time can be increased to see a time dependent effect for the detachment of the MMGs. Furthermore, imaging both samples in liquid (water) environment may also lead to a observable difference in their behavior.

### 11.3 Dynamic Light Scattering with Magnetic Field

In this thesis three major magnetic responses of the MMGs have been observed: the deformation of the MMGs in an external magnetic field, the separation from water in an inhomogeneous magnetic field and the magnetic relaxation process. Furthermore, MNPs can also be heated in high frequency external magnetic fields (compare *Chapter. 1* and *2*). To monitor such an energy transfer a combination of magnetic coil and DLS setup was built. The strategy was to include magnetic coils into the sample holder. The

heating of the MNPs and therefore, the MG shrinking could be observed simultaneously. Also the heating is proportional to the transferred energy. This could result in a VPT triggered for the MMGs by magnetic fields.

### Experiment

The self-built DLS consists of a HeNe laser with a wavelength of 632.8 nm and an energy output of 10 mW (purchased from ThorLabs). The laser beam is reflected by two mirrors into a focus lens with a focal length of 20 mm. The sample holder is a 3D-printed Helmholtz coil with hand-wounded copper wire. The sample holder is shown in *Figure 11.5 a)*. The coils had an inductance of 5.5  $\mu\text{H}$  and were combined with a capacitor of 150 nF to form a resonant circuit at about 100 – 200 kHz. The magnetic field was generated with a frequency generator and an amplifier. The created magnetic field strength could not be measured as the available Hall probe was not designed to measure such high frequency magnetic fields. The scattered light was directly measured with a Avalanche photo detector (APD130A2) from ThorLabs. The measurement frequency was set to 1 MHz. The data were recorded and analyzed in LabView. The whole setup is shown in *Figure 11.5 b)*.

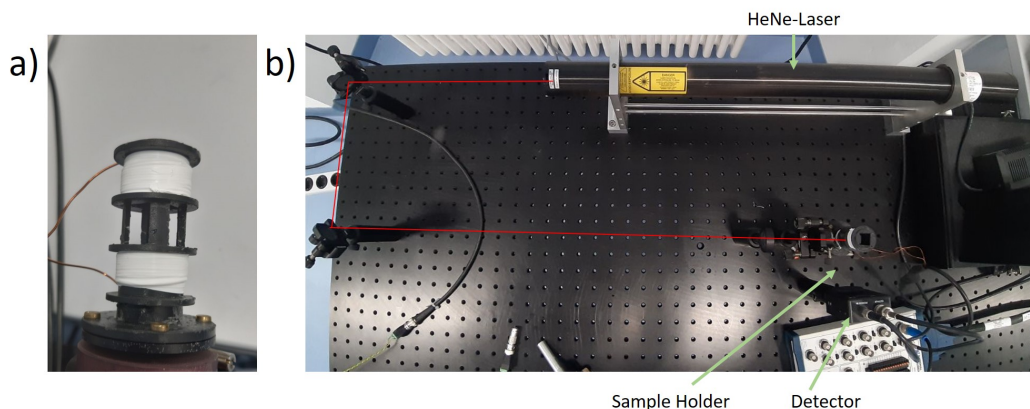


Figure 11.5: Part a) shows the self 3D-printed Helmholtz coil and b) the whole DLS setup. The laser beam path is shown in red.

The LabView program uses *Equation 2.23* and *2.25* to calculate the correlation data. The correlation data were averaged over 10 measurements and then fitted similar to the LS-Instruments DLS data (as described in *Chapter 3*). Note that the software correlation is slow. The number of performed computational steps ( $n$ ) scales with  $n = a * a$  with  $a$  being the number of data points. A typical measurement with 1 MHz and 1 s takes  $10^{12}$  computational steps, that is about 100 seconds. Averaging 10 data sets of 1 s takes less computational steps compared to measure once for 10 s. The DLS was tested with standard size samples purchased from Sigma Aldrich. The standard samples were also measured with the DLS from LS-Instruments as a reference. This is impotent, because the factory value was measured with a one angle setup (Zetasizer).

The magnetic heating was tested with a PT-100 submerged in a MNP dispersion. To

determine the performance peak of the Helmholtz coils, the change of temperature was measured against various magnetic field frequencies. The first 30 min were measured without a magnetic field to measure the equilibrium temperature of the MNP dispersion and the PT-100. Afterwards the different frequencies were set and the temperature was measured for 30 min every 10 s. The change of temperature was also measured in different media for two frequencies. The temperature of the medium was measured also for 30 min without a magnetic field to reach the equilibrium of room temperature. Afterwards the temperature was measured with field for 30 min every 10 s.

### Results and Discussion

Figure 11.6 shows the recorded data with the self-built DLS for the standard sample ( $r_H = 64$  nm). Part a) is a screen shot of the correlation data computed with the self written LabView program. Part b) shows the extracted data for a single measurements and part c) shows the average of 10 measurements. Averaging several data sets increases the measurement accuracy as statistical fluctuations are canceled out. Table 11.2 shows the size values of the measured standard samples.

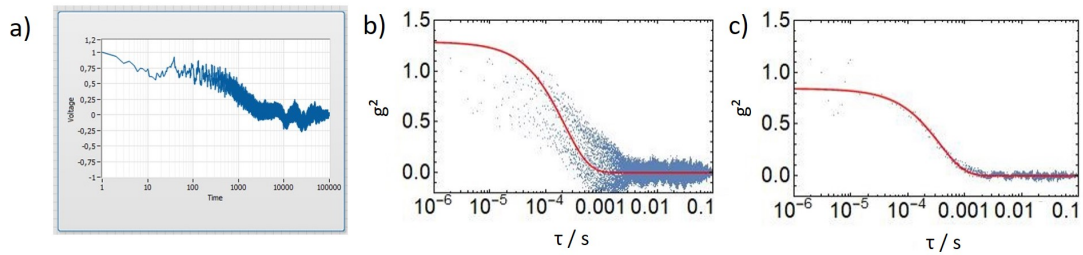


Figure 11.6: Part a) shows a screen shot of the correlation data computed by the LabView program. b) shows the extracted data transferred into origin for further treatment and c) shows an averaging of 10 measurements. The measured sample was the standard with  $r_H = 64$  nm.

Sample	$r_H(\text{Factory})$ / nm	$r_H$ (LS-I DLS) / nm	$r_H$ (self-built DLS) / nm
1	162	$165 \pm 8$	$173 \pm 12$
2	64	$70 \pm 6$	$52 \pm 12$

Table 11.2: Measured hydrodynamic radii for two standard samples.  $r_H(\text{Factory})$  denotes the particles size measured by the manufacturer with a Zetasizer similar to the one mentioned in Chapter 3.

The factory sizes were measured with the Zetasizer (similar to the one described in Chapter 3) by the manufacturer. Additionally, the size was measured with the DLS from LS-Instruments. For the 162 nm sample the measured size is in good agreement with the factory value and the reference value. The deviation is inside the first error margin. For the 64 nm sample the measured value is within the error margin of the theoretical

value but not for the reference value. Note that the reference values were measured over several angles (19) while the theoretical values were measured with a device only able to measure the back scattered light (173°) or forward scattered light (13°). The measured reference size is considered to be more trustworthy because the used device is more sophisticated.

*Figure 11.7* show two temperature measurements of a MNP suspension within the high frequency magnetic field. Part a) shows the temperature in the MNP suspension with different magnetic field frequencies. For no field ( $t < 2000$  s) the temperature decreases, showing the equilibration of the MNP dispersion to the room temperature (16.5 °C). Afterwards the temperature increases for all frequencies above the room temperature. The highest temperature was reached for 200 kHz. Part b) of *Figure 11.7* shows the temperature of different media with and without magnetic field. The first 30 min were measured without a magnetic field and the temperature drops down to room temperature. The temperature increases for the next 30 min with the applied magnetic field ( $f = 100$  kHz). The temperature increases for air to 22.65 °C, for water to 22.45 °C and for MNP dispersion to 22.70 °C. The change in temperature is highest for the MNP dispersion. The experiment were repeated with the higher frequency of 200 kHz. The temperature difference between MNP dispersion and water was  $\Delta T = 0.25$  K. *Table 11.3* shows the temperature differences for both frequencies. The temperature increase for all media most likely originates from the PT-100 that is heated by eddy currents.

Medium	f / kHz	$\Delta T_{max}/K$	$\Delta T_{ref}/K$
water	100	$5.95 \pm 0.05$	0
MNP	100	$6.20 \pm 0.05$	0.25
air	100	$6.15 \pm 0.05$	0.20
water	200	$13.65 \pm 0.05$	0
MNP	200	$13.91 \pm 0.05$	0.26
air	200	$12.26 \pm 0.05$	-1.39

Table 11.3: Peak temperatures measured with magnetic field for different media. The temperature difference is calculated between the two equilibrium states with and without field. Water was used for the reference.

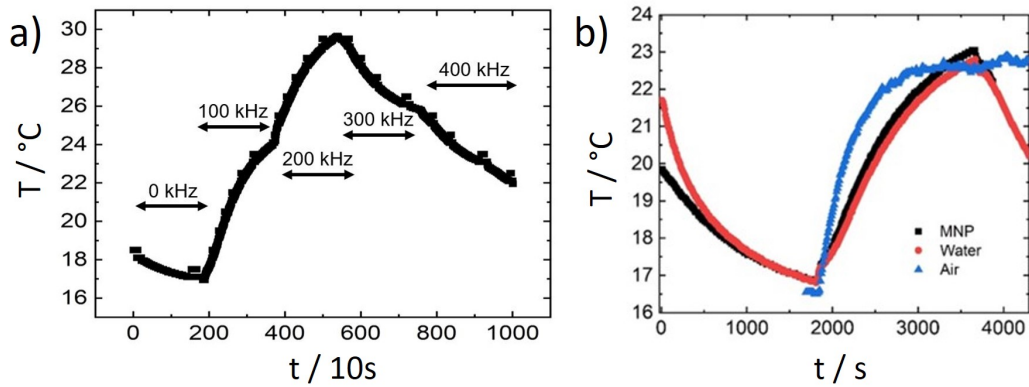


Figure 11.7: Part a) shows the temperature of the MNPs with various magnetic field frequencies. Part b) shows the temperature change measured with a PT-100 in different media at 100 kHz.

#### *Conclusion and Outlook*

The DLS setup was successfully built and the data show a good agreement of the particle size for particles with a hydrodynamic radius larger than  $r_H = 100$  nm. The induced temperature change with the high frequency magnetic field is rather small compared with the reference system (water). The temperature measurements were done with a PT-100. The PT-100 is made out of metal and the high frequency magnetic fields induces Eddy currents that increases the temperature of the PT-100 itself. The DLS setup can be used in future applications with a sample holder that can be easy adjusted by 3D-printing. Future magnetic measurements have to use a non invasive method (e.g. IR thermometer).